UNIVERSITÀ DEGLI STUDI DI PADOVA

CENTER OF STUDIES AND ACTIVITIES FOR SPACE "G. COLOMBO"

PhD Course in Space Sciences, Technologies and Measurements
Curriculum in Sciences and Technologies for Aeronautics and Satellite Applications

DEVELOPMENT AND TESTING OF A SMALL HYBRID ROCKET MOTOR FOR SPACE APPLICATIONS

PHD CANDIDATE
ENRICO PACCAGNELLA

Coordinator	Supervisor	Co-supervisor
Prof. Giampiero Naletto	Dr. Francesco Barato	Prof. Daniele Pavarin

CYCLE XXXII

ACADEMIC YEAR 2018–2019

DEVELOPMENT AND TESTING OF A SMALL HYBRID ROCKET MOTOR FOR SPACE APPLICATIONS

ENRICO PACCAGNELLA

A dissertation submitted to the Center of Studies and Activities for Space "G. Colombo" of the University of Padova (Italy) in partial fulfillment of the requirements for the degree of Doctor of Philosophy in Space Sciences, Technologies and Measurements.

This document was typeset in LaTeX using the typographical style `classicthesis`, designed by André Miede in homage to "The Elements of Typographic Style" of Robert Bringhurst.

Try to comprehend
a little more each day.
Have holy curiosity.
— Albert Einstein

ABSTRACT

In recent years there has been a significant renewed interest in hybrid propulsion for its unique features, in a world becoming more careful about safety, costs and environmental impact. Since the solid grain is made only of inert fuel and the propellants are physically separated by distance and phase, fabrication, transportation, storage, and handling can be done in complete safety and there is no possibility of an explosion. Moreover, the operational reliability is higher compared to solid and liquid motors. Hybrid rocket motors can also be throttled controlling only the flow of the liquid oxidizer and can be stopped and restarted multiple times with an appropriate ignition system. There is also the possibility to find several green combinations of oxidizer and fuel within the wide propellant choice. All the inherent advantages of hybrid propulsion can lead to a significant reduction in the total operational costs. Unfortunately, due to the characteristic diffusive flame mechanism, this technology presents also several disadvantages, like low regression rate, low combustion efficiency, low volume loading, and mixture ratio shift. However, most of these drawbacks can be solved through a correct design process and choosing convenient approaches. For this reason, the following research is focused on the development and testing of a small hybrid rocket motor, considering in particular possible space applications.

After introducing the hybrid propulsive system, the work starts with a review of the fundamental theory that explains the combustion process of hybrid rocket motors. This theory was developed in the early Sixties by Marxman, who based the analysis on the turbulent boundary layer combustion over a flat surface, and is in good agreement with the experimental data of the solid fuel grain regression. Briefly, in a classical hybrid motor configuration the oxidizer is injected into the combustion chamber from the head end of the motor and flows over the fuel surface. After the ignition of the motor, a macroscopic diffusion flame develops above the solid grain. The heat released from the reaction of combustion increases the temperature of the fuel grain until the surface decomposes due to pyrolysis. The vaporized fuel and the gaseous oxidizer are transported by convection and diffusion to the flame. Here the gases mix together and react, sustaining the combustion.

To help with the understanding of hybrid propulsion and its design, a set of simple explicit analytical equations to describe the hybrid rocket behavior and motor sizing are derived. Explicit relations are required in order to have a better sensibility on the trends, possibilities, and limits of this promising but tricky kind of propulsion system. The equations refer to the length, the diameter, the volume loading and the

length to diameter ratio of the combustion chamber, the performance penalties and the thrust variations incurred with time and throttling and the mission envelope of hybrid rocket motors. The need for these equations comes from the fact that hybrid rockets are generally not very flexible concerning the motor configuration, and the packaging of the hybrid propulsion system is strongly related to the sizing of the combustion chamber. Therefore, it is fundamental to understand how the length, the external diameter, the volume loading and the length to diameter ratio vary with the design parameters like scale, burning time, average mixture ratio, initial oxidizer mass flux and propellant combination. It is already possible to determine these quantities for conventional hybrid rocket motors thanks to the equations available in the literature. However, those equations are not in explicit form with respect to the aforementioned design parameters. Moreover, it is not possible to compute the instantaneous and average characteristic velocities during the burn without a numerical integration over time that interpolates a look-up table obtained from a thermochemical code. The use of explicit analytical tools has a strong beneficial effect, because it clearly shows the fundamental parameters affecting the results and their sometimes not intuitive dependencies.

Afterwards, two different motor configurations are designed and numerically verified. The two solutions are implemented in order to develop hybrid rocket motors with high regression rate and high combustion efficiency. The first approach is based on swirl injection of HTP burning with a HDPE solid grain, while the second one uses an axial injector and a propellant combination of HTP and a paraffin-based fuel. In both cases the HTP is first forced to pass through a catalytic reactor, where it decomposes into gaseous oxygen and water vapor at a temperature of around 1000 K, and then is injected inside the motor where its temperature is high enough to thermally decompose and ignite the fuel. This technique makes the motor self ignitable and restartable. HTP has several further advantages compared to other available oxidizers: it is storable, it allows to use gaseous injection, which in general has a very stable behavior since there are no droplet evaporation instabilities, and it has no problems of poor atomization at low pressure drops. Moreover, it permits to get full advantage of swirl oxidizer injection.

Following the design phase, a thorough experimental analysis have been conducted and the results are presented and discussed. The first motor configuration has been tested in order to understand the effects of the geometric swirl number on the performance of the propulsive system and to investigate the possibility of tailoring the regression rate based on the actual mission requirements. The throttling capability of this configuration has also been verified, with a real-time deep throttling firing test that uses a flow control valve specifically developed for this purpose by the Hybrid Propulsion Group of the University of Padova. Afterwards, since paraffin-based fuels have been often

regarded with skepticism due to their low melting temperature and softening point, the second configuration has been verified through a long burning time test.

Finally, a simple approach that is useful to decide which motor configuration is best suited to the intended space application is proposed. The problems that arise when designing the flightweight version of the same heavyweight motor are also discussed. These issues are mainly related to the thermal behavior of the system and to the erosion of the thermal protections. For example, if the thermal protections are not correctly sized, the heat flux conducted towards the motor case during the burning time can increase the temperature of the material up to its operating limit point or beyond. Moreover, considering the time frame that follows the motor shutdown, the heat accumulated in the system during the burning time increases the temperature of the solid fuel grain and the motor case, which can reach or even overcome its non-operating limit. A monodimensional thermal analysis is presented, considering both non-ablative and ablative thermal protections. Two different cases have been considered, namely an expendable hybrid rocket motor and a reusable one, where the latter can be used either in single-fire or in multi-fire mode. The obtained numerical model allows to size the thermal protections in order to efficiently withstand the thermal loads.

The following research demonstrates that it is feasible to develop a hybrid rocket motor that can fulfill the requirements of an actual space application with high performance, thus representing an alternative solution compared to liquid or solid rocket motors.

CONTENTS

LIST OF FIGURES

LIST OF TABLES

1 INTRODUCTION

Rocket motors can be divided according to the system used to produce exhaust matter and consequently thrust. Following this categorization, it is possible to distinguish among three main rocket propulsion systems: chemical propulsion, electrical propulsion and nuclear propulsion [109]. Chemical rocket motors are the most common ones and they use the combustion process of a propellant as energy source. The heat released by the chemical reactions is used to increase the internal energy of the gaseous products that is later converted into kinetic energy in the convergent-divergent nozzle.

The phase of the stored propellant is used to identify three different types of chemical rocket motors, namely liquid propellant motors, solid propellant motors and hybrid propellant motors. In liquid rocket motors the propellant is stored as liquid in tanks, as represented in figure 1.1. The propellant can be either a bipropellant if oxidizer and fuel are two separated liquids (stored in two different tanks), or a monopropellant if a single liquid contains both oxidizer and fuel (stored into a single tank). In solid rocket motors the propellant is cast into a solid shape inside the combustion chamber, as it can be seen in figure 1.2. Oxidizer and fuel are mixed together in the so-called solid grain. Hybrid rocket motors use a propellant combination composed by a liquid phase stored in a tank and a solid phase stored in the combustion chamber. As shown in figure 1.3, in the classical hybrid motor configuration the oxidizer is liquid and the fuel is solid, while in the reverse hybrid the oxidizer is solid and the fuel is liquid. However, research is focused on the former configuration, mainly because solid oxidizers are less energetic than liquid ones (excluding cryogenic solid oxidizers that involve storage issues) and because most liquid fuels must be handled with care. In figure 1.4 some different hybrid motors configurations are schematically represented.

The operation of hybrid rocket motors is completely different from the one of liquid and solid motors, even if they appear like an intermediate case and a mixture between the other two technologies. In a liquid motor the oxidizer and the fuel are injected independently in the combustion chamber where they mix together to form a combustible mixture with a specific mixture ratio that depends on the two mass flows. In a solid motor the oxidizer and the fuel are pre-mixed in the solid grain with a fixed mixture ratio. In both cases there is a uniform mixture in the whole combustion chamber. On the other hand, in a hybrid rocket motor the oxidizer and the fuel are injected into the combustion chamber from different sides and they burn in a large diffusion flame, as it will be explained in more detail later in

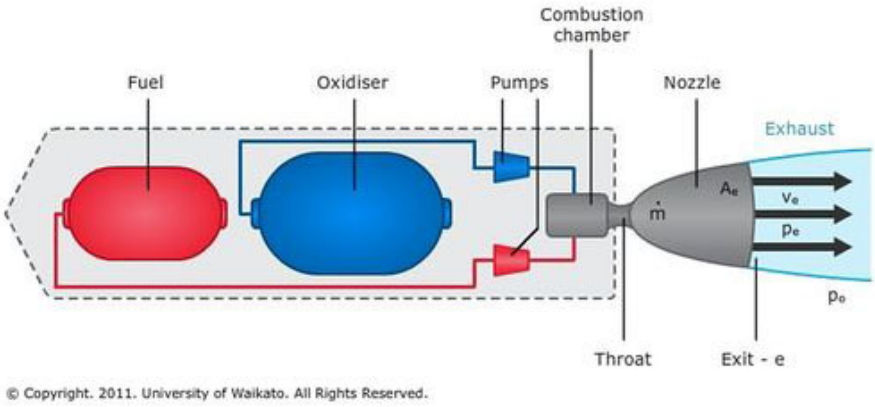

Figure 1.1: Liquid rocket motor

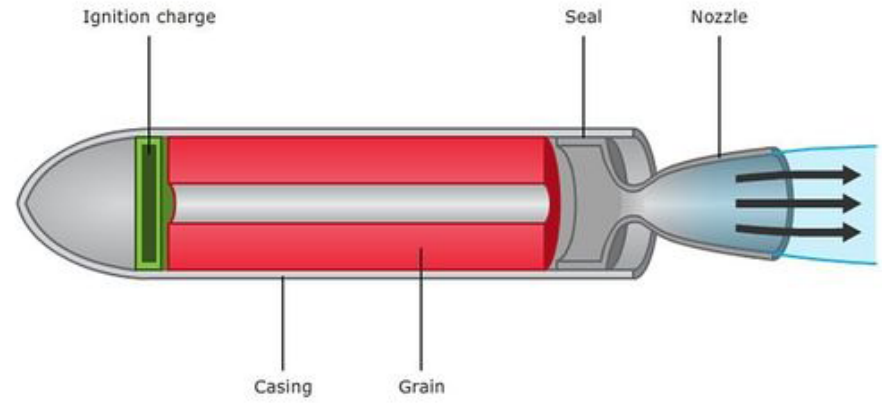

Figure 1.2: Solid rocket motor

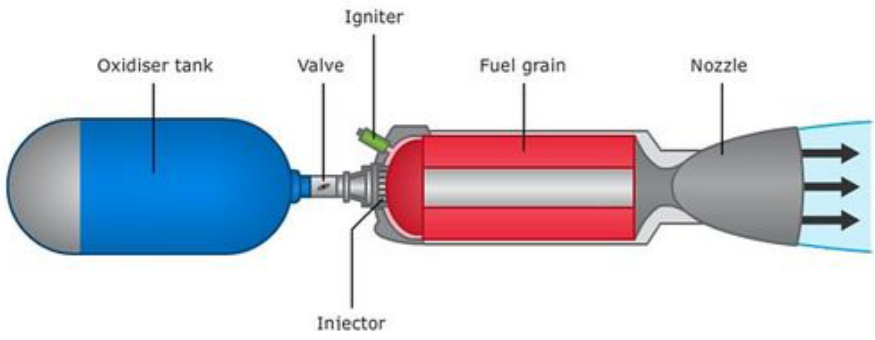

Figure 1.3: Hybrid rocket motor

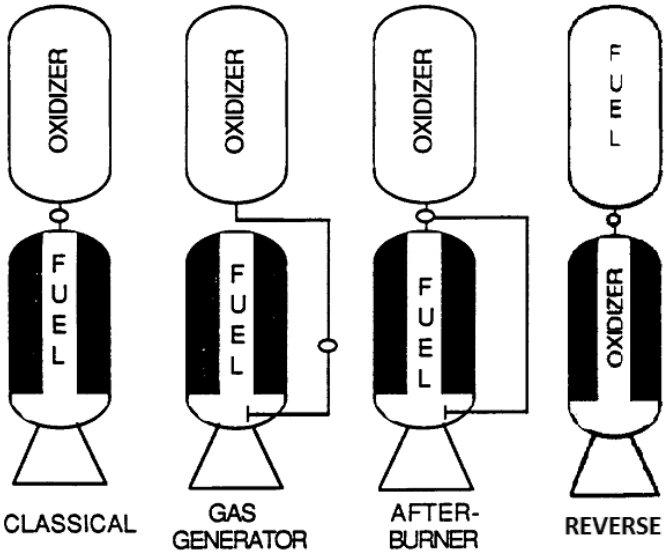

Figure 1.4: Different configurations of hybrid rocket motors

the next chapter. In this configuration, the mixture ratio varies along the length of the combustion chamber. This fundamental difference involves a number of distinctive features.

Hybrid rocket motors show several advantages compared to liquid and solid motors [2, 32]:

INTRINSIC SAFETY The fuel grain is made only of inert material. Therefore fabrication, transportation, storage and handling can be done in absolute safety. Oxidizer and fuel are physically separated by distance and phase and there is no possibility of an unwanted ignition. The system can be completely non-explosive if a non-explosive oxidizer is used. For this reason NASA classifies the propellant combination made of LOX and HTPB as zero TNT equivalent. Moreover, in case of an emergency abort operation, the motor can be stopped only closing the liquid oxidizer valve.

OPERATIONAL RELIABILITY The combustion process is regulated by a large diffusion flame that is less sensitive to imperfections of the fuel grain compared to solid motors, where the chamber pressure rises proportionally to the increase of the burning area and can easily reach the maximum design pressure of the motor in the presence of cracks. For this reason compared to solid motors the possibility of a catastrophic failure is largely reduced, while compared to liquid motors only half of the turbo-machinery, tanks and plumbing parts are required.

PROPULSIVE PERFORMANCE Hybrid motors can achieve a higher specific impulse compared to solid motors, which still have the highest volumetric specific impulse. Some propellants combinations can even approach the high performance of liquid motors,

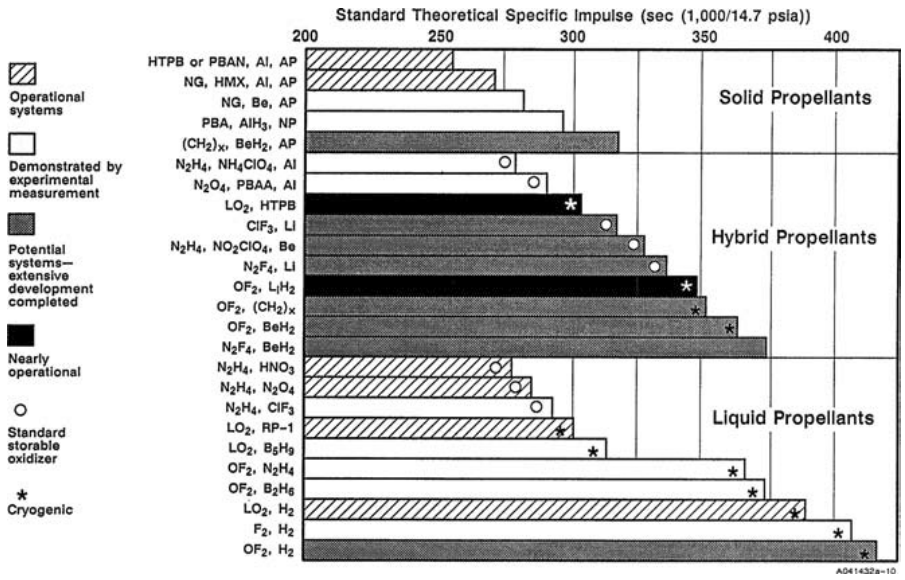

Figure 1.5: Theoretical specific impulse for different solid, liquid and hybrid motor propellant combinations [32]

while having a higher volumetric specific impulse. The propulsive performance of different solid, liquid and hybrid motors propellant combinations are compared in terms of theoretical specific impulse in figure 1.5.

MASS FLOW CONTROL The thrust of a hybrid motor can be varied in flight controlling only the flow of the liquid oxidizer through the valve. In liquid motors the process is more complex because two different liquid flows have to be modulated simultaneously. Moreover, the motor can be stopped and restarted many times, if an appropriate ignition system capable of multiple firings is provided.

PROPELLANT VERSATILITY The selection of propellants is much larger than with either liquid or solid motors. Like for solid motors, it is possible to add dense metal particles inside the fuel grain to improve the overall performance, without causing the formation of slurries like in liquid motors. Moreover, liquid oxidizers are more energetic compared to solid ones.

ENVIRONMENTAL FRIENDLINESS It is possible to find several green combinations of oxidizer and fuel among the wide propellant choice, which do not involve hazardous or toxic chemical species in the combustion process.

LOW COST The intrinsic safety and the operational reliability that characterize hybrid motors have the consequent advantage of reducing the total operational costs. The solid grain is made only of inert fuel and it can be manufactured in a commercial facility that does not require to follow any particular directive

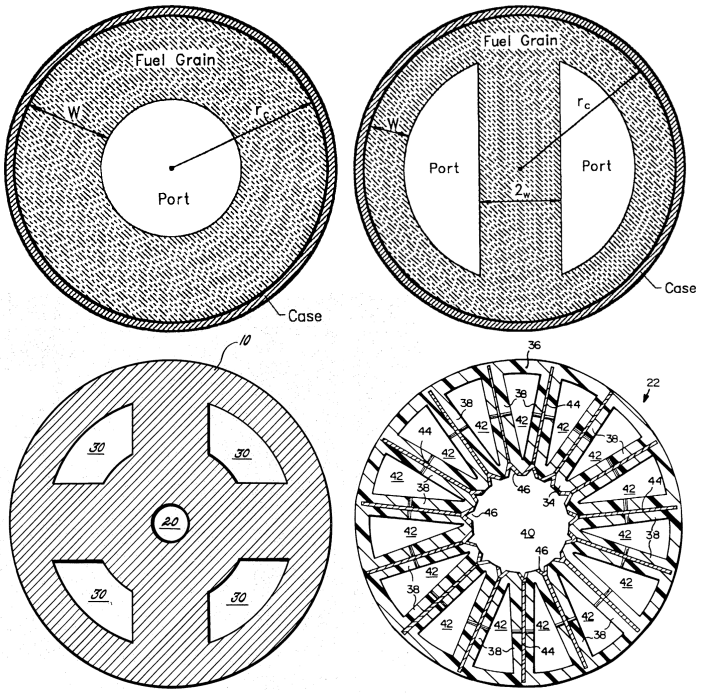

Figure 1.6: Example of increasing multiport grain configurations

on explosive materials. The fabrication costs are reduced also because the whole system can tolerate larger design margins. The costs for transportation, storage and handling are greatly reduced as well. Moreover, taking into consideration the elements that compose the inert mass of a motor, the cost of an hybrid system should stay between the cost of the simpler and cheaper solid motors and the cost of the more complex and expensive liquid motors.

Unfortunately hybrid rocket motors also present several disadvantages compared to liquid and solid motors:

LOW REGRESSION RATE Hybrid motors suffer of a low regression rate compared to solid motors, because of the complex combustion process that is regulated by a large diffusion flame. For example, hybrid motors using polymeric fuels such as HTPB are characterized by a regression rate that is generally one order of magnitude lower than the one of solid motors. Therefore, a large burning area is required to produce the fuel mass flow that is needed to obtain the design thrust. The desired area could be achieved using a long combustion chamber, but this would imply a very long motor. Furthermore, the web thickness that results from the low regression rate is small, causing a poor volume loading. A large burning area can be achieved in a better way if multiport grains are used, as shown in figure 1.6, but this approach implies some disadvantages like structural issues,

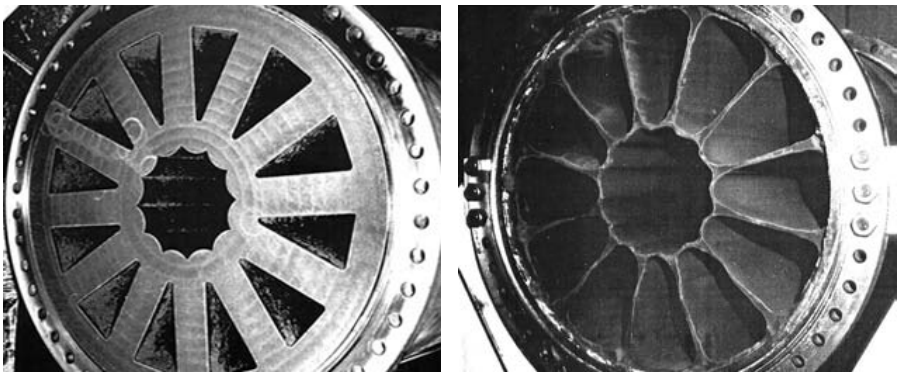

Figure 1.7: Multiport solid fuel grain of a hybrid rocket motor before (left) and after (right) a firing test [2]

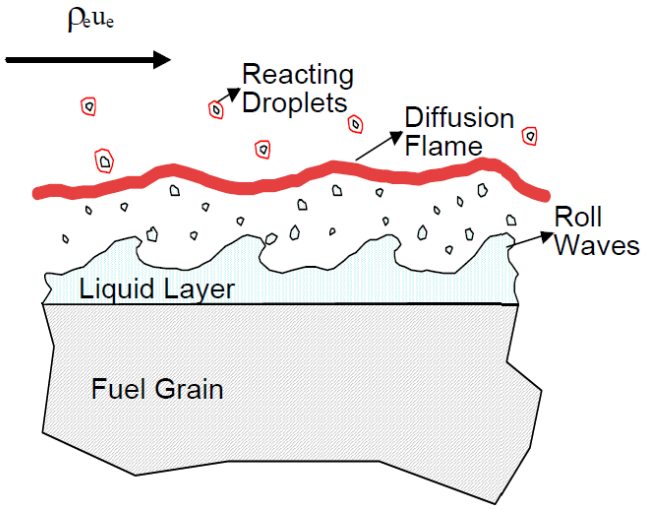

Figure 1.8: Simplified model of paraffin-based fuel combustion in hybrid rocket motors [58]

increased inert mass like web supports, increased manufacturing costs, increased injection complexity, port shape changing during burning time and different regression rate between ports. Moreover, multiport grains cannot burn completely, in order to avoid the separation of the fuel web supports that would cause the blocking of the nozzle. For this reason, a certain quantity of unburnt fuel slivers remains at the end of the combustion time, as it can be seen in figure 1.7. Several solutions have been proposed recently and two in particular look promising and have almost reached the operational status [32, 89]. The first solution was developed at Stanford University by Karabeyoglu and consist in the use of liquefying fuels like paraffin-based mixtures to manufacture the grain. This new class of fuels shows a characteristic behavior during the combustion process, because it forms a very thin hydro-dynamically unstable liquid film, with low viscosity and low surface tension, on the melting fuel sur-

face. The oxidizer flow causes the entrainment of small droplets from the liquid-gas interface, as shown in figure 1.8. The added mass transfer mechanism increases the fuel mass flow up to three-to-four times compared to conventional hybrid motors fuels [58, 59]. The operating principle of the second approach is to alter the classical flow field in the combustion chamber, in order to improve the heat transfer to the surface of the fuel grain and consequently increase the regression rate. To obtain a new flow structure, Yuasa experimented a hybrid motor with a swirl injector placed at the fore end of the motor. The configuration is characterized by a tangential oxidizer injector located at the motor head end, used together with a cylindrical fuel grain with a circular port. With this approach, a regression rate about three times greater than that for classical axial flow hybrid motors was found [110, 116, 117].

LOW COMBUSTION EFFICIENCY In hybrid motors the oxidizer and the fuel enter the combustion chamber from two different sides, namely the injector and the grain burning area. The consequence is that the combustion is limited by the diffusion of the chemical reactants towards the flame region. Here the propellants need to mix together and reach a mixture ratio close to the stoichiometric value before being able to burn together. In the classical hybrid motor configuration the flow field is highly stratified and it causes an incomplete mixing of the oxidizer with the fuel. As a consequence, the specific impulse decreases compared to the theoretical value due to the lower combustion efficiency. To assure a complete mixing and combustion of the reactants, it is possible to use a post-combustion chamber between the fuel grain and the nozzle, in order to increase the residence time of the chemical species inside the rocket motor. Another effective solution is to induce a strong level of turbulence in the flow field. The increased turbulence can be obtained, for example, by mean of a diaphragm or a mixing plate [19, 20, 47], or if a swirl injector is used, since it creates a helical flow field inside the combustion chamber that enhances the mixing of the chemical species along the motor [15, 50, 85].

MIXTURE RATIO SHIFT Considering a classical cylindrical fuel grain with a circular port, namely a side-burning grain, the fuel port area enlarges during the burning time. This process causes an enlargement of the burning surface but also a variation of the regression rate. The two effects are generally not balanced and the result is a decrease in the fuel production rate. Therefore, the mixture ratio varies during the burning time with the consequence that the average specific impulse decreases during the firing of the motor, as shown in figure 1.9.

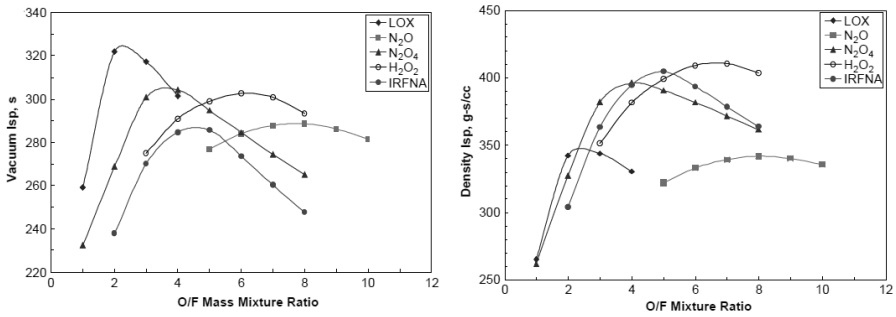

Figure 1.9: Variation of specific impulse (left) and volumetric specific impulse (right) with mixture ratio for HTPB solid fuel burning with different oxidizers [32]

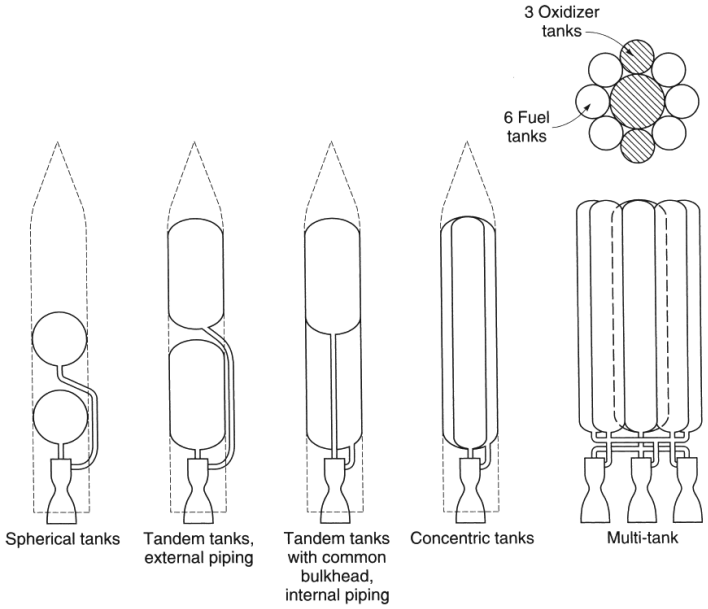

Figure 1.10: Simplified sketches of typical tank arrangements for large turbopump-fed liquid propellant rocket engines [109]

PACKAGING ISSUES Compared to liquid and solid motors, hybrid motors are generally not very flexible concerning the motor configuration. Liquid motors are mainly composed by the tanks where the propellant is stored, especially for systems with a low thrust to total impulse ratio like spacecraft motors, while the combustion chamber is relatively small because its geometry is related almost only to the thrust and not to the total impulse. As it can be seen in figure 1.10, tanks can assume very different configurations in order to be packaged in the best way according to the motor design. In solid motors the largest part of the system is composed by the combustion chamber, where the fuel grain is cast, which has a flexible configuration thanks to the possibility of tailoring the regression rate and adapting the grain shape. Therefore, it is possible to obtain several configurations to

meet the geometrical requirements and the mission constraints. Hybrid rocket motors have both a liquid oxidizer and a solid fuel. The former can be easily stored with flexibility like in liquid motors. The latter is what causes packaging issues, because the dependency of the regression rate on the oxidizer mass flux puts geometrical constraints that reduce the possible configurations. The combustion chamber of hybrid motors is generally slender, with limitations on the minimum feasible aspect ratio [11].

SLOW TRANSIENTS Compared to a liquid motor with equivalent thrust, the combustion chamber of a hybrid motor is much bigger because the fuel grain is enclosed inside. Furthermore, the internal volume changes with time due to the consumption of the fuel grain and the same happens to the thermal lag inside the solid fuel [4, 55]. The consequence is that the ignition transient and the response to throttling are generally slower in a hybrid motor. In most applications this aspect can be neglected, since reproducibility is generally more important than speed of response. However, hybrid rocket motors cannot be used when fast, accurate and repeatable response is required, for example if the motor has to operate in multipulse mode.

Liquid motors usually have the highest specific impulse, can be randomly throttled and can be stopped and restarted multiple times. Solid motors have a simple design, with none or only few moving parts, are ready to operate quickly and usually have the highest volumetric specific impulse. Hybrid rocket motors offer a compromise in performance and have long been considered an intermediate case between the two, without showing a clear advantage. But liquid motors have a complex and expensive design with all the required turbo-machinery, tanks and plumbing parts. Solid motors cannot be throttled or stopped and restarted, and a failure can be catastrophic with a great potential of explosion. Hybrid rocket motors are an attractive alternative for their unique features in a world becoming more careful about safety, costs and environmental impact.

1.1 SMALL SPACE MOTORS APPLICATIONS

Currently, hybrid rocket propulsion is not yet adopted for actual space missions. Due to the lack of widespread use for both military and commercial purposes, the available information on international researches is limited to conceptual designs and laboratory-scale firing tests. Considering a small space motor, typical applications have a thrust that ranges between 100 N and 1000 N. The motor thrust depends on both the required Δv for the mission and the size of the satellite and for this reason it can be scaled according to the payload weight. The most interesting possible applications are, for example,

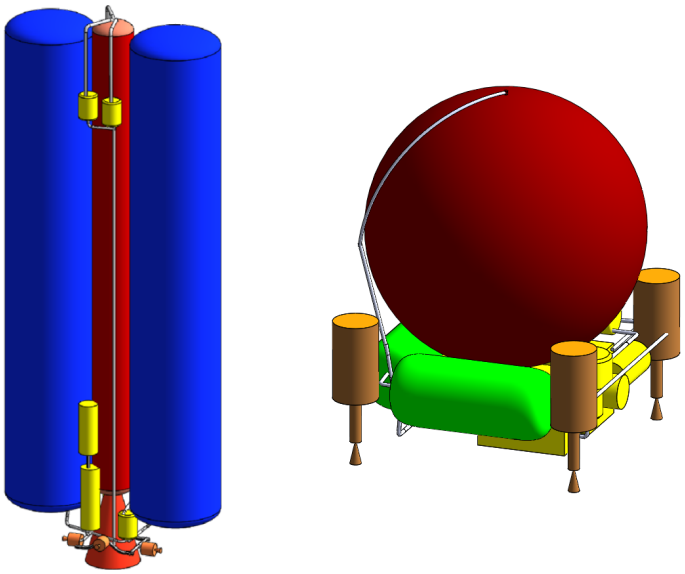

Figure 1.11: Hybrid propulsion system (left) and liquid monopropellant propulsion system (right) for a 25 kg spacecraft [49]

orbit insertion motors for small satellites [36, 37, 48, 49], orbit raising and station keeping motors for orbit transfer vehicles [24, 26, 71, 93, 115], reentry systems [39], and throttleable motors for planetary soft landing [88, 94].

At Jet Propulsion Laboratory, a remarkable work was done in the design of small hybrid propulsive units for different CubeSat and SmallSat missions. In particular, the CubeSat orbit insertion motor is interesting for the following analysis [36, 37, 48, 49]. A reference mission for Mars orbit insertion was selected and trades for different dedicated propulsion stages were done, with a total spacecraft and stage wet mass ranging from 25 kg to 100 kg. The propulsion system was designed in order to be capable of trajectory corrections on the way to Mars, Mars orbit insertion, and orbit clean-up maneuvers after the main engine burn, assuming it is released from its rideshare before cruise to Mars. The system was intended to be an independent propulsion stage, and as such it would be jettisoned prior to commencement of the spacecraft science mission. Afterwards, propulsion systems using a hybrid rocket motor as the main engine were compared to liquid monopropellant systems. The hybrid propulsion system was found to outperform the liquid monopropellant system, being typically able to deliver an extra 6 % of payload mass. The hybrid propulsion system for a 25 kg total spacecraft mass is presented in figure 1.11, compared with the equivalent liquid monopropellant propulsion system.

Orbit transfer vehicles are generating growing interest and one example is the SHERPA system, which was promoting responsive space in three major ways: allowing satellites to be stored on-orbit and then moved into position as needed; promoting reconfigurable and

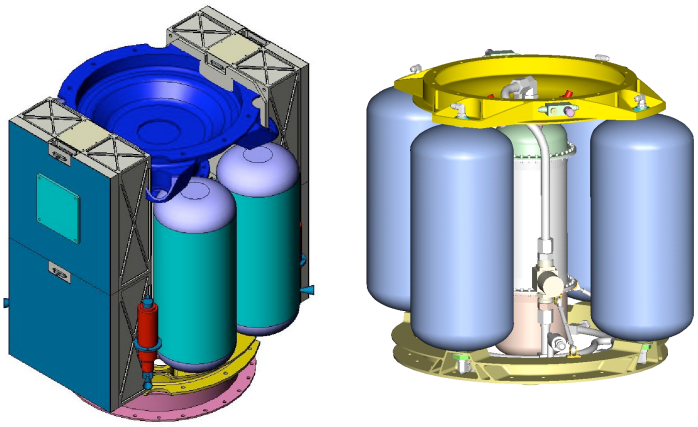

Figure 1.12: SHERPA orbit transfer vehicle (left) and hybrid propulsion module (right) [26, 93, 115]

maneuverable assets; producing a low cost space system that can be easily procured [26, 93]. It was designed with capability for multi orbit changes, station keeping, and deorbiting at the completion of a mission. The main propulsive module was developed by SpaceDev and it consisted of a hybrid motor with a central fuel grain made of PMMA and four oxidizer tanks surrounding it and filled with N_2O [115]. The hybrid motor had a specific impulse of 260 s and a maximum thrust of 222.4 N. The propulsion module mass was of 43 kg out of the 56 kg of total SHERPA mass. The whole transfer vehicle and the propulsion module can be seen in figure 1.12.

Other examples of orbit transfer motors are the ones studied by ESA or ONERA that were searching for alternatives to commonly used liquid rocket motors for apogee kick maneuvers [24, 71].

A hybrid motor approach was studied as reentry system for the Brazilian SARA satellite, which was conceived as a microgravity recoverable and reusable research platform [39]. The satellite is represented in figure 1.13 together with the hybrid deorbiting motor. Two different reentry motor configurations were proposed. The first hybrid motor relied on a self-pressurizing N_2O. The second option was more conventional, as it was based on hydrogen peroxide and on a pressurization subsystem. In both cases, paraffin was considered as the solid fuel. An injector plate based on pressure swirl atomizers was chosen for oxidizer injection into the combustion chamber. The main reentry mission requirement was to produce a deboost impulse capable of reducing the speed of the order of 235 m/s to 250 m/s, with a total burning time between 50 s and 200 s.

Another interesting application is planetary soft landing required for unmanned and manned missions, which have to deliver on planet surfaces always more heavy equipment and manned modules that cannot withstand strong impact loads or that need to maintain the landing place as unaltered as possible. Such approach is applicable

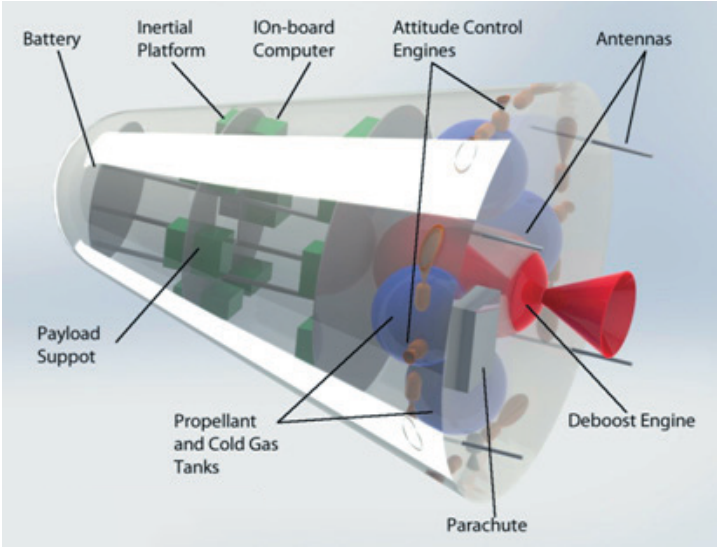

Figure 1.13: Conceptual design of the SARA platform [39]

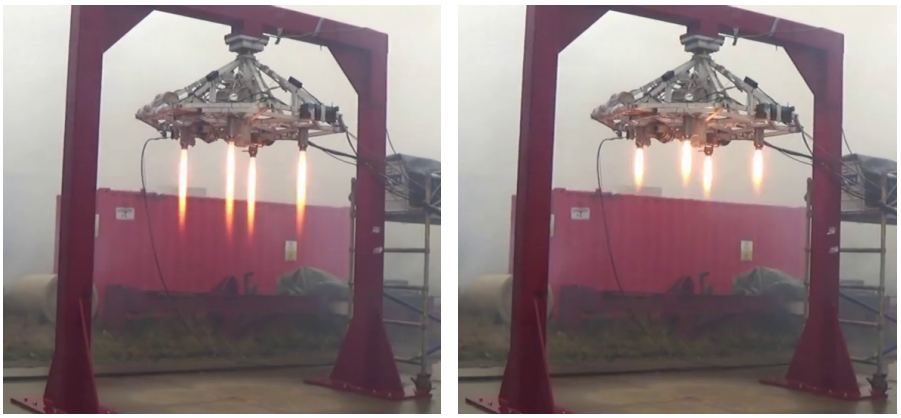

Figure 1.14: Throttling firing test of the SPARTAN lander [88, 94]

in the near future to both a return of the man on the Moon and to future Mars exploration missions. The SPARTAN research program, for example, relied on the hybrid motor technology, exploiting its capability of being throttled [88]. In figure 1.14 it is possible to see the results of throttling during a firing test, where the lander is mounted on the preliminary static test bench. The SPARTAN lander design was based on four hybrid rocket motors that used HTP as the liquid oxidizer and a proprietary HTPB-based polymer mixture as the solid fuel. The motor demonstrated a throttling ratio of 10 to 1 with tight thrust reproducibility [94].

1.2 PROJECT OBJECTIVE AND THESIS OUTLINE

In recent years there has been a significant renewed interest in hybrid propulsion for its unique features, in a world becoming more

careful about safety, costs and environmental impact. Unfortunately, this technology presents also several disadvantages, due to the characteristic diffusive flame mechanism. However, most of these drawbacks can be solved through a correct design process and choosing convenient approaches. This is not always a trivial work and this is the reason why, despite many efforts, most of the international contribution to this field is limited to conceptual designs and laboratory-scale firing tests. Therefore, the following research is focused on the development and testing of a small hybrid rocket motor, considering in particular its possible space applications. The final ambition of this work is to design a viable alternative to replace conventional propulsive systems, demonstrating its high performance and adaptability to different mission scenarios.

To achieve this goal, the following workflow is adopted. First, in order for hybrid rocket motors to be competitive, it is necessary to understand their peculiar behavior, especially related to the mixture ratio shift, and how the fuel grain shape and size are dependent on motor design parameters. Afterwards, it is fundamental to design a hybrid motor configuration that is simple and efficient. A CFD code should be used as a support in order to obtain the best results from the design process, since a numerical analysis can be a powerful instrument to predict the system operation. The design must be tested through an extensive experimental campaign, whose results are fundamental to refine the propulsive system and to calibrate the numerical simulations as well. Furthermore, the best configuration should be selected, depending on the intended application. Finally, the heavyweight design used for testing purpose needs to be converted in the flightweight version, taking into account new problems that arise during this process, like the thermal behavior of the system. In order to better understand the structure of the work that has been performed by the author, an outline of the thesis is presented hereunder.

In chapter 1 hybrid rocket motors are introduced and compared to conventional propulsive systems. Their inherent advantages ad disadvantages are discussed as well. Moreover, possible interesting applications are presented.

In chapter 2 the fundamental theory that explains the combustion process of hybrid rocket motors is presented.

In chapter 3 a set of simple explicit analytic equations to describe the hybrid rocket behavior and motor sizing are derived, in order to have a better sensibility on the trends, possibilities, and limits of this promising but tricky kind of propulsion system.

In chapter 4 two different motor configurations are designed and numerically verified, in order to develop hybrid rocket motors with high regression rate and high combustion efficiency.

In chapter 5 the results of a thorough experimental analysis are presented and discussed, after a description of the experimental setup that has been used during the whole test campaign.

In chapter 6 a simple approach that is useful to decide which motor configuration is best suited to the intended space application is proposed. The problems that arise when designing the flightweight version of the same heavyweight motor are also discussed.

In chapter 7 the conclusions are finally presented.

2

HYBRID COMBUSTION THEORY

In a classical hybrid rocket motor configuration the oxidizer is injected into the combustion chamber from the head end of the motor and flows over the fuel surface. After the ignition of the motor, a macroscopic diffusion flame develops above the solid grain. The heat released from the reaction of combustion increases the temperature of the fuel grain until the surface decomposes due to pyrolysis. The vaporized fuel and the gaseous oxidizer are transported by convection and diffusion to the flame. Here the gases mix together and react, sustaining the combustion. A detailed model of the physical processes involved in the hybrid combustion, namely the interface energy flux balance, the chemical species mass flux balance and the overall mass flux balances, is represented in figure 2.1.

All the physical processes of hybrid combustion take place inside the boundary layer, which is defined as the layer of fluid close to the surface where the effects of viscosity are significant and thus not negligible. On the other hand, outside the boundary layer the fluid flow can be approximated as inviscid. For each specific variable it is possible to define a related boundary layer where large gradients occur: the velocity is affected by friction inside the momentum boundary layer, where the flow has to slow down to fulfill the condition of no-slip at the wall; the temperature changes from the free stream value to the surface temperature inside the thermal boundary layer; the chemical concentration changes from the free stream value to the value at the wall inside the species boundary layer.

It is possible to start considering the general conservation equation in the eulerian form for a general fluid unknown:

$$\frac{\partial \Phi}{\partial t} + \mathbf{v} \cdot \boldsymbol{\nabla} \Phi = D_\Phi \boldsymbol{\nabla}^2 \Phi + S_\Phi \tag{2.1}$$

The first term represents the time variation of the quantity Φ, the second one is the convective transport of Φ, the third term is the diffusion of Φ, and the last one represents a source or sink for the variable Φ. Velocity, temperature, chemical concentration and all the other fluid unknowns follow the same equation, suggesting a similar behavior for all of them. This is the basis of the Reynolds analogy, which states that under specific conditions the solutions to the conservation equation are similar, implying that all the fluid quantities follow the same profile. The profiles of different fluid unknowns can be related to each other by means of adimensional parameters, defined as the ratio between the diffusive transport of Φ_1 and the diffusive transport of Φ_2, which also represents the ratio between

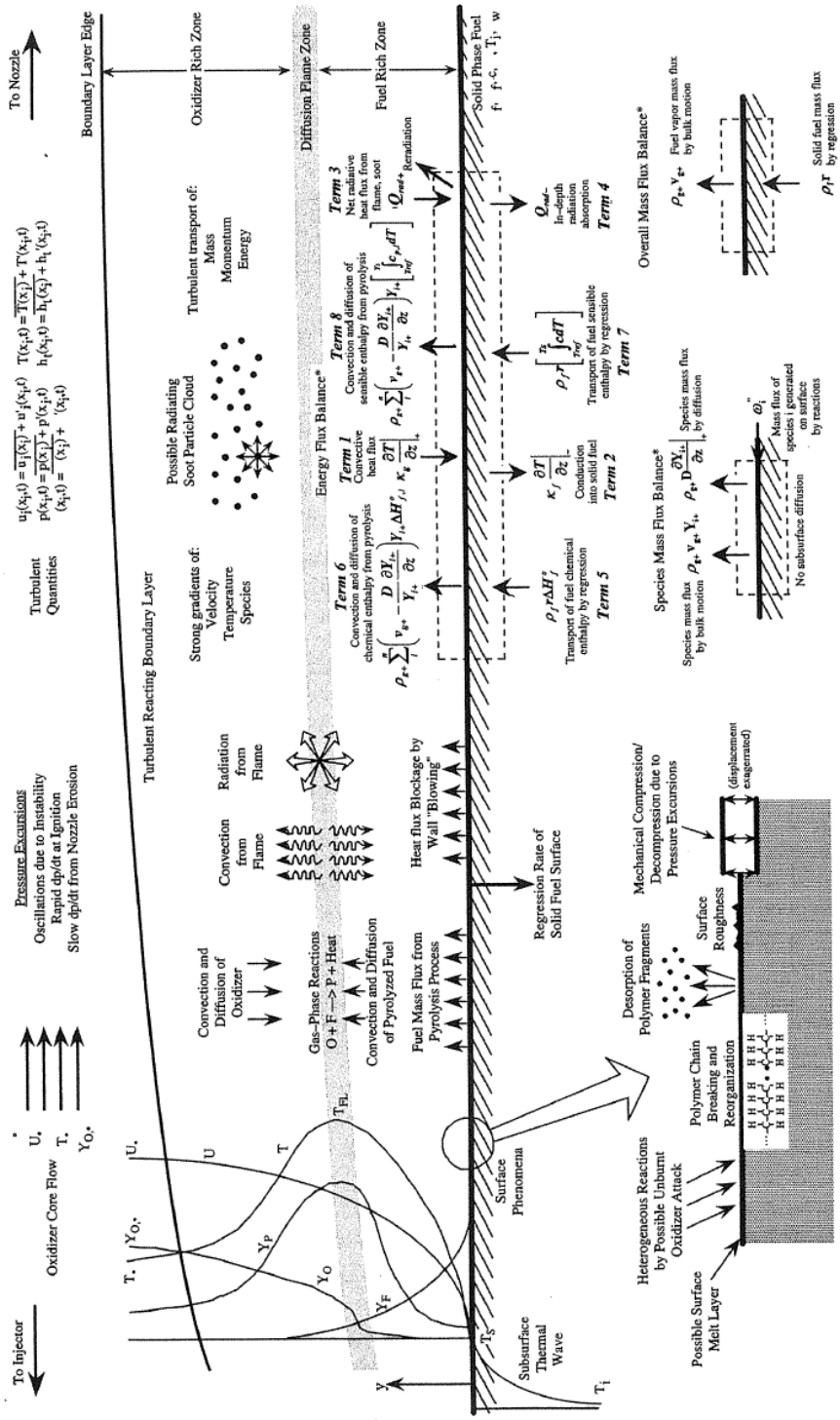

Figure 2.1: Physical processes involved in hybrid combustion [32]

the thicknesses of the different boundary layers. Some adimensional parameters of interest for the following discussion are, for example, the Prandtl number, the Lewis number and the Schmidt number:

$$Pr = \frac{\text{momentum diffusivity}}{\text{thermal diffusivity}} = \frac{\nu}{\alpha} = \frac{\mu c_p}{\lambda} \tag{2.2}$$

$$Le = \frac{\text{thermal diffusivity}}{\text{mass diffusivity}} = \frac{\alpha}{D} = \frac{\lambda}{\varrho c_p D} \tag{2.3}$$

$$Sc = \frac{\text{momentum diffusivity}}{\text{mass diffusivity}} = \frac{\nu}{D} = \frac{\mu}{\varrho D} = PrLe \tag{2.4}$$

Thanks to the Reynolds analogy, the profile of only one fluid unknown is needed, while the others can be scaled according to the adimensional parameters and the boundary layer values. Moreover, if the profiles of different variables are similar, the same happens to their derivatives. An important consequence of the Reynolds analogy is that it is possible to obtain the heat flux from the shear stress, where the former is proportional to the thermal gradient and the latter is proportional to the velocity gradient:

$$\dot{q} = -\lambda \frac{\partial T}{\partial y} \tag{2.5}$$

$$\tau = \mu \frac{\partial v}{\partial y} \tag{2.6}$$

This technique is widely used to solve heat transfer problems knowing the solution of the momentum equation. It has been used by Marxman as well to develop its hybrid combustion theory and a correlation for the regression rate of the solid fuel grain.

2.1 REGRESSION RATE MODEL

The fundamental theory that explains the combustion process of hybrid rocket motors, and consequently the regression of the solid fuel grain, was developed in the early Sixties by Marxman, who based the analysis on the turbulent boundary layer combustion over a flat surface [74–77]. The assumption is that the boundary layer is turbulent and the combustion occurs in an infinitely thin flame zone, located where the reagents concentration goes to zero. This is the so-called flame-sheet approximation, which is exact only in a laminar boundary layer with an infinite reaction rate, but is acceptable also in a turbulent boundary layer even if there are temporal and spatial fluctuations of the flux quantities. Experimental observations estimate the flame thickness to be about 10 % of the boundary layer thickness and the flame position above the fuel surface to be approximately 10 % to 20 % of the boundary layer thickness, not exactly where the concentration of the combustion reactants equals the stoichiometric conditions [75]. However, for typical operating conditions of hybrid rocket motors,

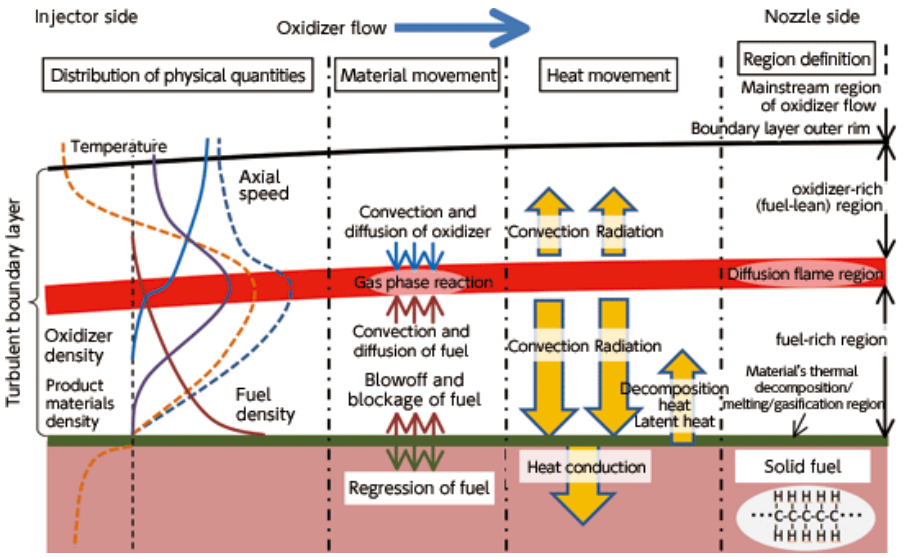

Figure 2.2: Boundary layer structure in hybrid rocket motors

the chemical reactions rate is much greater than the reactants mixing rate in the turbulent flame. For this reason it is possible to consider the combustion as controlled by diffusion and occurring with an infinite fast rate at the flame. This is represented by a large Damköhler number, which is defined as the ratio between the turbulent time scale and the chemical time scale:

$$Da = \frac{\tau_t}{\tau_c} \gg 1 \tag{2.7}$$

Looking at the boundary layer schematically represented in figure 2.2, the model allows to divide the layer in two different regions separated by the flame-sheet. In the upper zone the oxidizer that comes from the external flow diffuses through the combustion products to the position where the flame develops, while in the lower zone the fuel vaporizes from the grain surface and migrates upwards.

The starting point for developing a regression rate model is to assume for simplicity a slab configuration at a steady state condition and to consider a simplified heat balance at the fuel surface. In this configuration the heat flux to the wall surface is equal to the sum of the heat required for the fuel vaporization and the heat conducted inside the solid grain:

$$\dot{q}_w = \dot{r}\varrho_f L_v + \dot{q}_{cond} \tag{2.8}$$

It is possible to demonstrated that the energy lost for conduction is equal to the heat required to heat up the solid fuel from the initial temperature to the wall temperature. It is then possible to rewrite the heat balance at the surface introducing the effective heat of vaporization:

$$\begin{aligned} \dot{q}_w &= \dot{r}\varrho_f L_v + \dot{r}\varrho_f c(T_w - T_{in}) \\ &= \dot{r}\varrho_f [L_v + c(T_w - T_{in})] = \dot{r}\varrho_f h_v \end{aligned} \tag{2.9}$$

The wall heat flux is composed by a convective term and a radiative one. In the classical hybrid combustion theory the radiative component is neglected because in typical operating conditions the convective heat flux is predominant. However, a correction was later introduced to take into account also the contribution of radiation to the wall heat flux [75]. Another assumption is to set the Prandtl number and the Lewis number equal to one, implying also a unitary Schmidt number. This hypothesis is made frequently for turbulent flows of gas mixtures and forces the same thickness of the thermal boundary layer, the momentum boundary layer and the species boundary layer. Another strong assumption is to treat the fluid as incompressible. Even if it is an incorrect hypothesis it is acceptable to simplify a very complex process. Therefore, it is possible to rewrite the expression of the wall heat flux relating this fluid unknown to the wall shear stress:

$$\dot{q}_w = \dot{q}_{conv} + \cancel{\dot{q}_{rad}} = -\lambda \frac{\partial T}{\partial y} = -\frac{\lambda}{c_p}\frac{\partial h}{\partial y} = -\mu \frac{\partial h}{\partial y} \tag{2.10}$$

In order to proceed with the mathematical treatment, the Reynolds analogy has to be applied between the fuel surface and the flame-sheet. As previously stated, with this method it is possible to obtain the heat flux from the shear stress:

$$\frac{\dot{q}_w}{h_{fl} - h_w} = \frac{\tau_w}{v_{fl} - v_w} \tag{2.11}$$

Applying the no-slip condition, which imposes a zero velocity at the wall to viscous fluids, the last equation can be rewritten as:

$$\dot{q}_w = \tau_w \frac{h_{fl} - h_w}{v_{fl}} \tag{2.12}$$

The wall shear stress can be related to the skin friction coefficient and to the fluid properties at the outer edge of the boundary layer:

$$\tau_w = \frac{1}{2}\varrho_e v_e^2 C_f \tag{2.13}$$

Using this correlation it is possible to obtain the following expression of the wall heat flux:

$$\dot{q}_w = \frac{1}{2}\varrho_e v_e C_f \frac{v_e}{v_{fl}}\left(h_{fl} - h_w\right) \tag{2.14}$$

Remembering the equation of the heat balance at the surface, it is possible to rewrite the previous expression:

$$\dot{r}\varrho_f h_v = \frac{1}{2}\varrho_e v_e C_f \frac{v_e}{v_{fl}}\left(h_{fl} - h_w\right) = \frac{1}{2}\varrho_e v_e C_f \frac{v_e}{v_{fl}}\Delta h \tag{2.15}$$

The enthalpy difference expression can be generalized to include heterogeneous chemical reactions at the surface of the solid fuel. This

assumption is supported by experimental findings that confirmed the presence of a non-negligible quantity of oxidizer in the zone beneath the flame, which can cause chemical reactions like oxidizer attack at the grain wall [76].

Up to now, the vertical fuel flow that comes from the vaporizing grain surface has not been introduced yet. This phenomenon is called blowing and it alters the velocity and temperature profiles with respect to the case without blowing, stretching the boundary layer and increasing its thickness. For this reason, the velocity and temperature gradients are reduced and consequently the shear stress and the heat flux decrease. The blowing parameter is an adimensional number that describes the flow over a blowing surface and it is determined as the ratio between the vertical and the horizontal flows:

$$B = \frac{\dot{m}_f}{\frac{1}{2}\varrho_e v_e C_f} \tag{2.16}$$

In a hybrid rocket motor this parameter depends only on the oxidizer mass flow becuase the regression of the fuel surface is regulated by the fluid dynamics of the boundary layer. Introducing the blowing parameter, the expression of the mass flux from the wall becomes:

$$\dot{r}\varrho_f = \frac{1}{2}\varrho_e v_e C_f B \tag{2.17}$$

$$B = \frac{v_e}{v_{fl}}\frac{\Delta h}{h_v} \tag{2.18}$$

The blowing parameter, which depends only on the thermochemical properties of the propellants used, has a dual nature: it represents a similarity parameter of a boundary layer with mass flux from the wall, as well as a thermodynamic parameter quantifying the fuel regression caused by the enthalpy difference between the flame and the fuel surface. As a consequence, a constant blowing parameter and a unitary Lewis number imply that the momentum profile, the species profile and the enthalpy profile are similar.

Moreover, it is possible to determine the velocity ratio and the position of the flame, assuming as a first approximation that the flame is established where the chemical reactants concentration reaches the stoichiometric condition, with a treatment that is omitted here for the sake of brevity:

$$\Phi_{fl} = \frac{v_{fl}}{v_e} = \frac{\varphi\frac{\Delta h}{h_v}}{X_{ox_e} + (\varphi + X_{ox_e})\frac{\Delta h}{h_v}} \tag{2.19}$$

$$\eta_{fl} = \frac{y_{fl}}{\delta} = \left[\frac{\sqrt{1 + 2B\Phi_{fl}\left(1 + \frac{B}{2}\right)} - 1}{B}\right]^{\frac{1}{n}} \tag{2.20}$$

However, experimental measurements confirm that the flame is on the fuel rich side and that it burns at a slightly lower mixture ratio and

at a lower position [75]. This result can be explained by the several approximations of the model developed by Marxman.

The introduction of the skin friction coefficient allows to solve the heat transfer problem using the extensive amount of data in the literature about friction in a turbulent boundary layer. The value of the skin friction coefficient in a boundary layer with blowing from the wall is computed from its value in the case without blowing, obtained using an empirical correlation developed for a turbulent incompressible flow over a flat plate:

$$C_f = \frac{C_f}{C_{f_0}} C_{f_0} \tag{2.21}$$

$$\frac{C_{f_0}}{2} = 0.029 Re_x^{-0.2} \tag{2.22}$$

where the local Reynolds number is defined as:

$$Re_x = \frac{\varrho_e v_e}{\mu_e} x \tag{2.23}$$

The ratio C_f/C_{f_0} represents the reduction of the skin friction coefficient due to the wall blowing. It can be expressed as a function of the blowing parameter only that has to meet the conditions of $C_f/C_{f_0} = 1$ for $B = 0$ and $C_f/C_{f_0} \to 0$ for $B \to \infty$:

$$\frac{C_f}{C_{f_0}} = \left[\frac{\ln(1+B)}{B}\right]^{0.8} \left[\frac{1 + \frac{13}{10}B + \frac{4}{11}B^2}{(1+B)\left(1+\frac{1}{2}B\right)^2}\right]^{0.2} \tag{2.24}$$

However, this analytical expression can be approximated with a numerical fit valid over a wide interval of the blowing number, or using a more accurate expression later developed by Altman that is valid in the range of typical operating conditions of hybrid rocket motors [3]:

$$\frac{C_f}{C_{f_0}} = 1.27 B^{-0.77} \quad \text{for } 5 \leq B \leq 100 \tag{2.25}$$

$$\frac{C_f}{C_{f_0}} = B^{-0.68} \quad \text{for } 5 \leq B \leq 20 \tag{2.26}$$

It is worth noting that both numerical fits provide the correct asymptotic value for $B \to \infty$, but not for $B = 0$ where $C_f/C_{f_0} \to \infty$.

At this point all the quantities are known and substituting them in equation (2.17) it is possible to obtain the following expression:

$$\dot{r}\varrho_f = 0.029 \left(\frac{\mu_e}{x}\right)^{0.2} (\varrho_e v_e)^{0.8} B^{0.32} \tag{2.27}$$

Approximating the product $\varrho_e v_e$ with the local mass flux G:

$$\dot{r}\varrho_f = 0.029 \left(\frac{\mu_e}{x}\right)^{0.2} G^{0.8} B^{0.32} \tag{2.28}$$

and combining all the terms that are constant as a first order approximation, the last equation becomes:

$$\dot{r} = a_1 G^{0.8} x^{-0.2} \tag{2.29}$$

It is now possible to average the regression rate expression over the solid grain length and the burning time, obtaining the space-time averaged form of the regression rate law [60]:

$$\dot{r} = a_2(\varphi) G^{0.8} L^{-0.2} \tag{2.30}$$

$$\dot{r} = a_3(\varphi) G_{ox}^{0.8} L^{-0.2} \tag{2.31}$$

where the oxidizer mass flux is defined as:

$$G_{ox} = \frac{\dot{m}_{ox}}{A_p} \tag{2.32}$$

Both the equations correspond to the general expression that fits the experimental data and this result confirms the validity of the basic principle of the theory developed by Marxman:

$$\dot{r} = a_4(\varphi) G_{ox}^{n} L^{m} \tag{2.33}$$

The values of the coefficient a and of the exponents n and m are obtained through experimental data, because they are different from the ones predicted by the theory developed by Marxman, considering all the assumptions and approximations introduced to obtain a solution. Finally, it is possible to include the mixture ratio correction and the effect of the fuel grain length in the coefficient a:

$$\dot{r} = a G_{ox}^{n} \tag{2.34}$$

Analyzing equations (2.17), (2.18) and (2.28), it is possible to notice that the blowing number and consequently the regression rate are proportional to the enthalpy ratio $\Delta h / h_v$, which is essentially fixed by the choice of the propellant combination. This behavior can be explained considering that a higher enthalpy difference between the grain surface and the flame causes higher thermal gradients and thus a higher heat flux, whereas a lower effective heat of vaporization results in a lower energy necessary to vaporize the solid fuel. But since the blowing parameter is raised to a small power, even large variations of the enthalpy ratio have a small influence on the regression rate. This happens because a higher regression rate causes an increase of the fuel mass injected from the grain wall into the boundary layer that reduces the convective heat transfer to the surface, which in turns leads to a consequent decrease of the regression rate, and so forth. This phenomenon is the so-called blocking effect.

Looking again at equation (2.28), it is possible to notice that the expression of the regression rate found by Marxman is dependent on the local mass flux. This quantity is evaluated as the sum of the

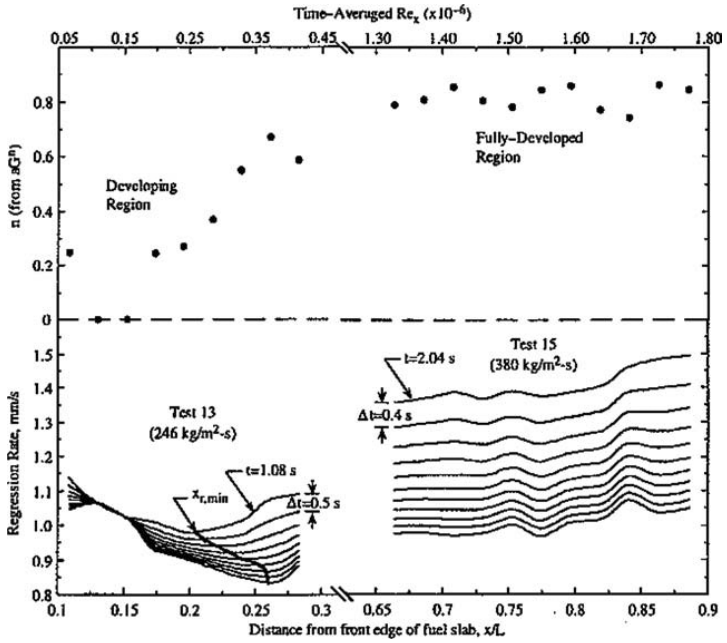

Figure 2.3: Regression rate of a lab-scale hybrid rocket motor [34]

oxidizer injected from the head end of the motor and of the fuel added from the blowing grain surface. For this reason, the local mass flux increases along the motor length. However, the regression rate law has also a negative dependence on the axial position. This can be explained considering that the increase of the boundary layer thickness causes a decrease of the heat transfer between the flame and the fuel surface. The presence of this two opposite effects results in the existence of a minimum regression rate location, as it can be seen in figure 2.3 that summarizes the results of the experimental tests conducted by Chiaverini to analyze the internal ballistics of a lab-scale hybrid rocket motor [34]. From the head end of the grain until the point of minimum the regression rate decreases due to the growing of the boundary layer, whereas downstream the point of minimum the increase of the local mass flux leads to a higher regression rate. The result of this two opposite effects is a slow variation of the regression rate along the axial position. Furthermore, this smooth trend is also enhanced by a self-compensating mechanism: the local enlargement of the port area causes a decrease of the local mass flux and consequently of the local regression rate. This is an advantage compared to the coupling among burning area, mass flow, chamber pressure and regression rate in solid rockets, which can lead to a catastrophic failure due to a variation of the burning area.

The local mass flux also decreases during the burning time due to the enlargement of the port area, leading to a similar variation of the regression rate with time. This phenomenon causes the shift of the point of minimum regression rate to axial positions further downstream, because the effect of the local mass flux on the regression

rate is more important than the one of the axial position. For this reason, the decrease of the local mass flux enhances the effects of the growing boundary layer.

Moreover, the regression rate correlation developed by Marxman has a dependence on the scale of the motor. As the term that represents the length of the motor is raised to a negative power, the regression rate decreases for longer motors. This behavior is the opposite of the desired one because bigger motors require a faster regression rate to have high volume loading.

It is important to note that the space-time averaged form of the regression rate law is generally more accurate than the local one. The reason is that the local form has a singularity for $x \to 0$, while the actual regression rate has a finite value. At the head end of the motor the regression rate is strongly dependent on the flame-holding mechanism and on the injection type [23, 27–29, 90]. All this effects are even more relevant for fuel grains with a low aspect ratio.

2.2 THERMAL RADIATION EFFECTS

The radiative component of the wall heat flux is not always negligible compared to the convective one. For example, this is the case of solid grains with a high percentage of metal additives or solid fuels that produce a high amount of soot. Marxman later introduced a correction to the regression rate model, in order to add the radiation contribution caused by the gas-phase combustion products [75]. First, it is necessary to define the convective heat flux and the radiative heat flux as follows:

$$\dot{q}_{conv} = 0.036 h_v \left(\frac{\mu_e}{x}\right)^{0.2} G^{0.8} B^{0.32} \tag{2.35}$$

$$\dot{q}_{rad} = \sigma \varepsilon_w \left(\varepsilon_g T_{fl}^4 - \alpha_g T_w^4\right) \tag{2.36}$$

The radiative component of the wall heat flux is defined by two terms: the first one is the radiative heat flux emitted by the flame and absorbed by the wall, while the second one is the radiative heat flux emitted by the fuel surface and absorbed by the flame. The second term is generally negligible compared to the first one, because in hybrid rocket motors the typical temperature of the flame is around 3000 K while the surface has a temperature of about 1000 K and the zone where the gas-phase reactions occur has a comparable emissivity and absorptivity.

It is now possible to write the expression of the regression rate for a system where both the convective and the radiative heat transfer are included:

$$\dot{r}\varrho_f = \frac{1}{h_v}\left[\dot{q}_{conv} \exp\left(-0.75 \frac{\dot{q}_{rad}}{\dot{q}_{conv}}\right) + \dot{q}_{rad}\right] \tag{2.37}$$

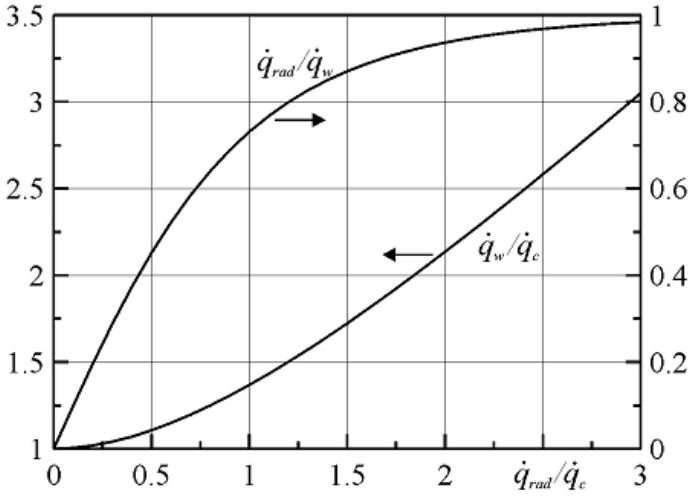

Figure 2.4: Coupling between convective and radiative heat fluxes [77]

Due to the intrinsic blocking effect, a weak radiative heat flux has a small effect on the total wall heat flux and consequently on the regression rate. The explanation is that a higher total wall heat flux causes an increase of the regression rate, which translates into a higher blowing from the fuel surface that in turn causes the blocking of a larger portion of the convective heat flux. This is confirmed by experiments conducted by Marxman, showing that the regression rate experiences only a 10 % increase when a radiative flux with a magnitude of half the convective heat flux is added [77]. This behavior suggests that the effect of radiation is almost always negligible. An exception is the case of metallized fuels, where the radiative heat transfer from the particles contributes significantly to the regression rate. When the radiative heat flux is equal to the convective term in the case without radiation, the total wall heat flux is only 47 % higher, due to the decrease of the convective heat flux caused by the blocking effect. The coupling among the convective heat flux, the radiative heat flux and the total wall heat flux is shown in figure 2.4.

It is important to note that soot and other solid particles behave nearly as black bodies, while the gaseous molecules release radiation energy only in specific emission bands related to their excited states. The emissivity of the gas-phase is dependent on the number of molecules for unit of volume and so is related to the pressure:

$$\varepsilon_g = 1 - e^{-k_g DP} \tag{2.38}$$

This means that with an increasing pressure the influence of the radiative heat flux becomes more important. When the radiative flux is the dominant part of the total wall heat flux, the regression rate is no longer dependent on the mass flux.

Strand tested a lab-scale hybrid rocket motor in order to analyze the radiative heat flux originated from both the gas-phase and the soot

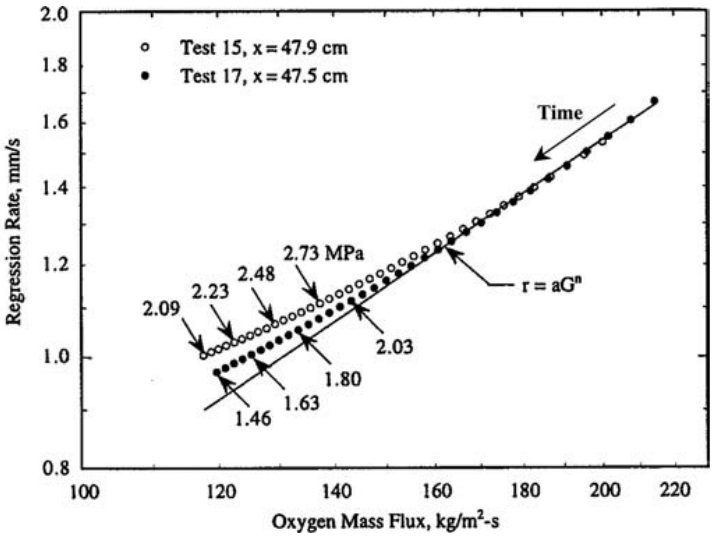

Figure 2.5: Effect of the pressure on the regression rate [34]

particles [108]. The gas-phase radiation and the soot radiation were estimated using empirical expressions:

$$\dot{q}_{rad_g} = \sigma T_g^4 \left(1 - e^{-k_g DP}\right) \tag{2.39}$$

$$\dot{q}_{rad_s} = \sigma T_g^4 \left(1 - e^{a_p N_p}\right) \tag{2.40}$$

where the gas-phase absorption coefficient k_g is dependent on the pressure and the term $a_p N_p$ is a function of the particles weight fraction, the mixture ratio and the pressure:

$$k_g = 9.33 \times 10^{-4} - 6.19 \times 10^{-6} P + 1.79 \times 10^{-8} P^2 \tag{2.41}$$

$$a_p N_p = 0.134 \left(\frac{\alpha_p P}{1 + \varphi - \alpha_p}\right) \tag{2.42}$$

The result of the experimental campaign was that the radiative heat flux is more than 50 % of the total wall heat flux when both the gas-phase term and the soot one are included.

Chiaverini found that the radiative heat flux plays an important role in the regression rate of a hybrid rocket motor burning HTPB with GOX [33, 34]. Figure 2.5 shows how the pressure influences the regression rate. In the zone of low mass flux a higher radiative heat flux causes an increase of the regression rate at higher pressures. Moreover, the regression rate becomes less dependent on the total mass flux. Starting from the results of Strand, it was possible to find that the radiation due to soot presence is about 80 % of the total radiative heat flux:

$$\dot{q}_{rad_s} = \sigma T_g^4 \left(1 - e^{-k_s}\right) \tag{2.43}$$

where the soot absorption coefficient k_s is related to the mixture ratio:

$$k_s = 0.51 - 0.113\varphi \tag{2.44}$$

From this expression it is possible to see that the soot emissivity decreases with the increase of the mixture ratio. The explanation is that there is more oxidizer ready to burn with the fuel produced by the pyrolysis of the solid grain. Moreover, Chiaverini demonstrated that the total heat flux curve has nearly the same shape as the convective heat flux curve but differs in magnitude, so the radiation cannot be ignored for non-metallized fuels as previously thought. However, this study was related to HTPB burning with GOX, while other propellant combinations could present a much lower soot formation.

2.3 CHEMICAL KINETICS EFFECTS

The results of the regression rate model proposed by Marxman are based on the hypothesis that for typical operating conditions of hybrid rocket motors the Damköhler number is very high, meaning that the chemical reactions rate is much greater than the mixing rate of the reactants in the turbulent flame. However, in the operating region of very high mass fluxes this approximation is not valid anymore because the residence time of the gases in the combustion chamber largely decreases at higher oxidizer injection velocities. Therefore, in this region it is necessary to take into account also the chemical kinetics that causes a reduction of the regression rate. Moreover, the pressure influences the regression rate because the chemical reaction rate becomes higher at increasing pressures. The regression rate dependence on the pressure at very high mass fluxes is caused by two phenomena: the kinetics of the gas-phase reactions between the oxidizer and the pyrolyzed fuel, and the kinetics of the heterogeneous reactions between the oxidizer and the solid fuel at the grain surface.

Wooldridge and Marxman derived a normalized regression rate expression dependent on the Damköhler number, which to recall is defined as the ratio between the turbulent time scale and the chemical time scale.

$$Da = \frac{\tau_t}{\tau_c} \gg 1 \tag{2.45}$$

Taking into account the chemical kinetics of both the gas-phase reactions and the heterogeneous reactions, it is possible to obtain:

$$\frac{\dot{r}}{\dot{r}_0} = (2Da)^{0.5}\left\{1 - Da\left[1 - \exp\left(-\frac{1}{Da}\right)\right]\right\}^{0.5} \tag{2.46}$$

where the reference regression rate is computed in the region of pressure independence. The correlation is plotted in figure 2.6.

The chemical kinetics is the limiting parameter when the Damköhler number is high. This happens when the combustion chamber pressure is low or when the mass flux is high. In this region the previous equation simplifies to:

$$\frac{\dot{r}}{\dot{r}_0} = (2Da)^{0.5} \tag{2.47}$$

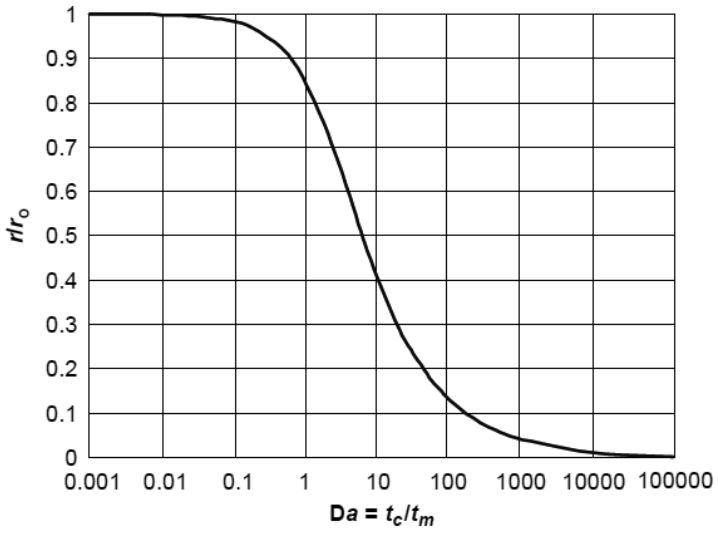

Figure 2.6: Effect of the Damköhler number on the regression rate [32] (note that in the reference this parameter is defined inversely to the one used in the text)

If a second-order reaction is considered, the Damköhler number can be approximated as follows:

$$Da = c_1 \left(\frac{P x^{0.2}}{G^{0.8}} \right) \tag{2.48}$$

where the constant c_1 includes the effects of the blowing parameter, the flame temperature and the gas viscosity. Combining the last two equations it is possible to write:

$$\frac{\dot{r}}{\dot{r}_0} = c_2 \left(\frac{P^{0.5} x^{0.1}}{G^{0.4}} \right) \tag{2.49}$$

Substituting the reference regression rate equation (2.28) and absorbing the blowing number into the constant c_2, it is possible to obtain the expression of the regression rate for the kinetically controlled region:

$$\dot{r} = c_3 P^{0.5} G^{0.4} x^{-0.1} \tag{2.50}$$

Even if this correlation has a qualitative meaning, it underlines that in the region of very high mass fluxes the regression rate is dependent on the pressure and less dependent on the total mass flux.

2.4 REGRESSION RATE BEHAVIOR

It is useful to summarize the last considerations on the regression rate of hybrid rocket motors with the help of figure 2.7, which qualitatively represents the correlation between the regression rate and the total mass flux in a logarithmic plot. Here the basic Marxman correlation appears as a straight line with a slope equal to the exponent n. For intermediate mass fluxes the regression rate is dominated

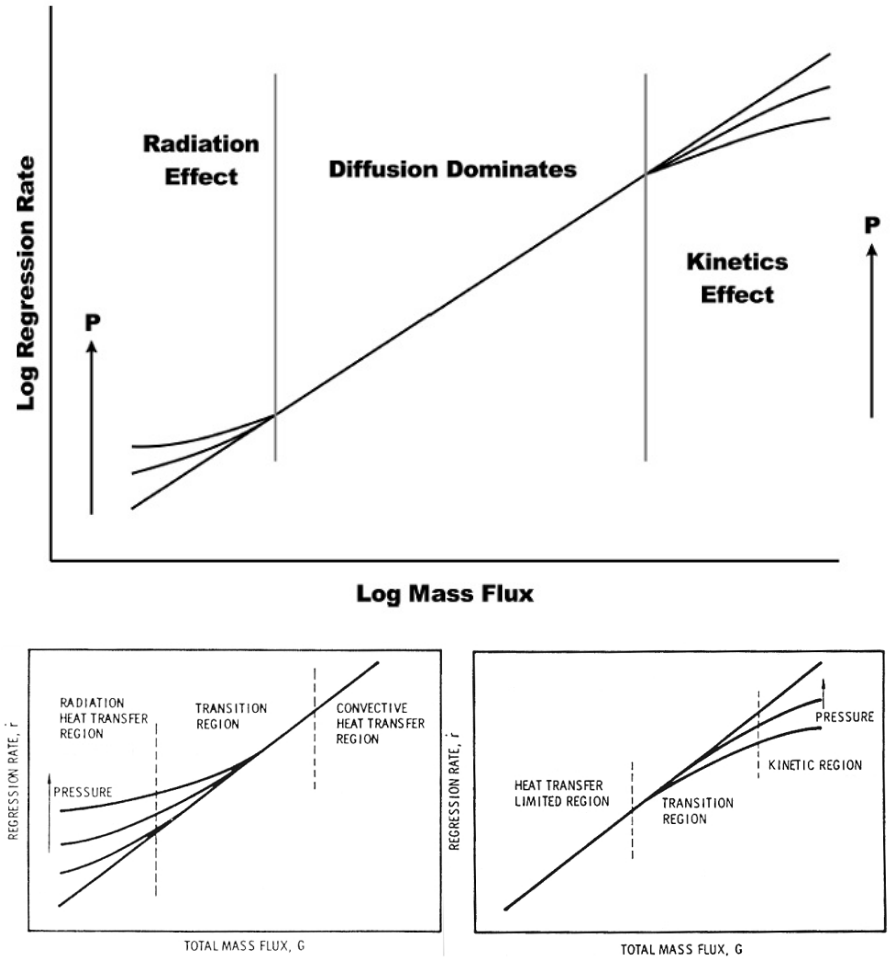

Figure 2.7: Variation of the regression rate with the total mass flux: logarithmic plot (top) and zoom of the pressure dependent regions (bottom)

by the turbulent diffusion and is independent of the radiation or the chemical kinetics. For low mass fluxes the influence of the radiative heat flux increases because the turbulent convection component of the total wall heat flux is small, causing a flattening of the slope of the curve. In this region a lower pressure increases the linear part of the curve further decreasing the regression rate. For high mass fluxes the effect of the chemical kinetics is more important because the residence time of the gases is reduced, causing a decrease of the slope of the curve. In this region a higher pressure increases the linear part of the curve, and consequently also the regression rate.

2.5 MIXTURE RATIO SHIFT

As already anticipated in chapter 1, one of the disadvantages of hybrid rocket motors is the mixture ratio shift that occurs during the burning time. In liquid rockets the oxidizer to fuel ratio can be directly

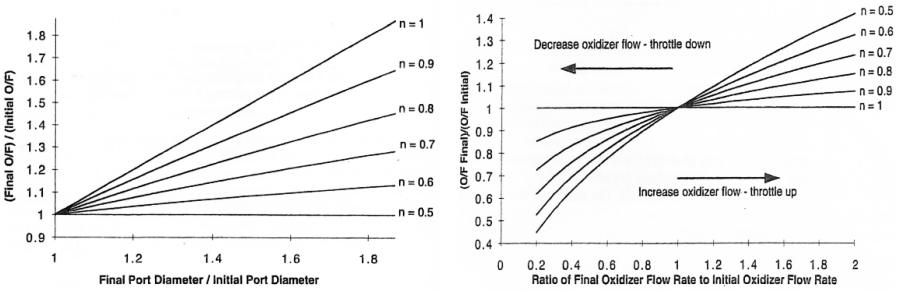

Figure 2.8: Adimensional mixture ratio shift for hybrid motors: with port diameter (left) and with oxidizer mass flux (right)

controlled adjusting the mass flow of the propellants, while in solid rockets the mixture ratio is constant because fuel and oxidizer are pre-mixed in the solid grain matrix. On the other hand, in hybrid rocket motors the mixture ratio shifts during the operation because only the oxidizer mass flow can be directly controlled, whereas the fuel generation is determined by the complex combustion process. Considering a classical cylindrical grain with a circular port, the fuel port area enlarges with time causing an increase of the burning surface but at the same time a decrease of the regression rate. These two effects are generally not balanced and they cause the variation of the mixture ratio with burning time.

Remembering the regression rate correlation for a solid grain with a single circular port:

$$\dot{r} = aG_{ox}^{n}L^{m} \tag{2.51}$$

it is possible to rewrite the definition of the mixture ratio, which is the ratio between the oxidizer and the fuel:

$$\varphi = \frac{\dot{m}_{ox}}{\dot{m}_{f}} = \frac{\dot{m}_{ox}^{1-n}D_{p}^{2n-1}}{a\pi^{1-n}4^{n}\varrho_{f}L^{1+m}} \tag{2.52}$$

Two different situations can be analyzed, namely the variation of the mixture ratio during the burning time for a constant oxidizer mass flow (caused by grain port enlargement) or for a variable oxidizer mass flow (that is motor throttling). The adimensional mixture ratio shift for the two cases is represented in figure 2.8.

The first case occurs when the oxidizer mass flow is kept constant during the combustion. During the burning time the circular port of the solid grain enlarges, increasing the fuel burning area and decreasing the oxidizer mass flux. The fuel mass flow is dependent on both the regression rate and the burning area. Considering that only the port diameter varies with time and that the exponent of this parameter is $2n - 1$, it is possible to divide this situation in three subcases. For $n = 0.5$ there is no mixture ratio shift because the increase of the burning area is perfectly balanced by the reduction of

the regression rate. For $n < 0.5$ the mixture ratio decreases during the burning time because the enlargement of the port area is more relevant than the reduction of the regression rate. For $n > 0.5$ the mixture ratio increases with time because the reduction of the regression rate prevails on the increasing of the burning area, leading to a decrease of the fuel mass flow.

The second case is when the oxidizer mass flow is throttled. The mixture ratio depends on the oxidizer mass flow raised to the power of $1 - n$. For this reason for $n = 1$ there is no mixture ratio shift because this case represents a linear correlation between the oxidizer mass flow and the fuel mass flow. Unfortunately, the mass flux exponent is always $n < 1$ and even the one predicted by Marxman is $n = 0.8$. The fuel mass flow variation is always sub-linear and it causes a mixture ratio shift during the throttling. Since the variation of the fuel mass flow caused by the oxidizer throttling is lower than the ideal case, it is necessary to have a higher throttling ratio to obtain the wanted fuel variation.

3

ANALYTICAL TOOLS FOR SYSTEM DESIGN

Hybrid rocket motors have several potential advantages with respect to other propulsion systems currently used, as discussed in chapter 1. However, they are generally not very flexible concerning the motor configuration, and the packaging of the hybrid propulsion system is strongly related to the sizing of the combustion chamber. Therefore, it is fundamental to understand how the length, the external diameter, the volume loading and the length to diameter ratio vary with the design parameters such as scale, burning time, average mixture ratio, initial oxidizer mass flux and propellant combination. It is already possible to determine these quantities for conventional hybrid rocket motors thanks to the equations available in the literature. However, those equations are not in explicit form with respect to the aforementioned design parameters. Moreover, it is not possible to compute the instantaneous and average characteristic velocities during the burn without a numerical integration over time that interpolates a look-up table obtained from a thermochemical code.

This chapter is intended to help the understanding of hybrid propulsion and its design. To achieve this goal, a set of simple explicit analytical equations to describe hybrid rocket behavior and motor sizing has been derived, in order to have a better sensibility on the trends, possibilities and limits of this promising but tricky kind of propulsion system [11]. The equations refer to the length, the diameter, the volume loading and the length to diameter ratio of the combustion chamber, the performance penalties and the thrust variations incurred with time and throttling and the mission envelope of hybrid rocket motors. The use of explicit analytical tools has a strong beneficial effect, because it clearly shows the fundamental parameters affecting the results and their sometimes not intuitive dependencies.

3.1 MOTOR BEHAVIOR CHARACTERIZATION

Hybrid rocket performance is affected by the fact that the mixture ratio is not controlled and varies with time and throttling [3, 22]. For the sake of clarity, the mixture ratio shift with diameter for a constant oxidizer mass flow is defined as:

$$\frac{\varphi}{\varphi_0} = \left(\frac{D_f}{D_0}\right)^{2n-1} = R^{2n-1} \tag{3.1}$$

If the regression rate exponent is $n = 0.5$ the mixture ratio is constant with time, if it is higher the mixture ratio increases, while the opposite occurs for lower values. This behavior is shown in figure 3.1. The

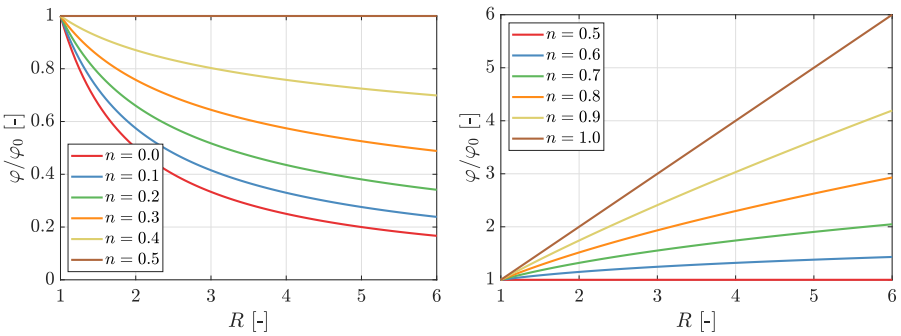

Figure 3.1: Variation of mixture ratio with diameter ratio for $n \leq 0.5$ (left) and $n \geq 0.5$ (right)

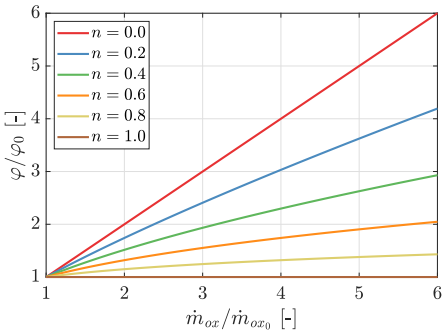

Figure 3.2: Variation of mixture ratio with throttling

mixture ratio shift with throttling of the oxidizer flow is described by the following equation:

$$\frac{\varphi}{\varphi_0} = \left(\frac{\dot{m}_{ox}}{\dot{m}_{ox_0}}\right)^{1-n} \tag{3.2}$$

In this case if $n = 1$ no mixture ratio shift occurs, while for lower values (as in typical hybrids) the fuel mass flow variation is sublinear, as it can be seen in figure 3.2. The consequence of the mixture ratio shift is a variation of the total propellant mass flow, along with the characteristic velocity, specific impulse and chamber pressure. The total mass flow is calculated from the mixture ratio. Chamber pressure and thrust are calculated by the following equations:

$$P_{cc} A_t = \dot{m}_{tot} c^\star \tag{3.3}$$

$$F = \dot{m}_{tot} I_{sp} g_0 \tag{3.4}$$

The calculations require the knowledge of the characteristic velocity and specific impulse. These are generally computed with a look-up table created with a thermochemical code. Even if this is pretty simple to do with modern computers, it is still useful to obtain an explicit analytical expression for the variation of thrust and chamber pressure. A crude zero order approximation is to use the previous equations with constant values of specific impulse and characteristic

velocity, so that thrust and pressure vary only with the total mass flow. A better approximation is presented here based on the work of Koehler and Schmucker [66, 103]. The characteristic velocity is approximated with an explicit function of the mixture ratio only. This is a good approximation as the effect of chamber pressure on the characteristic velocity is much smaller if the pressure is sufficiently high (as a rule of thumb higher than 10 bar). Comparing several propellant combinations, the following expression was found to be suitable:

$$c^\star = \frac{a + b\varphi}{1 + \frac{1}{\varphi}} \tag{3.5}$$

where:

$$\frac{a}{b} = 1 - (\varphi_{opt} + 1)^2 = -\varphi_{opt}(\varphi_{opt} + 2) = -\varphi_{max} \tag{3.6}$$

$$b = -\frac{c^\star_{opt}}{\varphi^2_{opt}} \tag{3.7}$$

$$\varphi_{max} = \varphi^2_{opt} + 2\varphi_{opt} \tag{3.8}$$

$$\frac{\varphi_{max}}{\varphi_{opt}} = \varphi_{opt} + 2 \tag{3.9}$$

Koehler curve has a maximum equal to the optimal characteristic velocity at the optimal mixture ratio and goes to zero for $\varphi = 0$ and $\varphi = \varphi_{max}$. The relative characteristic velocity is dependent only on the relative mixture ratio and the optimal mixture ratio:

$$\varphi_R = \frac{\varphi}{\varphi_{opt}} \tag{3.10}$$

$$\frac{c^\star}{c^\star_{opt}} = \varphi_R \frac{(2 + \varphi_{opt} - \varphi_R)}{1 + \varphi_{opt}\varphi_R} \tag{3.11}$$

As it can be seen in figure 3.3, φ_R determines the position on the curve while φ_{opt} defines the shape of the curve. It is worth noting that Koehler model predicts a flatter curve as φ_{opt} is increased. This is in general confirmed experimentally and shows that propellants with higher optimal mixture ratio are less sensitive to the mixture ratio shift. Here Koehler expression has been validated with three propellant combinations: LOX-HTPB, 90 % HTP-HTPB and N_2O-HTPB. In figures 3.4, 3.5 and 3.6 the error obtained assuming $c^\star = c^\star_{opt}$ and using Koehler expression is shown. The zero order hypothesis provides always overestimated results, except at the optimum point where the error is zero. Koehler expression is slightly optimistic around the optimum point and then crosses the real curve at a certain distance from the optimum point. After that and in both directions, the error changes sign and Koehler becomes pessimistic. In the range $0.5 \leq \varphi_R \leq 2$, the error of Koehler expression is on the order of few percent and is particularly accurate for N_2O and 90 % HTP. One secondary possible

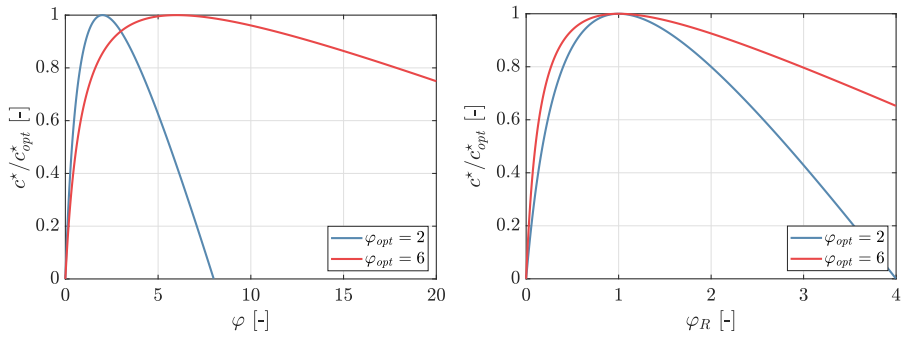

Figure 3.3: Characteristic velocity ratio as a function of mixture ratio (left) and adimensional mixture ratio (right)

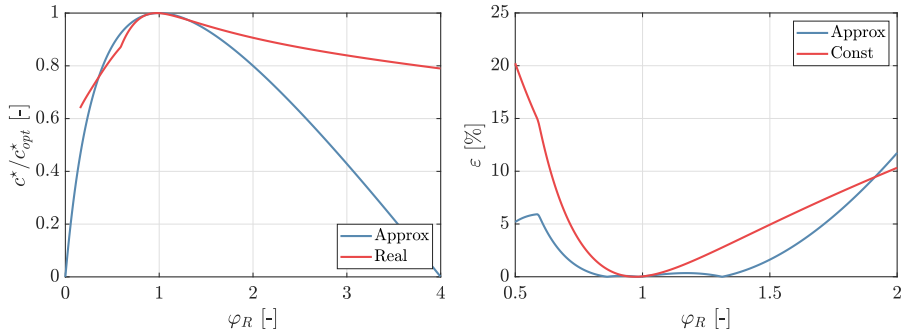

Figure 3.4: LOX validation

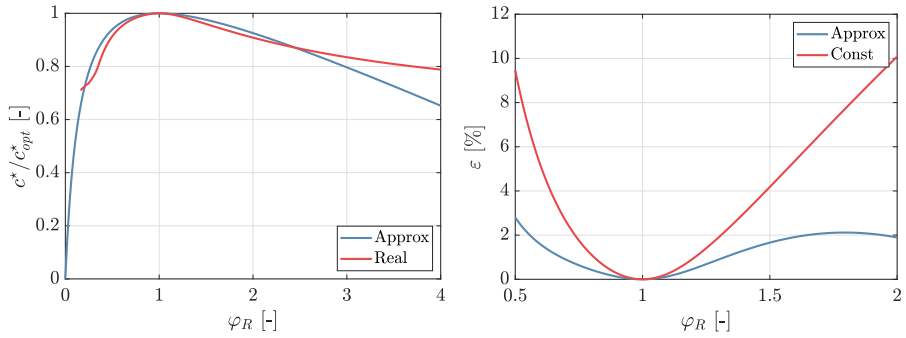

Figure 3.5: HTP validation

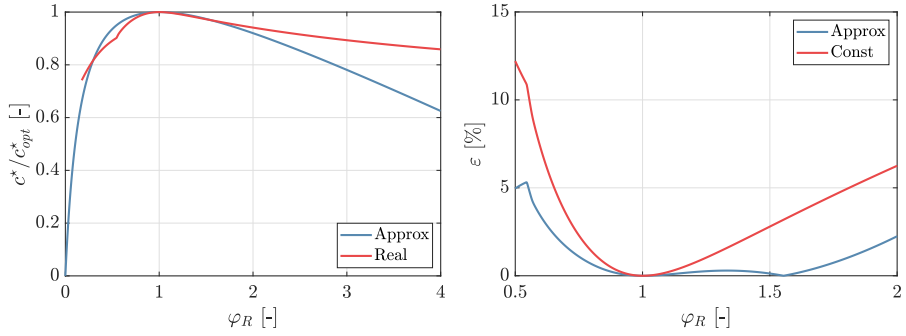

Figure 3.6: N_2O validation

advantage of these relations for the characteristic velocity is that they can be used in relatively complex preliminary optimization problems combining many aspects, like sizing or trajectory, in order to save computational time at each iteration.

Thanks to Koehler expression, it is now possible to estimate the penalty incurred with throttling from the optimal point using equations (3.2), (3.10) and (3.11) with $\varphi_0 = \varphi_{opt}$, as shown in figures 3.7 and 3.8. Moreover, in Koehler model chamber pressure becomes:

$$P_{cc} A_t = \dot{m}_{ox}(a + b\varphi) \tag{3.12}$$

And consequently pressure variations, which are represented in figure 3.9, can be calculated neglecting nozzle erosion as:

$$\varphi_{R_0} = \frac{\varphi_0}{\varphi_{opt}} \tag{3.13}$$

$$\frac{P_{cc}}{P_{cc_0}} \frac{\dot{m}_{ox_0}}{\dot{m}_{ox}} = \frac{\varphi_{opt} + 2 - \varphi_R}{\varphi_{opt} + 2 - \varphi_{R_0}} \tag{3.14}$$

Again, φ_R determines the actual position on the curve, φ_{R_0} determines the initial position on the curve, while φ_{opt} defines the shape of the curve. The same results can be obtained for the thrust using the equivalent curve of the specific impulse instead of the characteristic velocity. It is worth noting that the use of a non-constant characteristic velocity has a significant impact on chamber pressure behavior. When the motor is throttled up from the optimum mixture ratio (or higher mixture ratios), the pressure increase is lower than the throttling ratio (because the fuel mass flow is not increased as well), and this effect is slightly amplified by the drop of characteristic velocity. When the motor is throttled down from the optimum mixture ratio (or lower mixture ratios), the pressure decrease is lower than the throttling ratio (because the fuel mass flow is not decreased as well), and in this case the characteristic velocity drop acts on the opposite direction, slightly compensating the phenomenon. The opposite behavior occurs for throttling up from lower than optimal mixture ratios and throttling down from higher than optimal mixture ratios, unless the final operational point crosses the optimum point. For moderate throttling ratios the characteristic velocity penalty is limited, in fact for $n = 0.5$ and $\varphi_{opt} = 2$ and a throttling ratio of 0.5 the penalty is around 3.5 %. For $n = 0.5$ and $\varphi_{opt} = 7$ and a throttling ratio of 0.5 the penalty is 1.5 %. Again, a propellant with a higher optimal mixture ratio provides better results both in term of characteristic velocity penalty and pressure "precision" (pressure ratio similar to oxidizer mass flow ratio).

It is important to note that this penalty has to be multiplied by the relative total impulse spent at the non-optimal mixture ratio, further decreasing the penalty. Considering also that throttling down from the optimal point is more "precise" (as just shown), it is recommended to calibrate the maximum mass flow rate at the optimal mixture ratio.

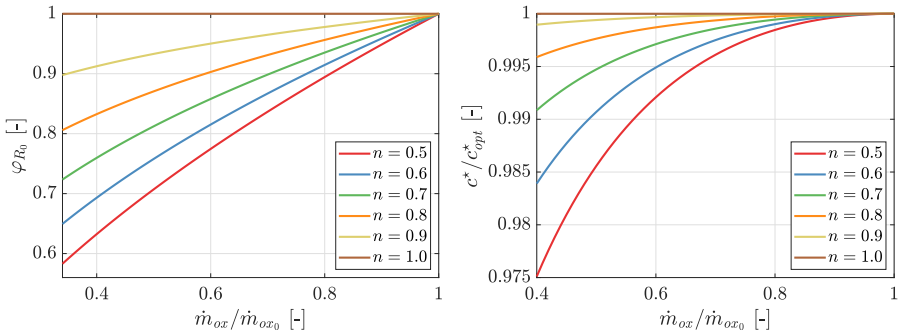

Figure 3.7: Penalty incurred with throttling down from optimal mixture ratio, where $\varphi_{opt} = 7$

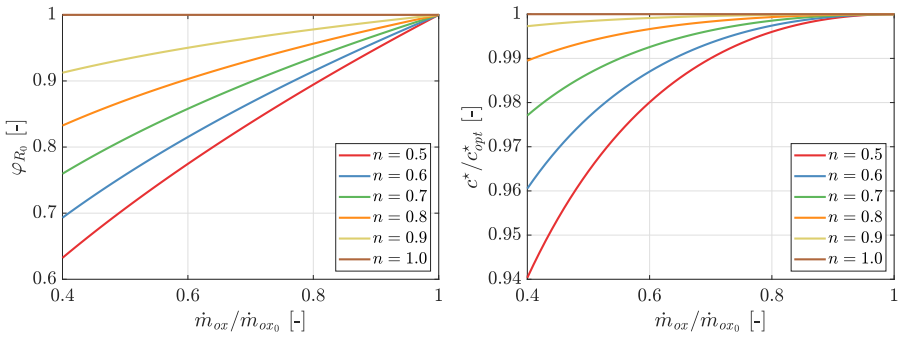

Figure 3.8: Penalty incurred with throttling down from optimal mixture ratio, where $\varphi_{opt} = 2$

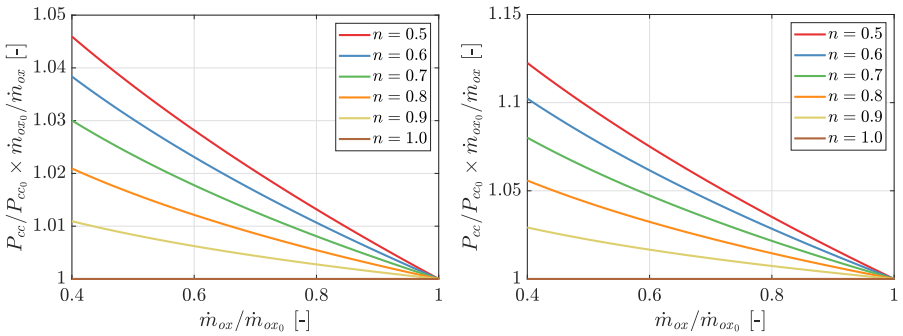

Figure 3.9: Pressure ratio multiplied by oxidizer mass flow ratio in case of throttling down from optimal mixture ratio, where $\varphi_{opt} = 7$ (left) and $\varphi_{opt} = 2$ (right)

In case the relative total impulse spent at partial level is significant (much longer time is spent there), the initial mixture ratio should be selected slightly above the optimum point (for throttling down, the opposite for throttling up) to minimize the whole losses. The equations presented in this chapter can be easily used to determine the best initial point.

Regarding the variation of ballistic parameters with time, first of all the diameter ratio can be computed from:

$$R^{2n+1} = (4n+2)\frac{aG_0^n t_b}{D_0} + 1 \tag{3.15}$$

Consequently, equation (3.14) becomes:

$$\frac{P_{cc}}{P_{cc_0}} = \frac{\varphi_{opt} + 2 - \varphi_{R_0}\left(R^{2n-1}\right)}{\varphi_{opt} + 2 - \varphi_{R_0}} \tag{3.16}$$

Again, it is worth noting that the use of a non-constant characteristic velocity has a strong impact on chamber pressure behavior. In fact, the highest is the initial mixture ratio the lowest is the total mass flow variation with time. However, at higher than optimal mixture ratios the characteristic velocity decreases with the mixture ratio, so the effect of mass flow variation is magnified on the pressure. On the contrary, operating at lower than optimal mixture ratios the mass flow variation increases but the characteristic velocity variation has the opposite direction, so a compensation occurs. At the end, the pressure variation predicted by the model is lower at lower than optimal mixture ratios. This result was already shown in [10]. In any case an increase of the optimal mixture ratio decreases the pressure drop, both because the characteristic velocity curve is flatter, and because the mass flow variation is lower. Moreover, it is possible to determine the average mixture ratio from the following equation:

$$\frac{\varphi_{avg}}{\varphi_0} = \frac{R^{2n+1} - 1}{(R^2 - 1)(n + 0.5)} \tag{3.17}$$

that is shown in figure 3.10. It is important to note that the average mixture ratio is the total oxidizer mass divided by the total fuel mass and not the time average of the instantaneous mixture ratio. Finally, it is possible to determine the average chamber pressure and characteristic velocity with the following expressions:

$$\frac{P_{cc_{avg}}}{P_{cc_0}} = 1 + \frac{1}{const}\left(\frac{2n+1}{4n}\frac{R^{4n} - 1}{R^{2n+1} - 1} - 1\right) \tag{3.18}$$

$$const = 1 + \frac{a}{b\varphi_0} = 1 + f\left(\varphi_0, \varphi_{opt}\right) = 1 - \frac{\varphi_{max}}{\varphi_0} \tag{3.19}$$

$$P_{cc_{avg}} A_t = \left(\dot{m}c^\star\right)_{avg} = \dot{m}_{avg} c^\star_{avg} \tag{3.20}$$

$$c^\star_{avg} = \frac{1}{t_b}\int_0^{t_b} \frac{\dot{m}}{\dot{m}_{avg}} c^\star dt \tag{3.21}$$

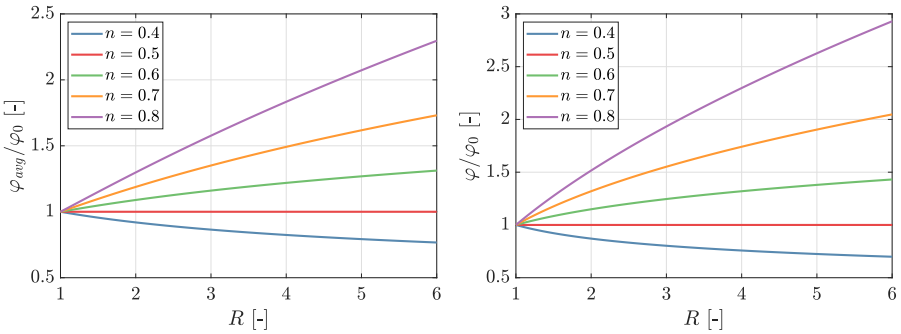

Figure 3.10: Mixture ratio shift with time: average ratio (left) and final ratio (right)

$$c^\star_{avg} = \frac{P_{cc_{avg}}}{P_{cc_0}} \frac{a + b\varphi_0}{1 + \frac{1}{\varphi_{avg}}} \tag{3.22}$$

$$\frac{c^\star_{avg}}{c^\star_{opt}} = \frac{P_{cc_{avg}}}{P_{cc_0}} \frac{\varphi_{opt} + 2 - \varphi_{R_0}}{\varphi_{opt} + 1} \frac{1 + \frac{1}{\varphi_{opt}}}{1 + \frac{1}{\varphi_{avg}}} = f\left(R, n, \varphi_0, \varphi_{opt}\right) \tag{3.23}$$

It is important to underline that the average characteristic velocity is not the time average of the instantaneous characteristic velocity. The variation of characteristic velocity with time can be limited selecting the initial mixture ratio in order to cross the optimal mixture ratio during operation.

It is interesting to plot the results of the characteristic velocity penalty and the other ballistic parameters when the average mixture ratio is selected as the optimal one:

$$\varphi_{avg} = \varphi_{opt} \tag{3.24}$$

$$\varphi_0 = f\left(R, n, \varphi_{opt}\right) \tag{3.25}$$

$$\frac{c^\star_{avg}}{c^\star_{opt}} = \frac{P_{cc_{avg}}}{P_{cc_0}} \frac{\varphi_{opt} + 2 - \varphi_{R_0}}{\varphi_{opt} + 1} = f\left(R, n, \varphi_{opt}\right) \tag{3.26}$$

This is not exactly the best choice for average characteristic velocity maximization but is very near to it. For typical R and n values characteristic velocity penalty can be limited to much less than 1 %. Average pressure can be generally kept within 10 % of the initial one. Again, a propellant combination with a higher optimal mixture ratio has a lower characteristic velocity loss and a lower pressure variation. These results are shown in figure 3.11, 3.12 and 3.13.

3.2 MISSION ENVELOPE DEFINITION

In this section some simple equations to define the possible mission envelope of hybrid rocket motors with single cylindrical port fuel

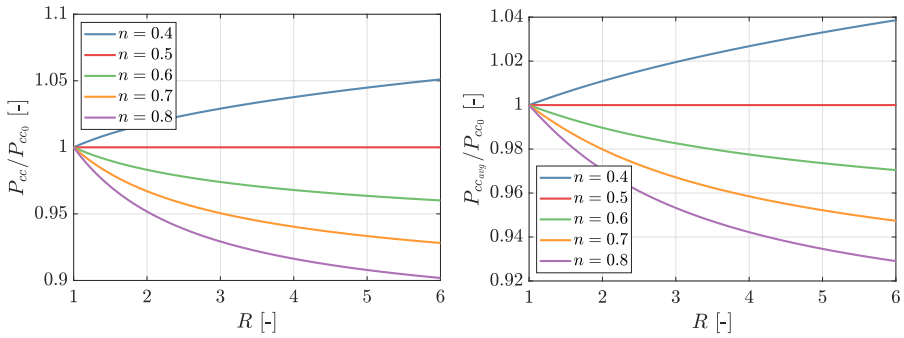

Figure 3.11: Mixture ratio shift with time: final pressure (left) and average pressure (right), where $\varphi_{opt} = 7$

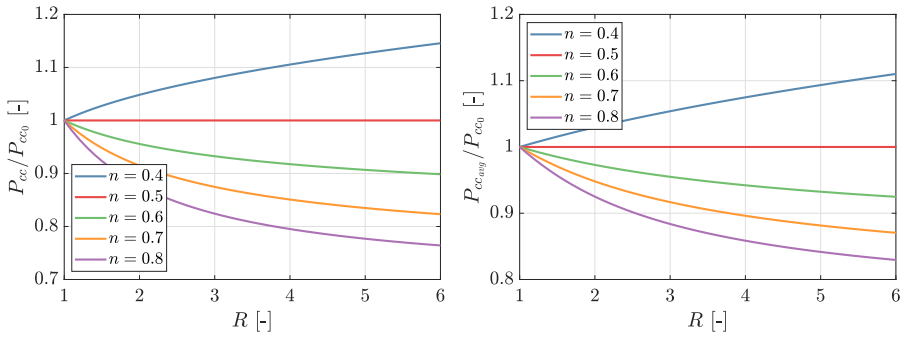

Figure 3.12: Mixture ratio shift with time: final pressure (left) and average pressure (right), where $\varphi_{opt} = 2$

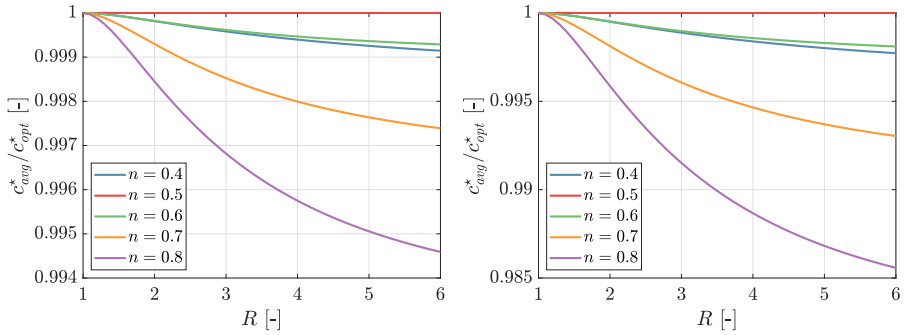

Figure 3.13: Mixture ratio shift with time: average characteristic velocity, where $\varphi_{opt} = 7$ (left) and $\varphi_{opt} = 2$ (right)

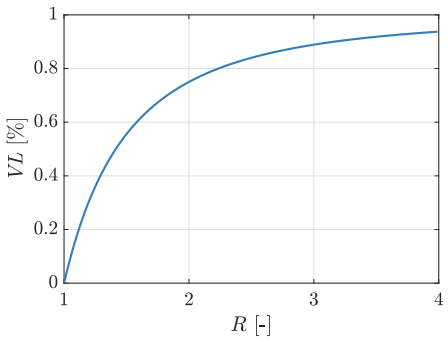

Figure 3.14: Variation of port volume loading with diameter ratio

grains are derived. Considering a constant oxidizer mass flow, it is possible to determine the final port diameter:

$$G_0 = \frac{4\dot{m}_{ox}}{\pi D_0^2} \tag{3.27}$$

$$D_f = \left[a(4n+2)t_b \left(G_0 D_0^2\right)^n + D_0^{2n+1} \right]^{\frac{1}{2n+1}} \tag{3.28}$$

With some manipulations, the following equation can be obtained:

$$\frac{aG_0^n t_b}{D_0} = \frac{R^{2n+1}-1}{4n+2} \tag{3.29}$$

On the left there is a quantity that will be called adimensional reference web thickness. It is adimensional because it is divided by the initial port diameter, and it is called reference because it is not the actual motor web thickness but it is the web thickness calculated as if the regression rate was kept constant and equal to the initial one. The real web thickness is always lower than the reference one because of the regression rate decay with time. The equation above shows that the adimensional reference web thickness is dependent only on the diameter ratio and the regression rate exponent n.

As it can be seen in figure 3.14, the diameter ratio is related to the grain volume loading by the following equation:

$$VL = 1 - \frac{1}{R^2} \tag{3.30}$$

The volume loading increases asymptotically to 100 % with the diameter ratio. A minimum diameter ratio between 2 to 3 is generally recommended in order to have a good volume loading. Much higher diameter ratios do not provide major benefits. It is possible now to plot equation (3.29), relating motor size to burning time for a fixed propellant combination at different volume loadings or for a fixed volume loading with different propellant combinations. The selected values are $a = 0.11$, $n = 0.65$ and $G_0 = 800\,\mathrm{kg/m^2}$ (for a regression rate in mm/s) that are typical values of the LOX and paraffin wax combination. Moreover, in order to represent a typical non-liquefying

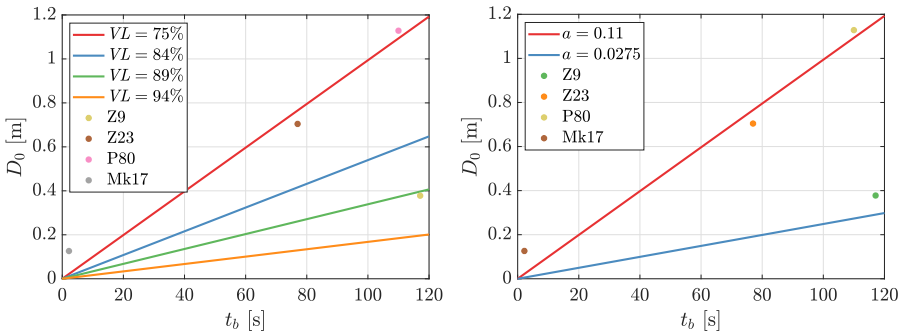

Figure 3.15: Relation between motor size and burning time: parametric with volume loading for $a = 0.11$ (left) or with regression rate for $VL = 75\,\%$ (right)

plastic fuel also a coefficient $a = 0.0275$ has been considered. The results are shown in figure 3.15.

Equation (3.29) shows a linear relation of burning time with size in order to keep a constant geometry and consequently a constant volume loading. As the size of the motor is increased, or the burning time is shortened, the volume loading decreases. This is a well-known problem of conventional hybrid rockets. It is worth noting that the size of the motor is proportional to the square of the thrust. On figure 3.15 some reference solid rocket motors are also plotted. The diameter of the solid rocket points has been calculated as the equivalent initial diameter of a hybrid rocket that has the same propellant mass and burning time. One solid rocket has a very short burning time and is the boost motor of the air-to-air missile AIM-9 Sidewinder, the other motors are the three solid stages of the small launcher Vega. Considering figure 3.15 on the right, it is possible to see that all the solids rocket points are above the lower curve. This means that a classical hybrid rocket cannot match the same thrust-burning time of the solids and provide a good volume loading. In order to overcome the low regression rate issue, one solution is to shift from a single cylindrical port to a multiport grain or to other complex geometries. However, all these solutions suffer from serious problems of residuals and increased mixture ratio shift. The use of paraffin wax, which has a higher regression rate, gives the possibilities to design motors with bigger diameters and/or with shorter burning time. With paraffin wax the Vega launcher motors become potentially feasible, particularly the smaller Zefiro 9. However, the missile booster is still largely out of the possibility. Moreover, increasing the burning time of Zefiro 23 to the same level of the other two will improve the volume loading. This shows that, when using hybrid rockets (except for small scales), the optimum design point tends to shift to a longer burning time.

To be accurate, the regression rate coefficient a is generally not constant with scale. As already presented in chapter 2, according to Marxmann theory it should slowly decrease with the scale, but

generally the dependence is very low for plastic fuels and is almost negligible for paraffin wax, at least on the scale range tested up to now. This means that increasing both the size and the burning time of the hybrid motor, the geometry is not exactly kept constant, but the larger one will have a slightly smaller volume loading. This slightly decrease of the regression rate with scale has a second order effect (that has been neglected here) which amplifies the aforementioned problem. From equation (3.29) it is possible to see that increasing the initial oxidizer flux will improve the volume loading. However, for a specific propellant combination and injection scheme, there is an upper limit of oxidizer mass flux due to flooding or flame blow-off. The port Mach number can limit also the maximum oxidizer mass flux, particularly at low chamber pressures.

After having discussed the lower limit of the adimensional reference web thickness, it is now possible to focus on the upper limit. This limit is often overlooked in hybrid rocket propulsion but is still important. It has been already shown that increasing the value of the diameter ratio above 4 does not provide much benefit on the volume loading. However, a high value of the diameter ratio could be problematic because the motor should provide good performance with a large change in geometry. The injection should guarantee high stability and efficiency and regression uniformity with a large change of the port size. This could be not easy and could provide an upper limit on the diameter ratio. Moreover, the final oxidizer mass flux is related with the initial one by the following equation:

$$\frac{G_0}{G_f} = R^2 \tag{3.31}$$

As already said the initial oxidizer mass flux is limited. The final oxidizer mass flux could be also limited by the too low regression rate that could cause consequent issues like chuffing and high thermal penetration. All these concerns could provide an upper limit on the value of diameter ratio. Some configurations are much more tolerant to higher values of diameter ratio with respect to others. For example, HTP decomposed with a catalyst provides a hot gas injection that tends to guarantee proper operation on a wide range of fluxes [9, 95]. The situation can be worst in the case of liquid injection of LOX [40, 61, 106], RFNA [42] or subcooled N_2O. Two-phase N_2O represents an intermediate situation [21, 69].

Plotting equation (3.29) for the maximum and minimum allowed values of diameter ratio, it is possible to obtain figure 3.16. The minimum diameter ratio has been selected as 2 and the maximum as 6 (as previously highlighted, this number can be different depending on the specific case). The high regression rate refers to $a = 0.11$ while the low regression rate to $a = 0.0275$. Hybrid rocket motors are suitable for missions where size and burning time are inside the region defined by the two straight lines. This region shifts to higher

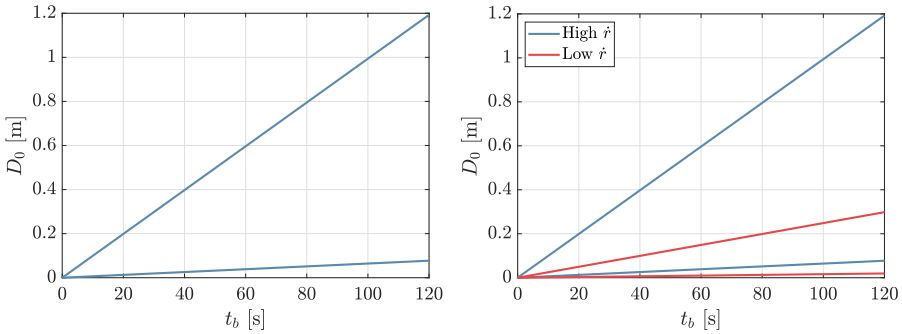

Figure 3.16: Mission envelope for single port hybrid rocket motors, where the area between two curves of the same color represents suitable combinations of burning time and initial diameter

sizes and lower burning times for high regressing fuels, while it shifts to longer burning times and lower sizes for low regressing fuels. Regression rate can be tailored for the particular application selecting the most appropriate fuel. However, hybrid rockets are not suitable for short burning times and high thrusts but also for too long burning times and low thrusts. In this second case the technological problems related with nozzle cooling should be taken into consideration. Hybrid rockets in general use an ablative cooling partially borrowed from solid rockets technology. If the burning time is too long, particularly if high performance is required, other techniques more similar to liquid rockets should be used, partially reducing the simplicity advantage of hybrid rockets compared to liquid rockets. It is worth noting that the problem of nozzle erosion and cooling is more significant as throat diameter decreases, so even in this case higher thrusts mean longer possible burns.

It is also important to highlight that the size of a liquid rocket is proportional to the square root of the required thrust. For high volume loadings the size of the hybrid rocket combustion chamber is proportional to the fuel mass, therefore it is related to the total impulse. A small thrust means a small liquid rocket, while a small thrust coupled with a long burning time (for a high total impulse) means a big hybrid rocket. Moreover, a change in the burning time for the same thrust (for a different total impulse) can be accommodated by the liquid rocket changing the propellant mass and so the tanks size. In case of the hybrid rocket, such a change should imply a redesign of the motor.

Concerning the effect of the initial oxidizer mass flux on the lower boundary of the size-burning time region, two situations can occur. If the limit is on the diameter ratio itself (without flux limits), lowering the initial oxidizer mass flux will widen the region of suitability. If the limit is on the final oxidizer mass flux, starting at higher oxidizer mass fluxes will widen the region, because higher oxidizer mass flux ratios mean higher diameter ratio values, defined by equation (3.31).

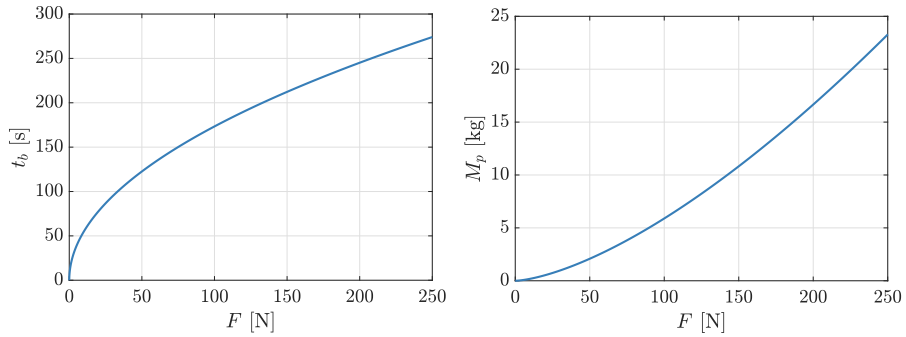

Figure 3.17: Burning time (left) and propellant mass (right) limits for single port hybrid rocket motors

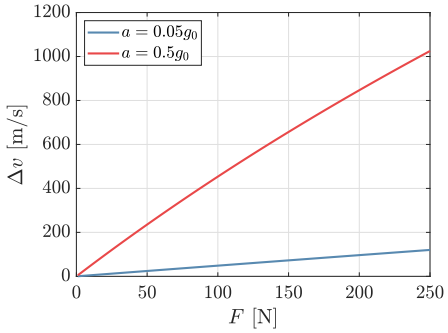

Figure 3.18: Variation of maximum velocity increment with thrust for two different accelerations

Focusing the attention on space engines, with equation (3.29) it is possible to determine the maximum burning time (based on the upper diameter ratio limit) for a certain size. The thrust is proportional to the square of the diameter, so the burning time becomes proportional to the square root of the thrust. The propellant mass is proportional to the thrust multiplied by the burning time, which is proportional to the square root of the thrust:

$$M_p \propto F t_b \propto F^{\frac{3}{2}} \tag{3.32}$$

These results are plotted in figure 3.17 for a specific impulse of 300 s and a mixture ratio of 7, with $a = 0.0275$ and $n = 0.5$, $G_0 = 500\,\mathrm{kg/m^2 s}$, $G_f = 10\,\mathrm{kg/m^2 s}$. Once the thrust and the propellant mass are known it is possible to calculate the velocity increment of the satellite. The total empty mass of the satellite can be calculated from the motor thrust if there is a limit on the maximum allowable acceleration. In figure 3.18 the velocity increment for two different maximum accelerations is plotted. It is possible to see that the maximum velocity increment increases with thrust. Small hybrid rockets are limited to short burning time and consequently they provide lower velocity increments. For the same acceleration limits, larger satellites propelled by hybrid rockets can achieve higher velocity increments than smaller satellites (because the satellite mass scale linearly with

thrust while the propellant mass scale more than linearly). For a fixed satellite size, if the allowable maximum acceleration is low the hybrid rcoket can provide only a limited maximum velocity increment. If the required velocity increment is moderate hybrid rockets give their best because they can fully exploit their advantages compared to liquid rockets. Moreover, at moderate velocity increments, the system mass has a lower sensitivity to inert mass and specific impulse and this makes the design even easier. For high velocity increments, the hybrid rocket has to increase its thrust, while the liquid rocket simply increase its burning time as necessary. Increasing the thrust, the hybrid rocket could reach the acceleration limit. Even in the case where the acceleration level does not represent an issue, the relative high thrust hybrid rocket has to compete with a low thrust liquid rocket that probably would have a lower inert mass and size. The mass and size of the propulsion system are more critical for high velocity increments.

3.3 COMBUSTION CHAMBER SIZING

In this section the set of explicit equations that describe hybrid motor behavior is completed. In particular, the size and shape of the fuel grain and its dependency on motor and propellant parameters is determined. The typical equations found in the literature do not show explicitly this type of relations because they keep some kind of hidden dependencies [3, 22]. This means that once a parameter is changed, another one is also influenced. Alternatively, as shown in the following mathematical treatment, the equations contain some instantaneous parameters that are not known in advance.

As a starting point, it is possible to rearrange the definition of mixture ratio to obtain the following equation:

$$L = \frac{\dot{m}_{ox}^{0.5}}{2\pi^{0.5} a \varrho_f \varphi G_{ox}^{n-0.5}} \tag{3.33}$$

This equation contains instantaneous parameters like mixture ratio, oxidizer mass flow and oxidizer mass flux. For simplicity, the oxidizer mass flow is considered as constant. For $n = 0.5$ the equation simplifies to:

$$L = \frac{\dot{m}_{ox}^{0.5}}{2\pi^{0.5} a \varrho_f \varphi} \tag{3.34}$$

In this case, the mixture ratio is a fixed quantity, therefore the length of the fuel grain is inversely proportional to the fuel density, the regression rate parameter a and the mixture ratio, while is directly proportional to the square root of the oxidizer mass flow. This is consistent with the fact that the thrust is proportional to the square of the size of the motor. For different values of n, equation (3.33) can

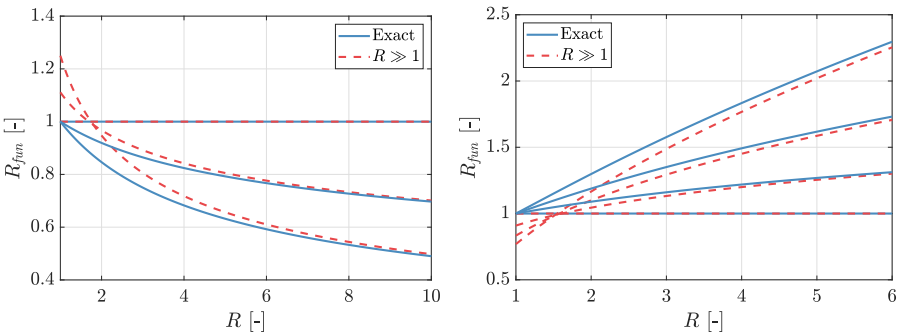

Figure 3.19: Values of R_{fun} for $n \leq 0.5$ (left) and $n \geq 0.5$ (right)

be written in terms of the initial values of mixture ratio and oxidizer mass flux:

$$L = \frac{\dot{m}_{ox}^{0.5}}{2\pi^{0.5} a \varrho_f \varphi_0 G_0^{n-0.5}} \tag{3.35}$$

The initial mixture ratio is not a design parameter because it is not known in advance. The next step is to relate the initial mixture ratio to the average one, which is the real design parameter:

$$\begin{aligned} L &= \frac{\dot{m}_{ox}^{0.5}}{2\pi^{0.5} a \varrho_f \varphi_{avg} G_0^{n-0.5}} \frac{R^{2n+1}-1}{(R^2-1)(n+0.5)} \\ &= \frac{\dot{m}_{ox}^{0.5}}{2\pi^{0.5} a \varrho_f \varphi_{avg} G_0^{n-0.5}} R_{fun} \end{aligned} \tag{3.36}$$

This expression is exact but does not show the real dependencies because every time a parameter is changed the diameter ratio would change as well.

In order to better understand hybrid rocket behavior, the two limit cases are considered, that is $R \to 1$ and $R \to \infty$. For $R \to 1$ the second term of equation (3.36) disappears:

$$\lim_{R \to 1} \frac{R^{2n+1}-1}{(R^2-1)(n+0.5)} = \lim_{R \to 1} R_{fun} = 1 \tag{3.37}$$

While for $R \to \infty$ the second term of equation (3.36) becomes:

$$\lim_{R \to \infty} \frac{R^{2n+1}-1}{(R^2-1)(n+0.5)} = \lim_{R \to \infty} R_{fun} = \frac{R^{2n-1}}{n+0.5} \tag{3.38}$$

In figure 3.19, 3.20 and 3.21 the second term of equation (3.36) and the comparison with the two limit cases are plotted.

It is possible to determine the value of diameter ratio where equation (3.38) is equal to equation (3.37):

$$R_{int} = (n+0.5)^{\frac{1}{2n-1}} \tag{3.39}$$

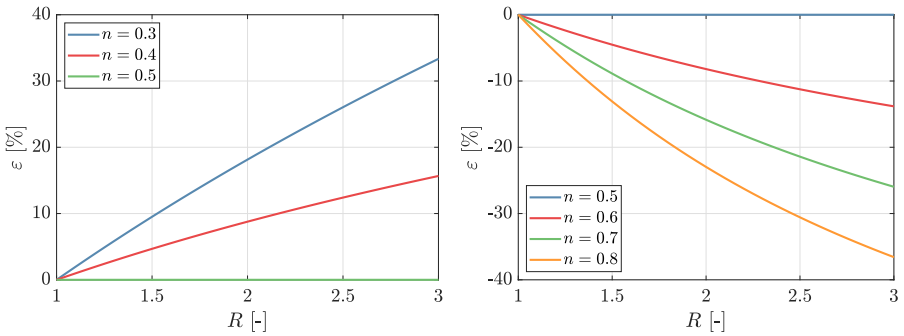

Figure 3.20: Error committed replacing R_{fun} with 1 for $n \leq 0.5$ (left) and $n \geq 0.5$ (right)

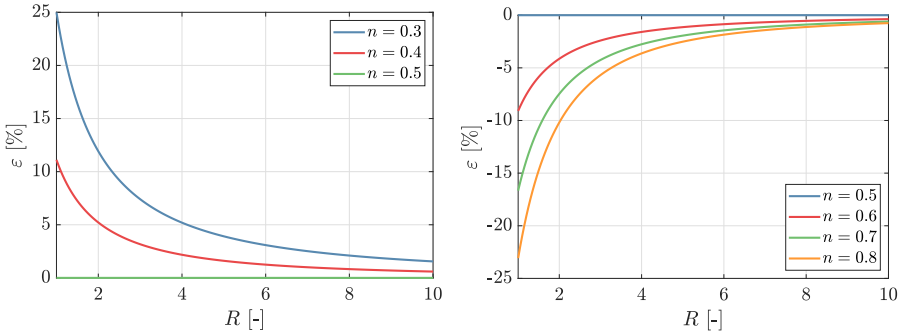

Figure 3.21: Error committed replacing R_{fun} with the asymptotic approximation for $n \leq 0.5$ (left) and $n \geq 0.5$ (right)

In figure 3.22 and 3.23 the R_{int} equation and the error committed using the best approximation in each region are plotted. For $R < R_{int}$ equation (3.37) gives the smallest error, while for $R > R_{int}$ equation (3.38) gives the smallest error. For $n = 0$ equation (3.39) gives $R_{int} = 2$, and the result decreases for $n > 0$. For $R = R_{int}$ the error of the two equations is the same because the curves cross each other. As expected, the error of equation (3.37) is zero for $R = 1$ and increases rapidly and in a slight sublinear fashion. On the opposite, the error of equation (3.38) is high for $R = 1$ and decreases rapidly and asymptotically to zero as the value of the diameter ratio increases. The error is always negative for $n > 0.5$ and always positive for $n < 0.5$. Moreover, the error is always zero for $n = 0.5$ and increases as n departs from this value (both above and below). It is possible to combine the two equations using the best approximation in its preferred range. In this way, the maximum error occurs at $R = R_{int}$.

Considering that $R_{int} < 2$ and remembering the discussion about volume loading, it is worth noting that the approximation for $R = 1$ has a more academic than practical value. However, it is still important to keep it because in this way it is possible to know that the real dependency of the fuel length on motor parameters will be bounded by the ones of the two approximations. On the opposite, the asymptotic

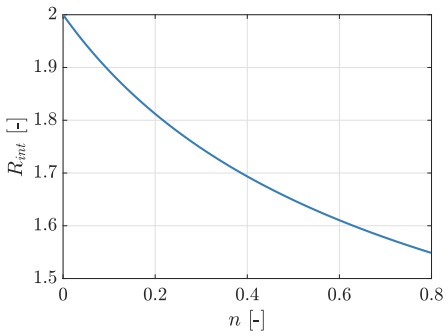

Figure 3.22: Variation of R_{int} with regression rate exponent n

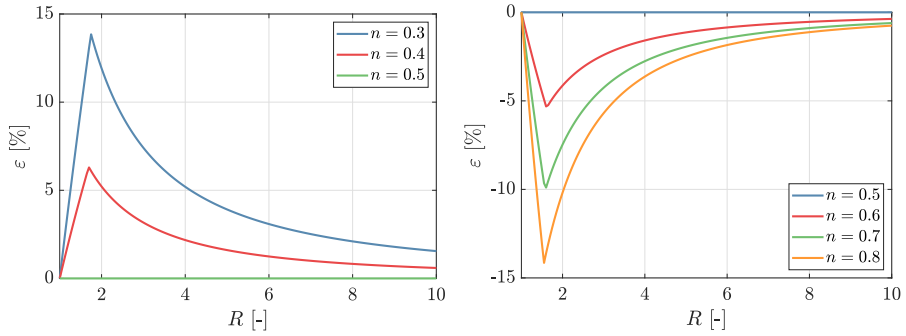

Figure 3.23: Error committed replacing R_{fun} with the best approximation in each region for $n \leq 0.5$ (left) and $n \geq 0.5$ (right)

approximation has a significant practical value, because for typical values of n it has an error of 10 % or lower for $R = 2$, decreasing further for higher diameter ratio values. It is now possible to derive the length, the diameter and thre length to diameter ratio with respect to motor parameters in explicit form for the two limit cases.

If $R = 1$ the initial diameter is equal to the final one:

$$D_f = D_0 \tag{3.40}$$

$$D_f = \frac{2\dot{m}_{ox}^{0.5}}{\pi^{0.5} G_0^{0.5}} = \frac{2M_{ox}^{0.5}}{\pi^{0.5} G_0^{0.5} t_b^{0.5}} = \frac{2M_p^{0.5} \varphi_{avg}^{0.5}}{\pi^{0.5} G_0^{0.5} t_b^{0.5} \left(\varphi_{avg} + 1\right)^{0.5}} \tag{3.41}$$

The length becomes:

$$\begin{aligned} L &= \frac{\dot{m}_{ox}^{0.5}}{2\pi^{0.5} a \varrho_f \varphi_{avg} G_0^{n-0.5}} = \frac{M_{ox}^{0.5}}{2\pi^{0.5} a \varrho_f \varphi_{avg} G_0^{n-0.5} t_b^{0.5}} \\ &= \frac{M_p^{0.5}}{2\pi^{0.5} a \varrho_f \varphi_{avg}^{0.5} \left(\varphi_{avg} + 1\right)^{0.5} G_0^{n-0.5} t_b^{0.5}} \end{aligned} \tag{3.42}$$

And the length to diameter ratio of the fuel grain is:

$$\frac{L}{D_f} = \frac{G_0^{1-n}}{4 a \varrho_f \varphi_{avg}} \tag{3.43}$$

For $R \to \infty$ it is possible to neglect the initial diameter in equation (3.28) and so the final diameter is:

$$\begin{aligned} D_f &= \left[a(4n+2) t_b^{1-n} \left(\frac{4M_{ox}}{\pi} \right)^n \right]^{\frac{1}{2n+1}} \\ &= \left\{ a(4n+2) t_b^{1-n} \left[\frac{4M_p \varphi_{avg}}{\pi(\varphi_{avg}+1)} \right]^n \right\}^{\frac{1}{2n+1}} \end{aligned} \tag{3.44}$$

The length becomes:

$$\begin{aligned} L &= \frac{M_{ox}^{\frac{1}{2n+1}} t_b^{\frac{2n-1}{2n+1}}}{4^{\frac{1}{2n+1}} \pi^{\frac{1}{2n+1}} a^{\frac{2}{2n+1}} \varrho_f \varphi_{avg} (n+0.5)^{\frac{2}{2n+1}}} \\ &= \frac{M_p^{\frac{1}{2n+1}} t_b^{\frac{2n-1}{2n+1}}}{4^{\frac{1}{2n+1}} \pi^{\frac{1}{2n+1}} a^{\frac{2}{2n+1}} \varrho_f \varphi_{avg}^{\frac{2n}{2n+1}} (\varphi_{avg}+1)^{\frac{1}{2n+1}} (n+0.5)^{\frac{2}{2n+1}}} \end{aligned} \tag{3.45}$$

And the length to diameter ratio of the fuel grain is:

$$\begin{aligned} \frac{L}{D_f} &= \frac{M_{ox}^{\frac{1-n}{2n+1}}}{4^{\frac{n+2}{2n+1}} \pi^{\frac{1-n}{2n+1}} a^{\frac{3}{2n+1}} \varrho_f \varphi_{avg} (n+0.5)^{\frac{3}{2n+1}} t_b^{\frac{3(1-n)}{2n+1}}} \\ &= \frac{M_p^{\frac{1-n}{2n+1}}}{4^{\frac{n+2}{2n+1}} \pi^{\frac{1-n}{2n+1}} a^{\frac{3}{2n+1}} \varrho_f \varphi_{avg}^{\frac{3n}{2n+1}} (\varphi_{avg}+1)^{\frac{1-n}{2n+1}} (n+0.5)^{\frac{3}{2n+1}} t_b^{\frac{3(1-n)}{2n+1}}} \end{aligned} \tag{3.46}$$

The real diameter is always larger than both approximations because one neglects the web thickness and the other the port. It is worth noting that the length determined by equation (3.42) has exactly the error shown in figure 3.20. Instead, (3.45) has a larger error than depicted in figure 3.21 because the approximation of equation (3.44) has been also added with the substitution of the diameter ratio. It is also possible to determine the value of the diameter ratio for which the diameter calculated with equation (3.41) is equal to the one calculated with equation (3.44):

$$R^{2n+1} = (4n+2) \frac{a G_0^n t_b}{D_0} + 1 \tag{3.47}$$

$$R_{int_D} = 2^{\frac{1}{2n+1}} \tag{3.48}$$

For $R < R_{int_D}$ equation (3.41) gives the smallest error, while for $R > R_{int_D}$ equation (3.44) gives the smallest error. The accuracy of the asymptotic solutions is generally good above $R = 2$ except at very low values of n where larger values of the diameter ratio are needed because the errors increase as n approaches zero.

The parameters that influence the fuel grain length, diameter and their ratio are the fuel density, the oxidizer flux, the burning time, the regression rate constants a and n, the propellant mass and the mixture

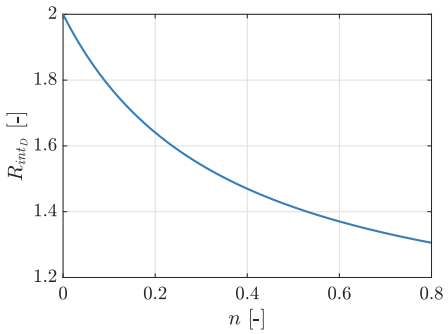

Figure 3.24: Variation of R_{int_D} with regression rate exponent n

ratio. Except the density case, which is trivial, each of them will be discussed separately in the following. The dependency on the value of n is rather complex and with difficult physical interpretation. It is more important here to understand how the value of n influences the dependency of motor length, diameter and length to diameter ratio on the other parameters.

An arbitrary reference example is selected and each parameter of interest is changed in order to sweep a wide range of diameter ratios. In the reference case the regression rate exponent is $n = 0.7$, the oxidizer mass flux is $G_0 = 500\,\mathrm{kg/m^2s}$, the burning time is $t_b = 100\,\mathrm{s}$, the regression rate constant is $a = 0.04$ (for a regression rate in mm/s) and the propellant mass is $M_p = 500\,\mathrm{kg}$. A regression rate exponent nearer to 0.5 will result in lower errors.

3.3.1 *Oxidizer Mass Flux*

For the asymptotic case the volume loading is 100 %, meaning that the grain is a fuel block without a port. For this reason, the initial oxidizer flux has no influence on the motor length and diameter. For very low volume loadings, the port determines the diameter of the grain, and the diameter increases as the square root of the area that is inversely proportional to the oxidizer mass flux. The length of the motor is always independent of the oxidizer mass flux for $n = 0.5$, while it increases with the oxidizer mass flux if $n < 0.5$ and vice versa for $n > 0.5$. The reason is the usual trade-off between regression rate and burning area. If $n < 0.5$ the burning area is more important, so the oxidizer mass flux has to be small. For $n > 0.5$ the regression rate is more important so the oxidizer mass flux has to be high. For low volume loadings the length to diameter ratio increases with the oxidizer mass flux (mainly because the diameter decreases, for $n < 0.5$ also because the length increases). For $n = 1$ the length to diameter ratio is always fixed while for $n = 0$ the length to diameter ratio is linear with the oxidizer mass flux. The explicit dependencies of the two limit cases on the oxidizer mass flux are summarized in table 3.1 and represented in figure 3.25 and 3.26, where the vertical line

Table 3.1: Explicit dependencies of the limit cases on the oxidizer mass flux

$R \to 1$	$R \to \infty$
$L \propto G_0^{0.5-n}$	Null
$D_f \propto G_0^{-0.5}$	Null
$\frac{L}{D_f} \propto G_0^{1-n}$	Null

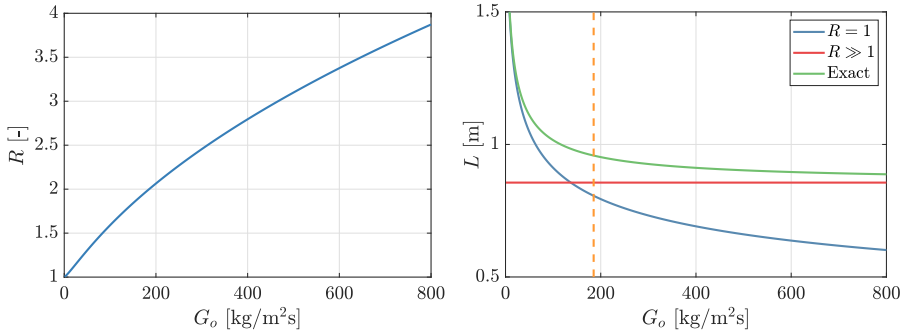

Figure 3.25: Variation of motor parameters with oxidizer mass flux: diameter ratio (left) and length (right)

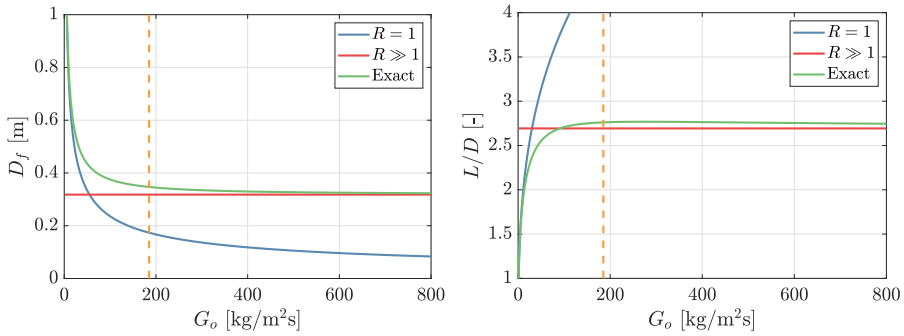

Figure 3.26: Variation of motor parameters with oxidizer mass flux: final diameter (left) and length to diameter ratio (right)

corresponds to $R = 2$. It is possible to notice that the asymptotic solution is accurate above this value.

3.3.2 *Burning Time*

For very low volume loadings both the diameter and the length of the motor scale with the square root of the thrust, which is inversely proportional to the burning time. The length to diameter ratio remains fixed. The fact that the length dependency changes afterwards is related to the mixture ratio shift, therefore the initial mixture ratio has to change in order to keep the same global average mixture ratio. For $n = 0.5$ there is no mixture ratio shift so the dependency remains the same. For $n < 0.5$ the dependency is strengthened, while for $n > 0.5$ is reduced and for $n = 1$ it disappears. As the burning time is increased the port diameter decreases but the web thickness increases. For this reason, the external diameter initially decreases (following the port diameter), reaches a minimum and then increases again (following the web thickness). For $n = 0$ the web thickness is linear with time, for higher n values is sublinear. For $n = 1$ the diameter, length and length to diameter ratio are independent of the burning time. For $n < 1$ the length to diameter ratio decreases with the burning time, and the effect increases as n decreases. The explicit dependencies of the two limit cases on the burning time are summarized in table 3.2 and represented in figure 3.27 and 3.28, where the vertical line corresponds to $R = 2$. It is possible to notice that the asymptotic solution is accurate above this value.

3.3.3 *Regression Rate Constant*

For very low volume loadings the length of the motor scales inversely with the regression rate. The regression rate has no influence on the port size. Therefore, also the length to diameter ratio scales inversely with the regression rate. The fact that the length dependency changes afterwards is related to the mixture ratio shift, therefore the initial mixture ratio has to change in order to keep the same global average mixture ratio. Again, for $n = 0.5$ there is no mixture ratio shift so the dependency remains the same. For $n < 0.5$ the dependency is strengthened, while for $n > 0.5$ is reduced. As the regression rate is increased the web thickness increases too. For this reason, the external diameter starts to increases until it reaches the asymptotic trend. In this case, for $n = 0$ the web thickness is linear with the regression rate coefficient a, while for higher n values is sublinear (because the average regression rate decays with same initial flux and lower final fluxes). Again, for $n = 1$ the length to diameter ratio dependency does not change with the diameter ratio and is always equal to -1. For $n < 1$ the length to diameter dependency is stronger at higher

Table 3.2: Explicit dependencies of the limit cases on the burning time

$R \to 1$	$R \to \infty$
$L \propto t_b^{-0.5}$	$L \propto t_b^{-\frac{1-n}{n+0.5}}$
$D_f \propto t_b^{-0.5}$	$D_f \propto t_b^{\frac{1-n}{2n+1}}$
Null	$\frac{L}{D_f} \propto t_b^{-\frac{3(1-n)}{2n+1}}$

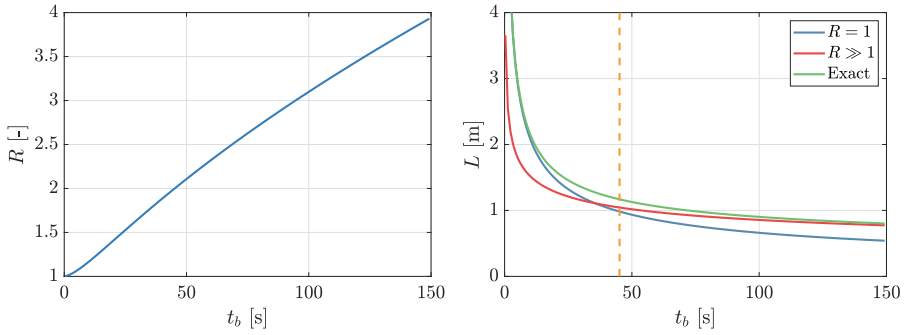

Figure 3.27: Variation of motor parameters with burning time: diameter ratio (left) and length (right)

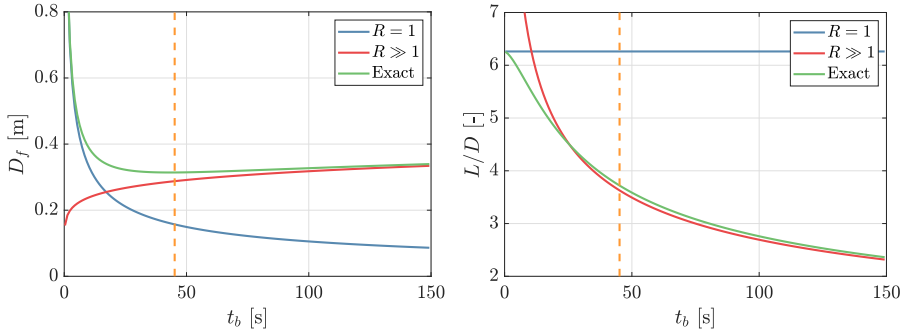

Figure 3.28: Variation of motor parameters with burning time: final diameter (left) and length to diameter ratio (right)

values of diameter ratio, because at low n both the diameter increase and the length decrease are higher. The explicit dependencies of the two limit cases on the regression rate constant a are summarized in table 3.3 and represented in figure 3.29 and 3.30, where the vertical line corresponds to $R = 2$. It is possible to notice that the asymptotic solution is accurate above this value.

3.3.4 *Propellant Mass*

For very low volume loadings the propellant mass dependency follows that of the burning time, the geometry keeps its shape and it is simply scaled as the square root of the thrust and, consequently, of the propellant mass. Again, the fact that the length dependency changes afterwards is related to the mixture ratio shift, therefore the initial mixture ratio has to change in order to keep the same global average mixture ratio. For $n = 0.5$ there is no mixture ratio shift so the dependency remains the same. For $n < 0.5$ the dependency is strengthened, while for $n > 0.5$ is reduced. For high volume loadings, the diameter growth with respect to the propellant mass is sublinear, and is lower for lower n values. For $n = 0$ the length is linear with the propellant mass and the diameter is fixed, therefore even the length to diameter ratio is linear with the propellant mass. This means that for high volume loadings and $n = 0$ the mass that is added or removed is placed almost only after the grain, not around. For $n = 1$ the length to diameter ratio is always fixed. For lower n values,the length to diameter ratio at high values of the diameter ratio is sublinear, and reaches linearity for $n = 0$. The explicit dependencies of the two limit cases on the propellant mass are summarized in table 3.4 and represented in figure 3.31 and 3.32, where the first vertical line corresponds to $R = 3$ while the second one to $R = 2$. It is possible to notice that the asymptotic solution is accurate for high value of the diameter ratio, particularly for the length to diameter ratio.

3.3.5 *Mixture Ratio*

The effect of the mixture ratio on motor dimensions is peculiar with respect to the other parameters seen so far. Qualitatively both solutions show similar trends, the diameter of the motor is only slightly affected by the mixture ratio while the length and the length to diameter ratio decrease with the mixture ratio (the grain is shorter because there is less fuel). In this case the graphs are not shown because a large variation of the mixture ratio (for example from 1 to 16) does not influence significantly the value of the diameter ratio, particularly at the higher mixture ratios. Therefore, once a reference diameter ratio is selected, changing the mixture ratio will not change the diameter ratio so much (and the change is concentrated at the lower mixture ratios)

Table 3.3: Explicit dependencies of the limit cases on the regression rate constant

$R \to 1$	$R \to \infty$
$L \propto a^{-1}$	$L \propto a^{-\frac{2}{2n+1}}$
Null	$D_f \propto a^{\frac{1}{2n+1}}$
$\frac{L}{D_f} \propto a^{-1}$	$\frac{L}{D_f} \propto a^{-\frac{3}{2n+1}}$

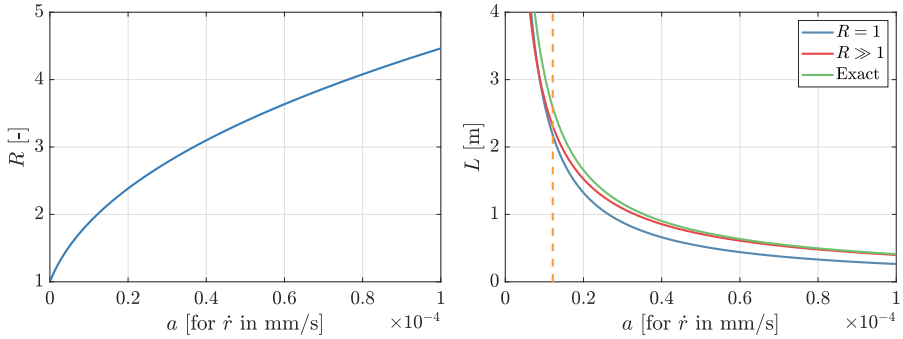

Figure 3.29: Variation of motor parameters with regression rate constant: diameter ratio (left) and length (right)

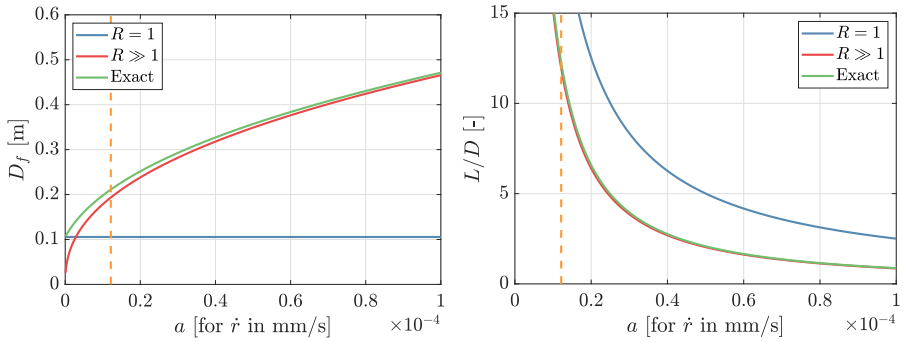

Figure 3.30: Variation of motor parameters with regression rate constant: final diameter (left) and length to diameter ratio (right)

Table 3.4: Explicit dependencies of the limit cases on the propellant mass

$R \to 1$	$R \to \infty$
$L \propto M_p^{0.5}$	$L \propto M_p^{\frac{1}{2n+1}}$
$D_f \propto M_p^{0.5}$	$D_f \propto M_p^{\frac{n}{2n+1}}$
Null	$\frac{L}{D_f} \propto M_p^{\frac{1-n}{2n+1}}$

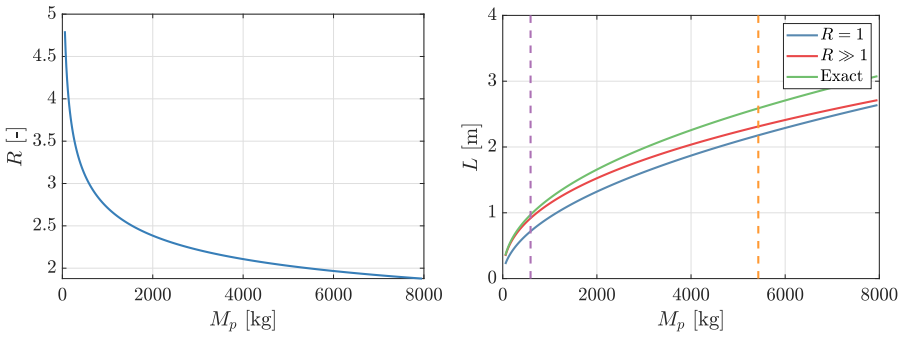

Figure 3.31: Variation of motor parameters with propellant mass: diameter ratio (left) and length (right)

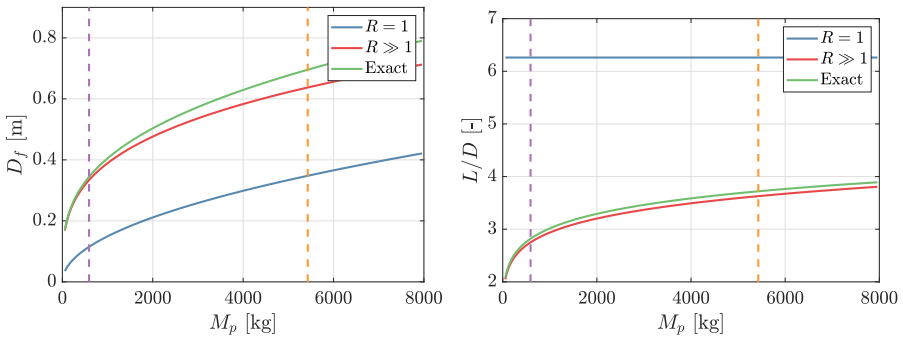

Figure 3.32: Variation of motor parameters with propellant mass: final diameter (left) and length to diameter ratio (right)

Table 3.5: Explicit dependencies of the limit cases on the mixture ratio

$R \to 1$	$R \to \infty$
$L \propto \frac{1}{\varphi_{avg}^{0.5}\left(\varphi_{avg}+1\right)^{0.5}}$	$L \propto \frac{1}{\varphi_{avg}^{\frac{2n}{2n+1}}\left(\varphi_{avg}+1\right)^{\frac{1}{2n+1}}}$
$D_f \propto \frac{\varphi_{avg}^{0.5}}{\left(\varphi_{avg}+1\right)^{0.5}}$	$D_f \propto \frac{\varphi_{avg}^{\frac{n}{2n+1}}}{\left(\varphi_{avg}+1\right)^{\frac{n}{2n+1}}}$
$\frac{L}{D_f} \propto \frac{1}{\varphi_{avg}}$	$\frac{L}{D_f} \propto \frac{1}{\varphi_{avg}^{\frac{3n}{2n+1}}\left(\varphi_{avg}+1\right)^{\frac{1-n}{2n+1}}}$

and so the best approximation is always the same for the entire range depending on the selected reference value of diameter ratio (low or high). It is worth noting that if the diameter ratio does not change significantly, the exponent of equation (3.36) should be correct, because the effect of a changing diameter ratio found previously is not present. Therefore, this means that the slope of the two approximations must coincide. In fact, it is possible to show that for typical values of the mixture ratio and exponent n found in hybrids, both approximations converge to the one for high mixture ratios. The explicit dependencies of the two limit cases on the propellant mass are summarized in table 3.5. If $\varphi_{avg} \gg 1$:

$$L \propto \frac{1}{\varphi_{avg}} \tag{3.49}$$

$$D_f \propto const \tag{3.50}$$

$$\frac{L}{D_f} \propto \frac{1}{\varphi_{avg}} \tag{3.51}$$

In order to increase the fuel mass flow the length of the fuel grain should be proportionally increased without any change on the external diameter. The slight non-linearity of the general case is related to the fact that the port diameter is varied (for the same oxidizer mass flux) every time the oxidizer mass flow is changed. For high mixture ratios, a significant change of the fuel mass has little relative effect on the oxidizer mass so the port variation becomes negligible. It is worth noting that with a mixture ratio of only 2 the oxidizer mass flow is already the 67 % of the total. As always, for $n = 0.5$ there is no mixture ratio shift so the length dependency remains the same. For $n > 0.5$ the dependency is slightly strengthened for φ_{avg} and reduced for $\varphi_{avg} + 1$, for $n < 0.5$ the opposite occurs. For the diameter the dependency on φ_{avg} and $\varphi_{avg} + 1$ is reduced at high diameter ratio values, however they tend to compensate each other.

If $n = 1$, no matter what the value of the diameter ratio is:

$$\frac{L}{D_f} \propto \frac{1}{\varphi_{avg}} \tag{3.52}$$

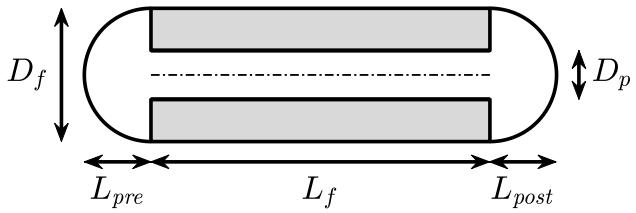

Figure 3.33: Combustion chamber configuration

If $n = 0$ the asymptotic solution gives:

$$L \propto \frac{1}{\varphi_{avg} + 1} \tag{3.53}$$

$$D_f \propto const \tag{3.54}$$

$$\frac{L}{D_f} \propto \frac{1}{\varphi_{avg} + 1} \tag{3.55}$$

However, as in the previous cases, larger values of diameter ratios are needed for low n to reach a good accuracy with the asymptotic solution.

3.3.6 *Chamber Configuration*

A final consideration needs to be done. In general, the combustion chamber of a hybrid motor includes a pre-combustion chamber and a post-combustion chamber. These items affect the length and length to diameter ratio of the whole chamber. To give an indication of this effect, it is possible to approximate the pre- and post-combustion chamber as spherical domes, as represented in figure 3.33. The length and length to diameter ratio of the chamber become:

$$L_{tot} = L_f + D_f \tag{3.56}$$

$$\frac{L_{tot}}{D_f} = \frac{L_f}{D_f} + 1 \tag{3.57}$$

For high length to diameter ratios the effect of the domes is not significant. However, for low length to diameter ratios the domes could have a strong impact.

It is possible to obtain the length of the combustion chamber combining the previous equations. Considering for simplicity only the case of $n = 0.5$:

$$L = \frac{M_{ox}^{0.5}}{2\pi^{0.5} a \varrho_f \varphi_{avg} t_b^{0.5}} + \left[4 a t_b^{0.5} \left(\frac{4 M_{ox}}{\pi} \right)^{0.5} + \frac{4 M_{ox}}{\pi G_0 t_b} \right]^{0.5} \tag{3.58}$$

That for $R \to \infty$ becomes:

$$L = \frac{M_{ox}^{0.5}}{2\pi^{0.5} a \varrho_f \varphi_{avg} t_b^{0.5}} + \frac{2\sqrt{2} a^{0.5} M_{ox}^{0.25} t_b^{0.25}}{\pi^{0.25}} \tag{3.59}$$

In this equation, it is possible to notice that all motor parameters except the propellant mass and mixture ratio have counteracting effects on the motor length. If the grain is shortened too much, its diameter enlargement induces an increase of chamber length through the domes size. The whole problem is much more complicated because the pre- and post-combustion chamber size is related also with proper injection, regression, combustion efficiency and stability. However, it is important to keep in mind that too high values of diameter ratio are not beneficial and could induce not appropriate shapes (the so-called "pizza motors"). It is possible to calculate the volume loading of the whole motor to reinforce this point:

$$\begin{aligned} VL_{tot} &= \frac{\frac{1}{12} VL_{pre} \pi D^3 + \frac{1}{12} VL_{post} \pi D^3 + \frac{1}{4} \pi D^2 L_f VL_f}{\frac{1}{4} \pi D^2 L_f + \frac{1}{6} \pi D^3} \\ &= \frac{\frac{1}{12} VL_{pre} \pi D^3 + \frac{1}{12} VL_{post} \pi D^3 + \frac{1}{4} \pi D^2 L_f \left(1 - \frac{1}{R^2}\right)}{\frac{1}{4} \pi D^2 L_f + \frac{1}{6} \pi D^3} \\ &= \frac{\frac{1}{12} VL_{pre} + \frac{1}{12} VL_{post} + \frac{1}{4} \frac{L_f}{D} \left(1 - \frac{1}{R^2}\right)}{\frac{1}{4} \frac{L_f}{D} + \frac{1}{6}} \end{aligned} \tag{3.60}$$

In case the pre- and post-combustion chamber are empty:

$$VL_{pre} = VL_{post} = 0 \tag{3.61}$$

$$VL_{tot} = \frac{\frac{1}{4} \frac{L_f}{D} \left(1 - \frac{1}{R^2}\right)}{\frac{1}{4} \frac{L_f}{D} + \frac{1}{6}} \tag{3.62}$$

Again if the length to diameter ratio is high the volume loading of the combustion chamber tends to the one of the fuel grain:

$$VL_{tot} \to VL_f \tag{3.63}$$

However, if the length to diameter ratio of the grain goes to zero the volume of the motor is dominated by the empty domes:

$$VL_{tot} \to 0 \tag{3.64}$$

Again these equations confirm that a single port hybrid rocket has to operate in a certain range of diameter ratios (not too low or too high) in order to achieve good performance metrics.

4

HEAVYWEIGHT MOTOR DESIGN

Hybrid rocket motors have long been recognized as a propulsion option with strong potential [82] due to their inherent advantages like simplicity, reliability, safety, start-stop-restart and thrust control capabilities [2, 3, 22]. Unfortunately, this potential has not been exploited to date [8, 46, 52, 68, 114]. One of the main reasons is related to the low regression rate of the fuel, which is limited by the blocking mechanism of the convective heat transfer to the grain surface caused by the blowing of the ablating fuel [32, 74–77]. This mechanism has been thoroughly explained in chapter 2 together with the whole hybrid combustion process. Even for moderate thrusts, the low regression rate prevents the realization of fuel grains with an acceptable volume loading and length [89], as it is possible to understand following the mathematical treatment of chapter 3 where some simple relations for a preliminary hybrid motor optimization have been derived.

Since the Sixties and for several decades, the main way to address this issue has been the use of multiport grains [105, 107]. However, multiport grains are penalized by complexity, structural issues, different mass flows and regression rates between ports, and high fuel residuals [10, 61]. A significant effort has been spent in recent years to find a way to increase the regression rate in order to use a much more effective single-port geometry [30]. Some interesting solutions that have been investigated are the addition of energetic materials [25, 41, 53, 92], mixing devices like diaphragms [19, 20, 47], unique injection patterns like swirl injectors [9, 12, 13, 15–18, 62–65, 73, 83–86, 95], and innovative liquefying solid fuels like paraffin-based fuels [54, 57–59].

The two most promising technologies that are able to guarantee a high regression rate and a high combustion efficiency are swirl injectors and paraffin-based fuels. The first approach is based on the formation of a strong turbulence level inside the combustion chamber, caused by the injector itself that forces the oxidizer mass flow to enter the combustion chamber with a strong tangential velocity component and to follow a helical pattern along the motor axis. The increased turbulence enhances the heat transfer to the fuel surface and promotes a better mixing of the reactants, consequently improving both the regression rate and the combustion efficiency. The second approach is based on the use of a new class of fuels called liquefying fuels, generally based on paraffin wax. These fuels melt on the surface, creating a thin liquid layer with a very low viscosity. Thanks to the low viscosity, the shear stresses of the port flow are able to perturb the surface, generating small waves. Fuel droplets detach from the tip of the waves and are entrained by the gas flow. Adding another mass

transfer mechanism to the conventional one, paraffin-based fuels are able to reach a regression rate several times higher than conventional ones, thus giving the possibility to design single-port hybrids for various applications [31, 51, 56].

At the Center of Studies and Activities for Space "G. Colombo" of the University of Padova, two different solutions have been developed within the Hybrid Propulsion Group in order to design hybrid rocket motors with high regression rate and high combustion efficiency, depending on the intended application. The first approach is based on swirl injection of HTP burning with a HDPE solid grain, while the second one uses an axial injector and a propellant combination of HTP and a paraffin-based fuel. In both cases the HTP is first forced to pass through a catalytic reactor, where it decomposes into gaseous oxygen and water vapor at a temperature of around 1000 K, and then is injected inside the motor where its temperature is high enough to thermally decompose and ignite the fuels that are commonly used. This technique makes the motor self ignitable and restartable. HTP has several further advantages compared to other available oxidizers: it is storable, it allows to use gaseous injection, which in general has a very stable behavior since there are no droplet evaporation instabilities, and it has no problems of poor atomization at low pressure drops. Moreover, it permits to get full advantage of swirl oxidizer injection.

In this chapter the design of a hybrid rocket motor for test purpose will be presented and discussed, followed by the numerical investigation that has been carried out in order to support the design process and verify the result itself.

4.1 PRELIMINARY MOTOR DESIGN

The preliminary design of a hybrid rocket motor is based on a simple one-dimensional code. The first step of the process is to relate the thrust of the motor with the total mass flow:

$$F = \dot{m}_{tot} c^\star C_F = \dot{m}_{tot} I_{sp} g_0 \tag{4.1}$$

where characteristic velocity, thrust coefficient and specific impulse are defined as:

$$c^\star = \sqrt{\frac{R}{M_m}\frac{T_{cc}}{\gamma}\left(\frac{\gamma+1}{2}\right)^{\frac{\gamma+1}{\gamma-1}}} \tag{4.2}$$

$$C_F = \sqrt{\frac{2\gamma^2}{\gamma-1}\left(\frac{2}{\gamma+1}\right)^{\frac{\gamma+1}{\gamma-1}}\left[1-\left(\frac{P_e}{P_{cc}}\right)^{\frac{\gamma-1}{\gamma}}\right]} + \frac{P_e - P_a}{P_{cc}}\frac{A_e}{A_t} \tag{4.3}$$

$$I_{sp} = \frac{c^\star C_F}{g_0} \tag{4.4}$$

The thrust of the motor is a requirement coming from the intended mission profile, while the characteristic velocity and the specific im-

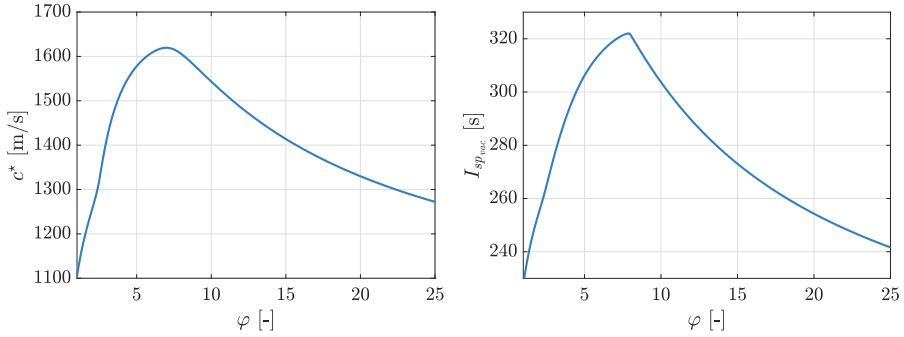

Figure 4.1: Mixture ratio influence on characteristic velocity (left) and vacuum specific impulse (right) for HTP burning with HDPE, where $\varepsilon = 60$ and $P_{cc} = 20\,\text{bar}$

pulse can be computed with a thermochemical code [45] as a function of the mixture ratio, which is defined as the ratio between the oxidizer mass flow and the fuel mass flow:

$$\varphi = \frac{\dot{m}_{ox}}{\dot{m}_f} \tag{4.5}$$

Consequently, it is possible to evaluate the total mass flow that is needed to match the expected application.

As it can be seen in figure 4.1, the optimal mixture ratio for HTP burning with HDPE is around 6.5 to 7.5. Almost identical results are obtained for the propellant combination HTP and paraffin wax. Choosing the mixture ratio in this range, it is possible to compute oxidizer and fuel mass flows from the total propellants mass flow:

$$\dot{m}_{tot} = \dot{m}_{ox} + \dot{m}_f = \dot{m}_{ox}\left(1 + \frac{1}{\varphi}\right) = \dot{m}_f(1 + \varphi) \tag{4.6}$$

$$\dot{m}_{ox} = \frac{\dot{m}_{tot}}{1 + \frac{1}{\varphi}} \tag{4.7}$$

$$\dot{m}_f = \frac{\dot{m}_{tot}}{1 + \varphi} \tag{4.8}$$

The design of the small hybrid rocket motor that is here presented is tailored for space missions, where typical applications have a thrust that ranges between 100 N and 1000 N as have been shown more in detail in chapter 1. For most of the experimental activity, the thrust level has been chosen as about 300 N that is obtained with an oxidizer mass flow rate of around 100 g/s.

Considering a hybrid motor that uses a fuel grain with a single cylindrical port, the fuel mass flow depends on the fuel properties and on the grain geometric dimensions:

$$\dot{m}_f = \dot{r}\pi\varrho_f D_p L_p \tag{4.9}$$

where the space-time averaged form of the regression rate is expected to follow the empirical formula (2.34) defined in chaper 2:

$$\dot{r} = aG_{ox}^n \tag{4.10}$$

and the oxidizer mass flux is defined as:

$$G_{ox} = \frac{\dot{m}_{ox}}{A_p} \tag{4.11}$$

With these last relations it is possible to design the grain shape, in terms of initial and final diameter and length, when the regression rate coefficients a and n are known.

For HTP burning with a paraffin-based fuel or with HDPE, $n = 0.5$ is a good assumption, as was already demonstrated by several international researchers [79, 112, 113] and confirmed by the Hybrid Propulsion Group of the University of Padova during other test campaigns performed under similar conditions. It is possible to demonstrate that if the exponent n is equal to 0.5 and if the oxidizer mass flow is kept constant, the mixture ratio is constant during the burn at any port diameter size. In fact, recalling equation (2.52) derived in chapter 2:

$$\varphi = \frac{\dot{m}_{ox}^{1-n} D_p^{2n-1}}{a \pi^{1-n} 4^n \varrho_f} \tag{4.12}$$

Moreover, thanks to the large amount of data collected over the years by the Hybrid Propulsion Group of the University of Padova, a first guess of the coefficient a has also been possible. The preliminary value for the swirl injection configuration with HTP and HDPE has been chosen as $a = 0.15$, while for the axial injection configuration with HTP and paraffin wax the coefficient has been evaluated as $a = 0.1$ (these values are used to compute the regression rate in mm/s with an oxidizer mass flux measured in kg/m^{2}s).

Finally, the pressure inside the combustion chamber can be estimated using the well-known equation:

$$P_{cc} = \frac{\dot{m}_{tot} c^\star}{A_t} \tag{4.13}$$

The characteristic velocity, as well as the specific impulse, has a dependency not only on the mixture ratio but also on the combustion chamber pressure. However, the influence is negligible when the pressure is high enough, as a rule of thumb higher than 10 bar, as it can be seen from figure 4.2. Furthermore, the nozzle throat erosion is proportional to the combustion chamber pressure. A trade-off is required and for these reasons the throat area has been computed to obtain a pressure of around 20 bar inside the combustion chamber. Moreover, the exit section diameter has been evaluated in order to have a supersonic flow perfectly adapted at ambient pressure, for ground testing purpose:

$$\varepsilon = \frac{A_e}{A_t} = \frac{1}{Ma_e} \sqrt{\left[\frac{2}{\gamma + 1} \left(1 + \frac{\gamma - 1}{2} Ma_e^2 \right) \right]^{\frac{\gamma+1}{\gamma-1}}} \tag{4.14}$$

$$Ma_e = \sqrt{\frac{2}{\gamma - 1} \left[\left(\frac{P_t}{P_a} \right)^{\frac{\gamma-1}{\gamma}} - 1 \right]} \tag{4.15}$$

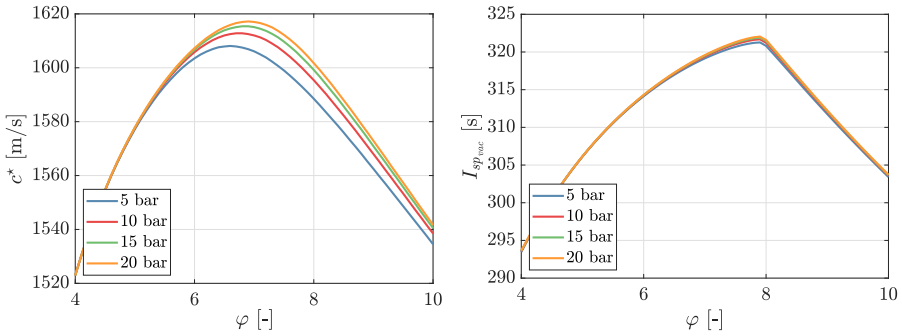

Figure 4.2: Pressure influence on characteristic velocity (left) and vacuum specific impulse (right) for HTP burning with HDPE, where $\varepsilon = 60$

During the burning time, the internal geometry of the motor changes due to the consumption of both the fuel grain and the thermal protections. However, assuming that the characteristic velocity is mainly affected by the mixture ratio value and only slightly affected by the small change in the fluid dynamic flow pattern, between the start and the end of the burn it is reasonable to expect an almost constant combustion efficiency. Therefore, if the oxidizer mass flow is held constant, given all the aforementioned assumptions, the combustion chamber pressure should remain constant as well, if no erosion of the nozzle throat occurs. This allows to have an almost constant thrust during the entire burning time.

4.2 DETAILED MOTOR DESIGN

The hybrid rocket motor has been designed specifically for ground testing purpose and consequently it has a heavy battleship design, as it can be seen in figure 4.3. The combustion chamber case has been designed to withstand a maximum pressure of 40 bar with a high safety factor. It is composed of a cylindrical section and two flanges, connected together by a set of eight threaded rods. The basic equations used to design these metal components are those for cylindrical pressure vessel and those for circular plates with central holes. The thickness of the cylindrical case and of the flanges depends on the tensile strength σ of the material used, which in this case is carbon steel:

$$t_{cyl} = SF\frac{P_{cc}D_{cyl}}{2\sigma} \tag{4.16}$$

$$t_{fl} = \sqrt{SF\frac{kP_{cc}D_{fl}^2}{4\sigma}} \tag{4.17}$$

where SF is the design safety factor and k a geometric coefficient that depends on the ratio between the outer diameter and the hole diameter of the circular plate.

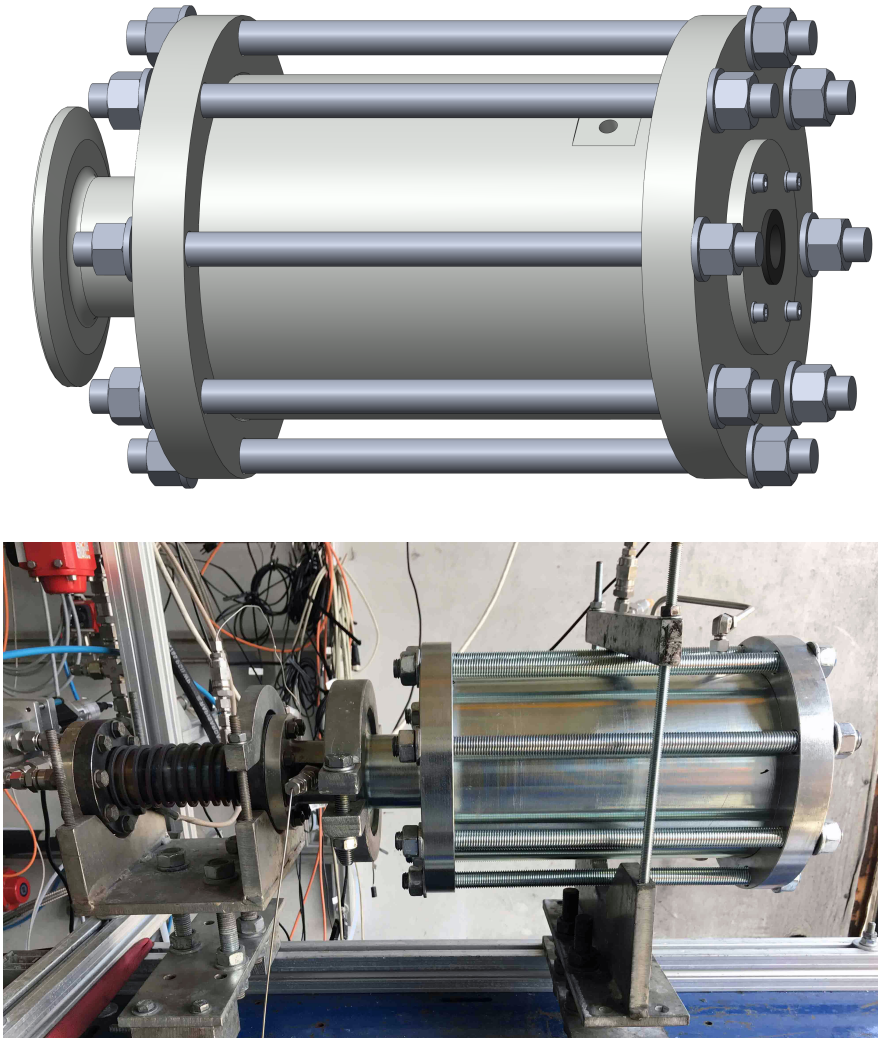

Figure 4.3: CAD model (top) and real model (bottom) of the hybrid rocket motor assembled on the test bench

The sealing between the flanges and the cylinder is granted by a graphite braid packing seal, which is able to withstand high temperatures. The combustion chamber design is very simple and allows to have a different motor length only changing the cylindrical section.

The inlet flange is directly connected to the catalytic reactor with a two-piece clamping collar. Here it is possible to add the swirl injector or the axial injector, depending on the configuration that needs to be tested. The catalytic reactor will not be discussed in detail here, as it was already developed by the Hybrid Propulsion Group of the University of Padova. The outlet flange accommodates a convergent-divergent graphite nozzle, which is held in place with a smaller steel flange. These two flanges are connected together by four bolts, specifically designed to break in case of an overpressure higher than 60 bar inside the motor. The rupture bolts allow to have a predetermined failure point of the system, in order to avoid major

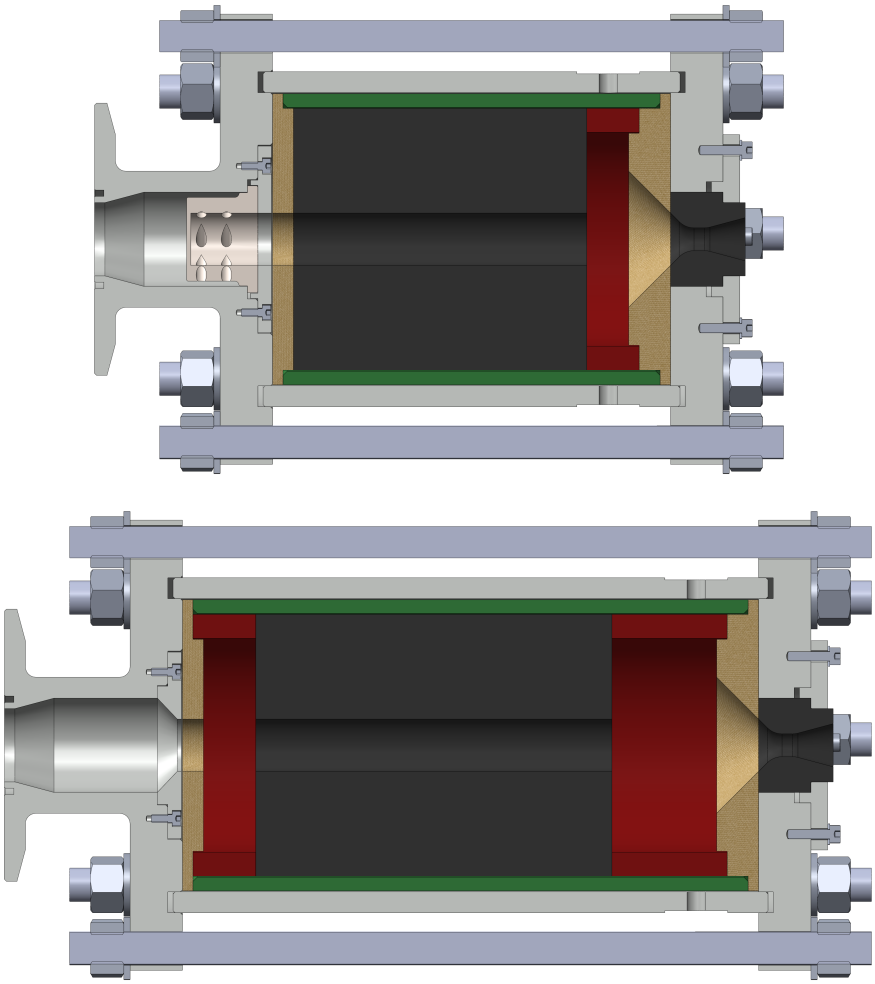

Figure 4.4: CAD model section view of the swirl injection (top) and the axial injection (bottom) hybrid rocket motor

damage to the combustion chamber or the whole experimental setup in case of an unexpected event.

The combustion chamber presents two pressure sensors connections and several thermocouples ports. Two pressure sensors can be used for redundancy or to measure both low and high frequency instabilities, if a sensor with a very fast response time is employed. Several thermocouples can be used to measure the temperature of the thermal protections and to check that the temperature of the structural components does not get too high. Unfortunately, the thermocouples cannot be used to control the temperature inside the combustion chamber due to their measurement range limits, but eventually can be used to evaluate the fuel regression rate if placed inside the solid grain at different radial positions.

As previously said, the two different configurations of hybrid rocket motor are the one with swirl injected HTP burning with HDPE, and the one that uses axial injection of HTP together with a paraffin-based fuel grain. The two configurations are represented in figure 4.4. It is

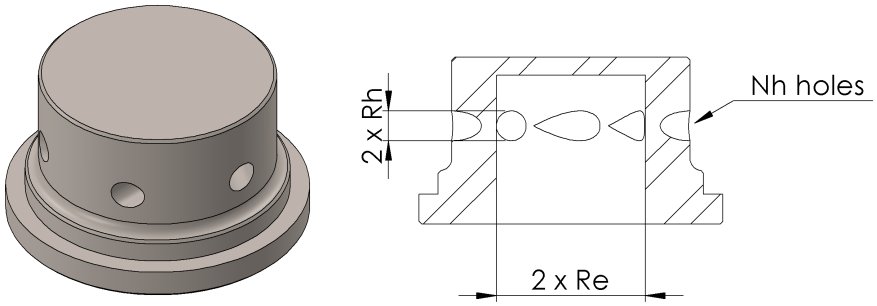

Figure 4.5: Characteristic geometric dimensions of the swirl injector

possible to see that inside the combustion chamber metal case there is a number of parts assembled in a cartridge-like fashion. The cartridge is composed of a cylindrical liner made of HDPE, which protects the motor case and contains all the expendable components. The expendable components are joined together using high temperature silicone to prevent leakages at the interfaces. Starting from the inlet side there is the inlet flange thermal protection, the pre-combustion chamber, the solid fuel grain, the post-combustion chamber, and the outlet flange thermal protection. The pre-combustion chamber is generally used only in the axial injection configuration, while the length of the pre- and post-combustion chambers can be varied depending on the motor design. The two flange thermal protections are made of a phenolic composite reinforced with cotton fabric. This composite material, commonly known as cotton-phenolic, is a good compromise between performance and cost compared to carbon-phenolic.

The swirl injection configuration, as it is clear from its name, employs a swirl injector, which is of the inward type with fully tangential holes. A common parameter used to describe this type of injector is the geometric swirl number [14, 35]:

$$SN_g = \frac{R_e(R_e - R_h)}{R_h N_h} \tag{4.18}$$

where R_e is the internal radius of the injection plate outlet section, R_h is the radius of the tangential holes, and N_h is the number of holes. These geometric dimensions are better shown in figure 4.5. It is important to underline that the geometric swirl number is not equal to the local swirl number at the injection plate or inside the combustion chamber. The effective swirl number is defined as the ratio between the axial flux of the tangential momentum and the axial flux of the axial momentum [14]:

$$SN = \frac{\int \varrho v_x v_\vartheta R dA}{R_0 \int \varrho v_x^2 dA} \tag{4.19}$$

However, the effective swirl number at the injection plate is directly proportional to the geometric swirl number. The advantage of using

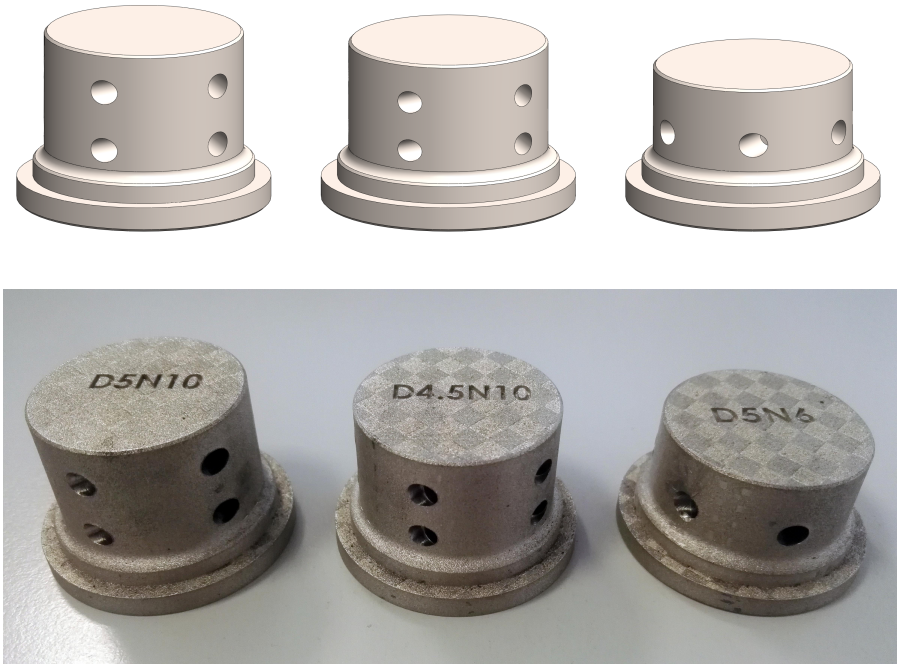

Figure 4.6: CAD model (top) and real model (bottom) of three fully tangential swirl injectors: from left to right $SN_g = 2$, $SN_g = 2.53$, $SN_g = 3.33$

the latter parameter is that it can be evaluated by means of only geometric quantities, without the need for local measurements of specific fluid unknowns.

The swirl intensity of the flow field inside the combustion chamber strongly affects the regression rate. For this reason, three different swirl injectors have been taken into account, as it can be seen in figure 4.6: one with $SN_g = 2$, obtained with ten 5 mm diameter holes, placed on two ranks; one with $SN_g = 2.53$, obtained with ten 4.5 mm diameter holes, placed on two ranks; one with $SN_g = 3.33$, obtained with six 5 mm diameter holes, placed on one rank. Two more constraints have been given to the geometry of the injection plate. First, the Mach number across a single tangential hole cannot exceed 0.3 to avoid a too high pressure drop. Second, the length to diameter ratio of the tangential holes must be greater than 1.5 to ensure that the flow across each hole almost follows the direction of its axis, in order to have a real fully tangential injection.

On the other hand, the axial injection configuration uses an axial injector that is basically a circular plate with a certain number of holes. The purpose of the plate is to better distribute and straighten the flow of decomposed hydrogen peroxide, coming from the catalytic reactor, before entering inside the pre-combustion chamber. Again, the ratio between the area of the full plate and the area of the perforated plate has been evaluated in order to have a maximum Mach number of 0.3 across the holes and consequently a minimum pressure drop along the injection plate.

4.3 NUMERICAL INVESTIGATION

A numerical investigation of the hybrid rocket motor with swirl oxidizer injection has been carried out, in order to verify the design of both the injection plate and the whole motor. A commercial CFD code, which solves the RANS equations associated with the flow field inside the combustion chamber, has been used to analyze its characteristic behavior. If the boundary conditions are properly setup and the numerical models are carefully chosen, a numerical analysis can be a powerful instrument to predict the system operation and therefore it can be used to support the design process of a hybrid rocket motor. Moreover, it allows to visualize the flow field inside the combustion chamber and to measure local parameters in critical positions that are otherwise impossible to reach in an experimental setup.

Only the configuration that uses swirl injected HTP burning with HDPE has been studied, since the axial injection configuration can be designed just with the one-dimensional code. First, the swirl injector has been analyzed on its own to verify the results of the design process, in terms of pressure drop along the injector and of streamlines angle with respect to the holes axes. Afterwards, several configurations of the whole hybrid rocket motor have been examined, in order to refine the design of the combustion chamber, if needed, and to predict the results of the experimental campaign.

The numerical simulations take advantage of the rotational periodicity of the geometries, reducing the axisymmetric flow field to a single slice. The slice covers an angle that depends on the number of injector holes, where a motor portion corresponding to a single injector hole is simulated. This approach permits to reduce the computational time needed to obtain a numerical solution.

4.3.1 *Boundary Conditions and Models*

The setup of all the numerical simulations is similar regardless of the analyzed configuration. In figure 4.7 the flow field geometry associated with both the swirl injector and the combustion chamber is presented, in order to show the different surfaces where the following boundary conditions are imposed.

An inlet boundary condition is given at the injector holes surface and at the solid grain surface. This means that both the mass flow rate and the temperature of the injected chemical species are fixed. The mass flow rate is injected tangentially to the inlets area and the velocity is computed from the mass flow rate definition:

$$\dot{m} = \varrho \mathbf{v} \cdot \mathbf{A} \tag{4.20}$$

The oxidizer is HTP at a concentration of 90 % by weight. Since the catalytic reactor has not been studied here, the oxidizer is injected

Figure 4.7: Flow field associated with the hybrid motor and divided by color into injector, fuel grain, post-combustion chamber and nozzle

already decomposed into a mixture of gaseous oxygen and water vapor at a temperature of 1018 K. The decomposition temperature is computed with a thermochemical code [45], while the chemical composition of the decomposed HTP mixture depends only on its concentration. For pure hydrogen peroxide it is possible to obtain the following formula:

$$2\,H_2O_2 \longrightarrow 2\,H_2O + O_2 \tag{4.21}$$

while for a concentration of 90 % by weight the result is:

$$28.6\,H_2O_2 + 6\,H_2O \longrightarrow 34.6\,H_2O + 14.3\,O_2 \tag{4.22}$$

The fuel is HDPE and is injected already decomposed as gaseous ethylene at a temperature of 900 K, which is approximately the temperature of the pyrolyzed grain surface. The mixture ratio is fixed at 6.

A fixed pressure is imposed at the outlet section of the swirl injectorif only the injection plate is analyzed, or at the nozzle exit surface of the complete hybrid rocket motor. In the first case a pressure of 20 bar has been chosen, because this value is comparable to the one expected inside the combustion chamber and it allows to characterize the injection section during real steady operating conditions of the motor. On the other hand, in the second case the nozzle perfectly expands the flow to ambient pressure, in order to simulate the ground firing tests. However, a space motor has a higher expansion ratio and works in a vacuum environment.

All the other surfaces are modeled as adiabatic walls. Here the no-slip condition is imposed to the flow, in order to take into account the viscosity of the fluid:

$$v = v_w = 0 \tag{4.23}$$

When the whole hybrid rocket motor is analyzed, the combustion process is simplified with a single-step chemical reaction:

$$\begin{aligned} 2211\,O_2 + 737\,C_2H_4 \longrightarrow\ & 1274\,CO_2 + 1247\,H_2O \\ & + 200\,CO + 152\,H_2 + 150\,OH + 138.5\,O_2 \end{aligned} \tag{4.24}$$

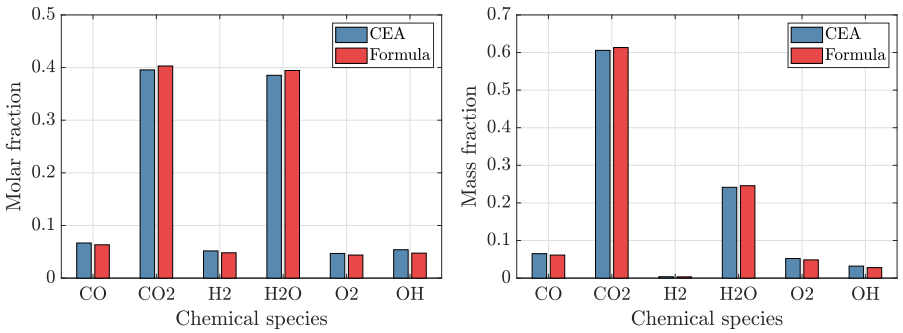

Figure 4.8: Comparison between thermochemical calculations and single-step reaction: molar fractions (left) and mass fractions (right)

The chemical products have been chosen using the results of a thermochemical code [45], where the species with a molar fraction lower than 1×10^{-3} have been neglected in order to reduce the required computational time. In figure 4.8 a comparison between the thermochemical code calculations and the single-step chemical reaction is presented, for both molar and mass fractions of the reaction products. In order to model the flame zone, the mixture ratio used to obtain the combustion reaction formula is equal to the stoichiometric one. The combustion process is analyzed considering all the chemical species as ideal gases and using the eddy dissipation model to treat the chemistry of the flame. This approach does not include chemical kinetics effects and is a good approximation for typical hybrid rocket motors where the chemical reactions rate is higher than the mixing rate of the reactants in the turbulent diffusion flame. This is summarized by a large Damköhler number, which is defined as the ratio between the turbulent time scale and the chemical time scale:

$$Da = \frac{\tau_t}{\tau_c} \gg 1 \tag{4.25}$$

The turbulence model used in the numerical simulations is the isotropic turbulence model $k - \omega$ SST. It was developed to combine the advantages of the $k - \varepsilon$ model with the ones of the $k - \omega$ model, using a blending function to switch between the two [80]. The first model is used in the free-stream zone, where its accuracy is higher, while the second one is used in the near-wall region, because it can precisely simulate the flow in the viscous sub-layer. The $k - \omega$ SST is a two-equations eddy-viscosity turbulence model, meaning that it includes two extra transport equations to characterize the turbulent properties of the flow. The first transported variable is the turbulent kinetic energy k, which determines the energy in the turbulence, while the second transported variable is the specific dissipation rate ω, which determines the scale of the turbulence.

The numerical investigation has been carried out with a steady-state, pressure-based, coupled solver, where the governing equations

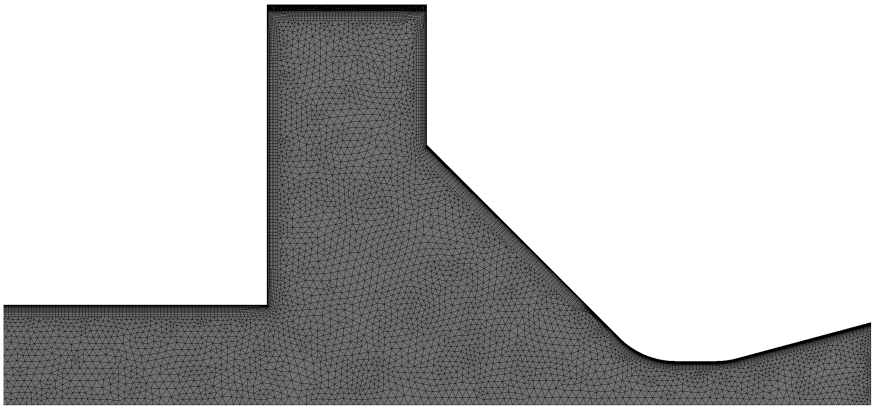

Figure 4.9: Magnified section of the unstructured mesh

Table 4.1: Test matrix of the analyzed configurations

Config	SN_g [-]			L_{post} [mm]			D_p [mm]	
	2	2.53	3.33	20	35	50	25	50
1	•					•	•	
2		•				•	•	
3			•			•	•	
4			•		•		•	
5			•	•			•	
6	•					•		•
7		•				•		•
8			•			•		•

have been discretized with a second order method. The mesh type is unstructured with tetrahedral elements, whose overall size, local refinements and inflations have been chosen after a convergence study. In figure 4.9 a magnified section of the unstructured mesh is shown. Here it is possible to better visualize the local size of the tetrahedral elements in the post-combustion chamber and in the nozzle region.

4.3.2 *Configurations and Results*

Only the configuration with swirl injected HTP burning with HDPE has been studied. The first part of the numerical investigation is related to the analysis of the three different swirl injectors, which are characterized by a geometric swirl number of $SN_g = 2$, $SN_g = 2.53$, and $SN_g = 3.33$ respectively. Once the design of the injectors has been verified, several configurations of the whole hybrid rocket motor have been examined. Three main parameters can be varied, namely the injector geometric swirl number, the post-combustion chamber length, and the diameter of the fuel circular port. In table 4.1 the test matrix of all the analyzed configurations is presented.

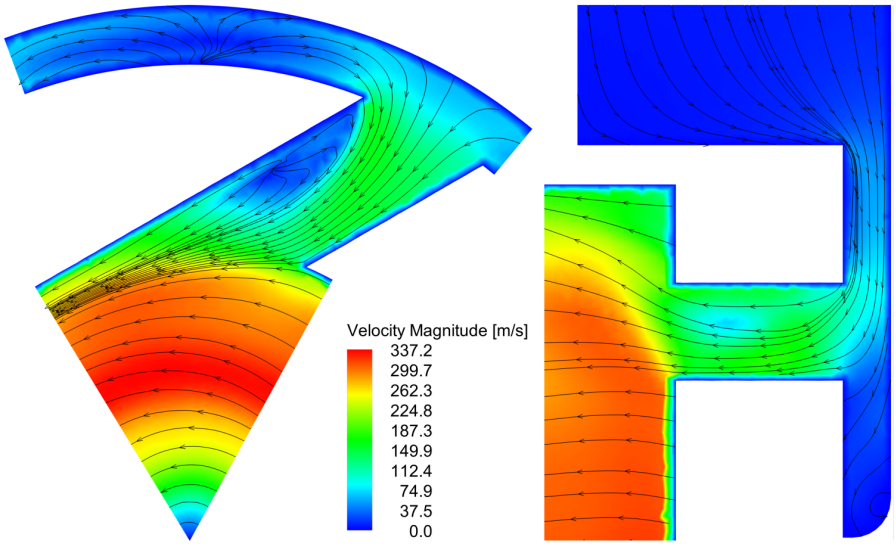

Figure 4.10: Velocity contour and streamtraces in a swirl injector

It is important to underline that the length of the solid fuel depends on the selected swirl injector, because a higher swirl number results in a faster regression rate. For this reason, the grain length has been selected accordingly, in order to keep the overall mixture ratio of the hybrid rocket motor constant. Using the experimental results of similar firing tests performed by the Hybrid Propulsion Group of the University of Padova, the length has been evaluated as following: for $SN_g = 2$ the grain is 177 mm long, for $SN_g = 2.53$ the grain is 144 mm long and for $SN_g = 3.33$ the grain is 118 mm long.

The first part of the numerical investigation analyzes the swirl injector on its own to verify the results of the design process, in terms of pressure drop along the injector and of streamlines angle with respect to the holes axes. The three different configurations have been studied, namely $SN_g = 2$, $SN_g = 2.53$ and $SN_g = 3.33$. The pressure drop along the injectors is about 5 % of the upstream pressure, or around 1 bar, for all the analyzed configurations. However, this result is trivial because it comes from the initial constrain on the Mach number that cannot exceed 0.3. Regarding the streamlines shape, the oxidizer flow is injected into the combustion chamber following a path that is almost parallel to the holes axes, ensuring that the geometric swirl number of the real swirl injector is equal to the design one. The streamlines on two sections of a swirl injector are shown in figure 4.10: the first section is along a plane parallel to the holes axes and perpendicular to the motor axis, while the second one is along a plane parallel to both one hole axis and the motor axis. In these figures just one slice of the swirl injector, which corresponds to a single injector hole, is visible.

The most important part of the numerical investigation is related to the simulation of the whole combustion chamber. Following the test

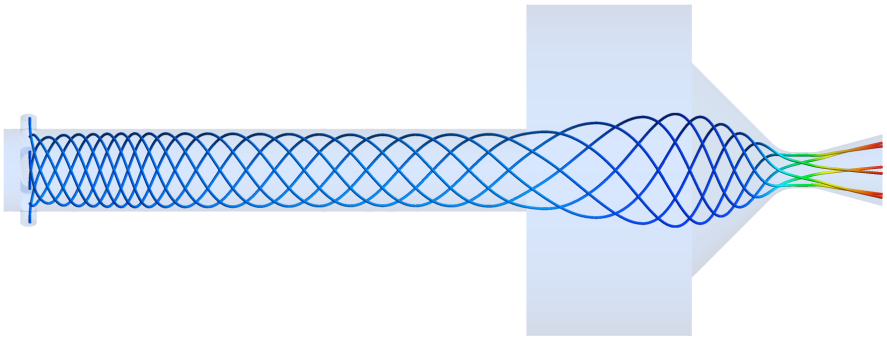

Figure 4.11: Characteristic helical streamlines associated with swirl injection

Table 4.2: Performance parameters of the analyzed configurations

Config	$c^{\star}_{th}$ [m/s]	$c^{\star}_{num_P}$ [m/s]	$c^{\star}_{num_F}$ [m/s]	η_P [%]	η_F [%]
1	1593.3	1632.9	1554.3	102.5	97.6
2	1593.3	1650.5	1557.1	103.6	97.7
3	1593.3	1678.7	1559.7	105.4	97.9
4	1593.3	1690.2	1560.4	106.1	97.9
5	1593.3	1705.1	1560.3	107.0	97.9
6	1593.3	1632.3	1551.6	102.4	97.4
7	1593.3	1651.9	1554.3	103.7	97.6
8	1593.3	1678.7	1555.2	105.4	97.6

matrix already presented, the influence of three parameters has been studied: the injector geometric swirl number, the post-combustion chamber length, and the grain port diameter. It is important to underline that the swirl injector forces the gaseous oxidizer to enter the combustion chamber with a strong tangential velocity component. The consequence is the formation of the characteristic helical streamlines that distinguish the flow field of this particular type of hybrid rocket motor, as it can be seen in figure 4.11. The increased turbulence level enhances the heat transfer to the fuel surface and guarantees a better mixing between the chemical species inside the combustion chamber. The result is that the fuel grain burns at faster rates and that a more complete combustion is achieved, thus guaranteeing a higher regression rate and a higher combustion efficiency.

A summary of the performance parameters for all the analyzed configurations is presented in table 4.2. Two different characteristic velocities can be evaluated from the numerical results, namely the characteristic velocity computed from the pressure:

$$c^{\star}_{num_P} = \frac{P_{cc} A_t}{\dot{m}_{tot}} \tag{4.26}$$

and the characteristic velocity computed from the thrust:

$$c^{\star}_{num_F} = \frac{F}{\dot{m}_{tot} C_F} \tag{4.27}$$

where the combustion chamber pressure is the average value evaluated on a section just before the nozzle convergent part. Moreover, the thrust is computed as:

$$F = \dot{m}_{tot} v_e + (P_e - P_a) A_e \tag{4.28}$$

and the thrust coefficient includes a factor that takes into account the non monodimensionality of the isentropic flow through the nozzle, because the geometry is characterized by a certain divergent angle:

$$C_F = C_{F_0} \frac{1 + \cos\left(\frac{\alpha}{2}\right)}{2} \tag{4.29}$$

However, this coefficient does not take into account other real nozzle losses, like viscous effects or heat transfers, and as a result the characteristic velocity computed from the thrust could be slightly higher, generally no more than 1 % to 2 % [109]. Depending on the performance parameter considered, two different expressions of the motor efficiency can be obtained:

$$\eta_P = \frac{c^\star_{num_P}}{c^\star_{th}} \tag{4.30}$$

$$\eta_F = \frac{c^\star_{num_F}}{c^\star_{th}} \tag{4.31}$$

where the theoretical characteristic velocity is computed with a thermochemical code [45], considering a shifting equilibrium flow model.

Considering the results of the numerical investigation, it is possible to realize that the pressure efficiency is higher than 100 %, even if this is physically unreasonable. As theoretically examined by several authors, this phenomenon is the consequence of a reduction of the effective throat area when a swirling flow, which has a strong tangential velocity, passes through a convergent-divergent nozzle, due to the centrifugal forces that oppose the flow when it approaches the nozzle throat [1, 38, 43, 72]. For this reason, the efficiency computed from the thrust has been used as performance parameter in order to compare the different test cases.

All the analyzed configurations exhibit a very high efficiency, above 97 %. It is hard to see a significant increase of the combustion efficiency with higher geometric swirl numbers or longer post-combustion chambers. This is imputable to the fact than even the configuration with the lower geometric swirl number and the shorter post-combustion chamber is able to create a turbulence level high enough to promote an almost complete mixing of the chemical species inside the motor. It is important to underline that the swirl intensity decreases along the motor axis and in particular inside the post-combustion chamber, where the difference between its diameter and the fuel port diameter causes a decrease of the tangential velocity for the angular momentum conservation [15–18, 83–85].

However, three main trends can be recognized. Given the same initial port diameter, the motor efficiency increases with a higher geometric swirl number. Unfortunately, as already said, it is not possible to see any influence of the post-combustion chamber length because the effect of the high geometric swirl number is predominant, but it is reasonable to affirm that the motor efficiency would also increase with a longer post-combustion chamber. On the other hand, for a fixed swirl number, a bigger port diameter has the opposite effect on the motor efficiency because the reduced difference between the port area and the post-combustion chamber area diminishes the mixing capabilities of this motor section. In figure 4.12 and 4.13, the contours of relevant variables are presented, in order to compare the results between the same configuration with different port diameters, namely configuration 3 and configuration 8.

It is important to underline that the larger port diameter causes the formation of a recirculation zone immediately after the swirl injector, due to the large difference between the two diameters and the lack of a pre-combustion chamber. This could lead to a higher and uneven regression rate at the fuel grain head-end.

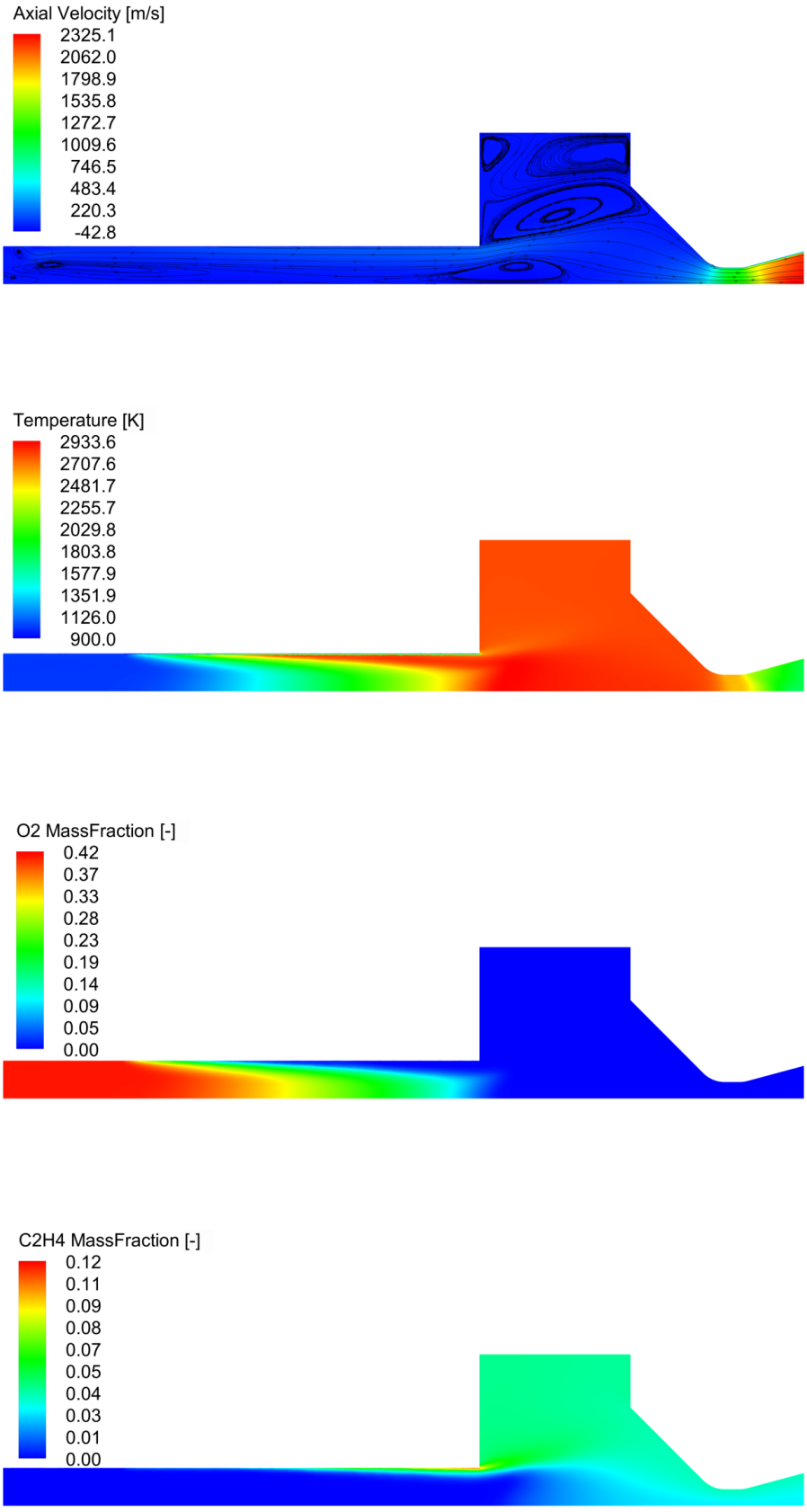

Figure 4.12: Configuration 3 numerical results: contours of velocity, temperature, oxygen and ethylene mass fractions

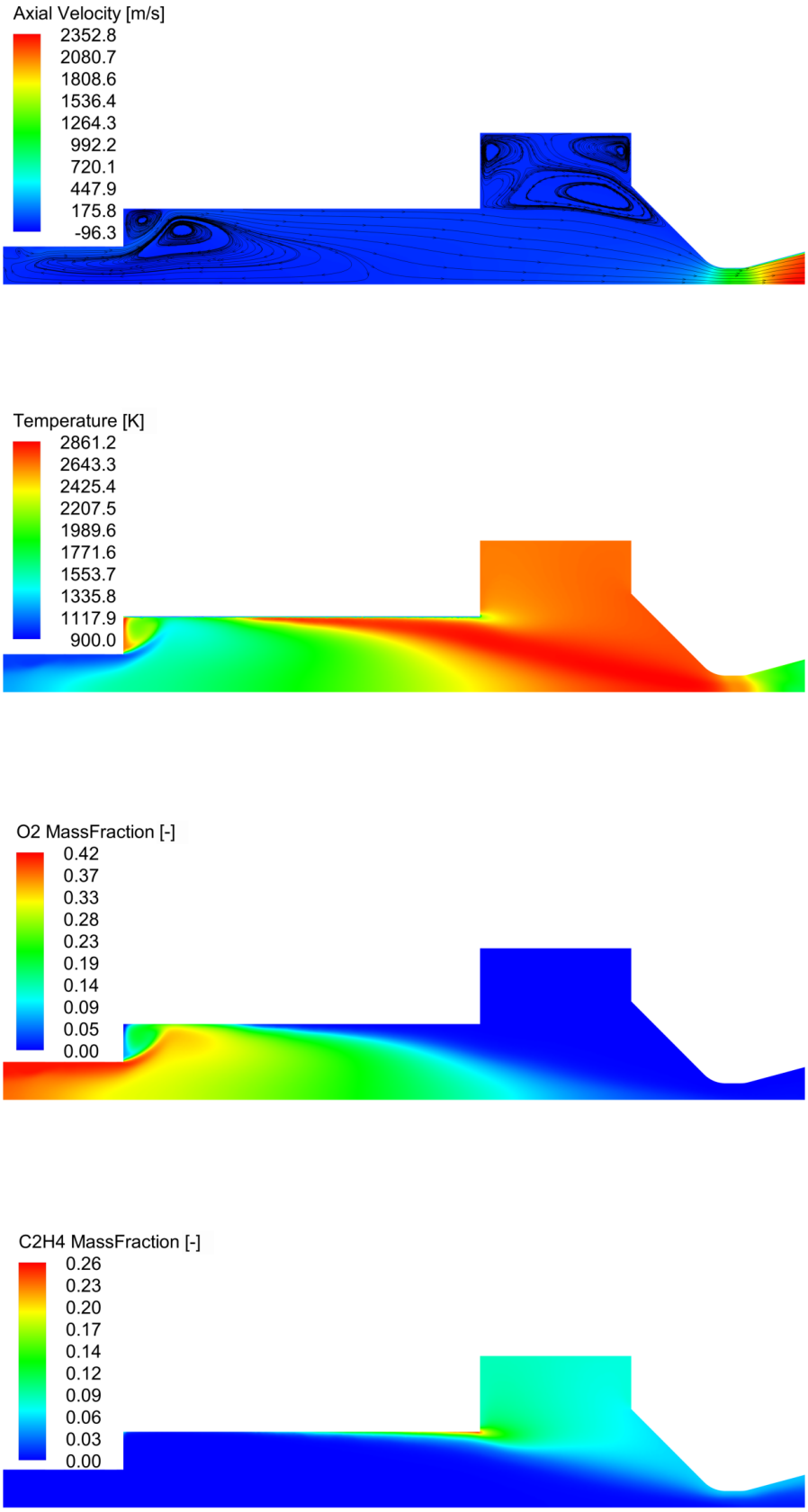

Figure 4.13: Configuration 8 numerical results: contours of velocity, temperature, oxygen and ethylene mass fractions

5 EXPERIMENTAL ACTIVITY

The regression rate and the combustion efficiency of a hybrid rocket motor with swirl oxidizer injection are strongly related to the turbulence intensity created inside the combustion chamber by the injector itself [44, 67, 70, 78, 81, 100, 101, 104]. For this reason, the main objective of the experimental activity that will be presented in this chapter is to understand the effects of the geometric swirl number on the performance of a hybrid rocket motor burning HTP with HDPE.

Moreover, the possibility of tailoring the regression rate based on the actual mission requirements has been investigated. The throttling capability of this configuration has been tested as well, with a real-time deep throttling firing test that uses a flow control valve specifically developed for this purpose by the Hybrid Propulsion Group of the University of Padova [96, 97, 99].

The second motor configuration that has been considered uses an axial injector with HTP and paraffin wax as propellant combination. Unfortunately, paraffin-based fuels have been often regarded with skepticism due to their low melting temperature and softening point. Because these material properties could represent a limitation for specific applications with extended temperature range for long periods, there is often a common misconception on paraffin hybrid motors: the paraffin grain will soften and melt during a long burn. However, according to the liquid layer theory, the heat transfer from the flame is able to melt only a very thin layer near the surface, whereas the rest of the grain should remain at room temperature unless it is heated from other paths [58, 59]. With proper motor thermal insulation, a paraffin grain should be able to withstand a long burn.

Based on this theory, during the experimental activity, the capability of paraffin-based fuels to operate successfully for a long burn without major issues has been proven. To achieve this goal, a laboratory-scale hybrid motor using HTP and paraffin has been tested up to 80 s [87, 102]. To the best of the author's knowledge, this is the longest burn of a paraffin-based hybrid motor ever documented. In order to demonstrate the liquid layer theory, the temperature of the fuel grain has been monitored during the burn.

5.1 TEST BENCH SETUP

The test benches available to the Hybrid Propulsion Group of the University of Padova allow to conduct firing tests of both small-scale and medium-scale hybrid rocket motors, up to a sea-level thrust of

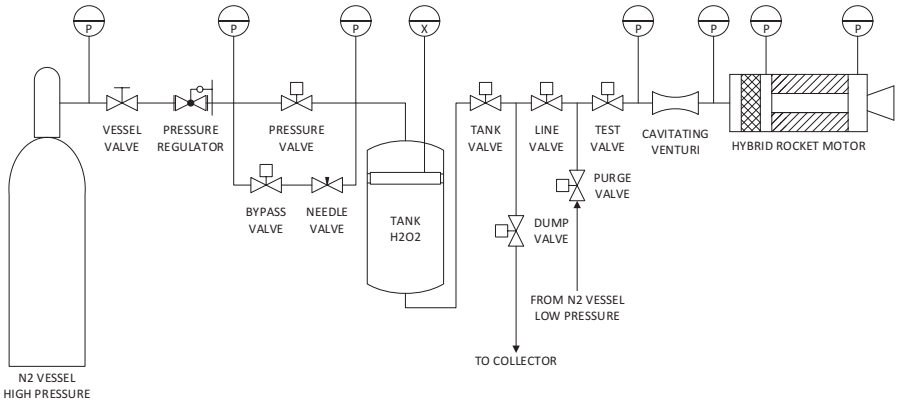

Figure 5.1: P&ID of the test bench setup for small-scale motors

about 10 kN. The experimental setup used for the laboratory-scale motors is the one that interests the following test campaigns and is schematically represented in figure 5.1.

Looking at the detailed P&ID from upstream to downstream, the components of the test bench are a high pressure nitrogen vessel, the pressure regulation block consisting of two pressure regulators connected in series, the oxidizer tank, a series of tubes and automated ball valves connected by double ferrule fittings, the cavitating venturi, and finally the hybrid rocket motor.

The oxidizer tank consists of a cylindrical barrel with two flat bulkheads connected at its ends. Inside the tank two volumes are separated by a piston, where the upper volume hosts the pressurant, while the lower one holds the oxidizer. The impermeability of the piston is granted by a specific dynamic sealing. Connected to the piston, and directed upward, there is a stem that crosses the uppermost bulkhead and is directly linked to a linear potentiometer. Thanks to the potentiometer signal output, both the instantaneous mass flow and the cumulative mass can be determined. This is a good method to measure the mass flow over a wide range of values. Two oxidizer tanks are available for the experiments, one for short burns with a capacity of 4 L, and the other for longer burns with a capacity of 12 L. In order to guarantee the accuracy of the measurements, most of the gas and fluid in the lower volume is vacuum removed before each test and afterwards the tank is filled up, thus reducing the ullage volume during the firing tests.

All the valves in the feed line are ball valves that are operated either manually (on site or from the remote control room), or automatically with an electropneumatic actuator. A remote PLC controller opens and closes each automatic valve, following a predetermined test procedure that depends on the test configuration. The first valve after the high pressure nitrogen vessel is manually operated for safety reasons, to be sure that there cannot be unexpected pressure in the system. The bypass valve is activated before the firing tests to pressurize the oxi-

dizer tank slowly, where the pressurization transient depends on the needle valve opening size. Afterwards, the pressure is maintained constant activating the main pressure valve. The tank valve and the line valve are used as safety redundancy and to divide the feed line in shorter sections for cleaning reasons. The dump valve is used to empty the feed line from the residual oxidizer. The purge valve, instead, allows low pressure nitrogen to flow trough the last part of the line and through the combustion chamber, in order to purge this volume from any residual oxidizer still present at the end of a firing test. The last valve before the hybrid rocket motor is the main valve, which is actuated in order to start or stop the firing test. To ensure full safety during the tests, various rupture disks and relief valves are mounted at different locations inside the tank and along the feed line. In case of unexpected overpressure, the gases are vented to the atmosphere outside of the testing area while the fluids are collected inside an external barrel.

There are five pressure sensors of particular interest placed along the feed line. The first and the second sensor are used to monitor the pressure of the nitrogen vessel and to set the pressure after the regulation block, depending on the test configuration. Another sensor is screwed in the upper bulkhead of the oxidizer tank and hence measures the pressurant pressure. The last two sensors are placed immediately upstream and downstream of the cavitating venturi, to be sure that the oxidizer mass flow is chocked and thus independent of the downstream pressure. Two more sensors are connected to the hybrid rocket motor, one after the catalytic reactor and one in the middle of the post-combustion chamber, which are also used to measure the pressure drop along the swirl injector.

Two thermocouples are placed before and after the catalytic reactor, where the former measures the outflow temperature in order to compensate the density data, while the latter monitors the decomposition efficiency. Moreover, several thermocouples are placed in the external part of the motor case to monitor if there is excessive heating of the structural components or a flame break through.

The hybrid rocket motor is connected to a thick board made of carbon steel using a clamping system. The rigid board has four linear carriages laying on two parallel linear guides, which are connected to the test bench main structure. With this simple configuration, the motor is allowed to move along the axial direction and to transfer its thrust to a button load cell installed on the main structure. The setup just described is shown in figure 5.2.

Before the start of the experimental campaign, a preliminary analysis of the catalytic reactor has been performed. In fact, it is possible to test this section of the hybrid rocket motor in a monopropellant configuration, as it can be seen in figure 5.3. A dedicated nozzle flange has been applied directly downstream of the catalytic reactor, in order to reduce the empty volume and thus the filling time. The

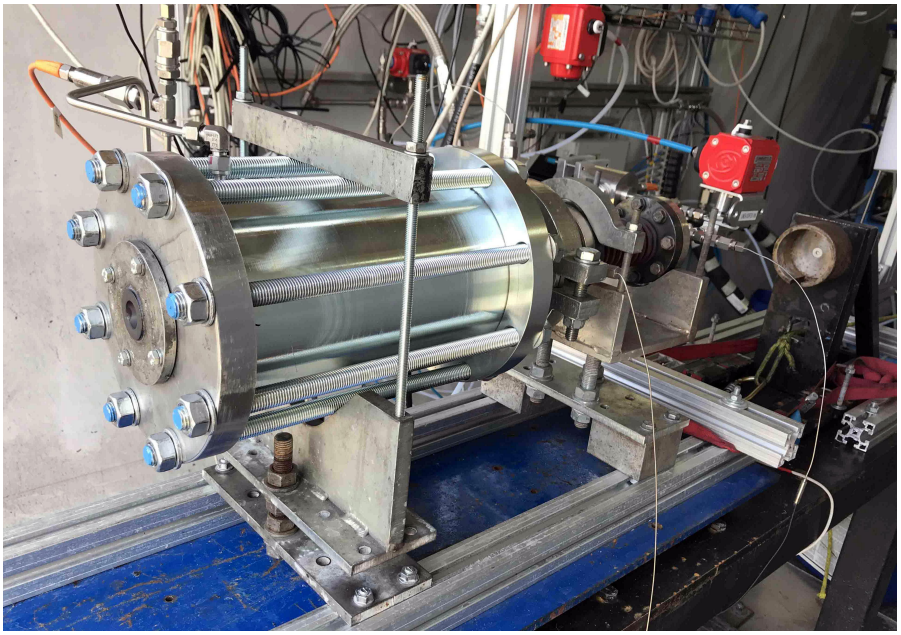

Figure 5.2: Hybrid rocket motor assembled on the test bench

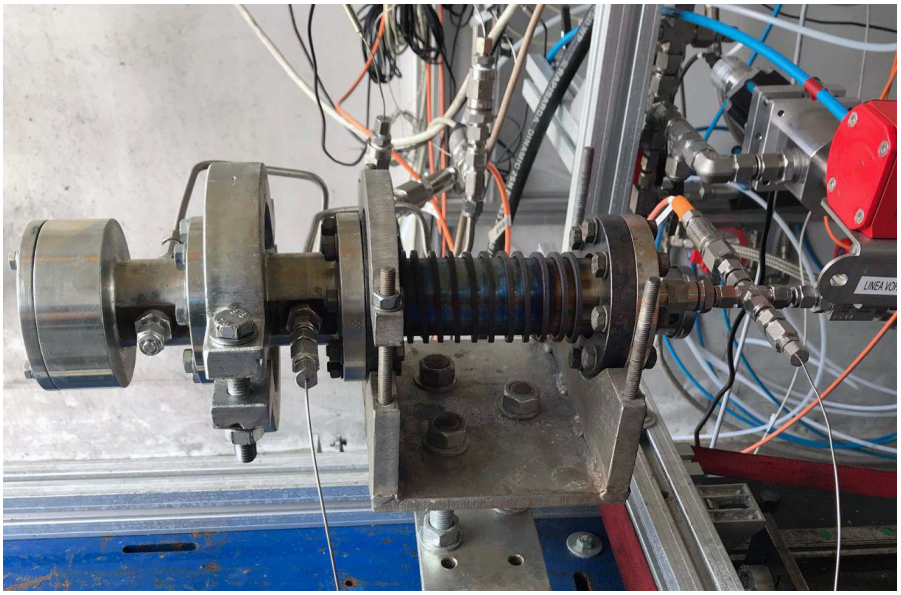

Figure 5.3: Catalytic reactor in the monopropellant configuration

monopropellant tests are aimed to evaluate the suitability and steady state performance of the catalytic decomposition method currently employed, over a wide range of oxidizer mass flows and combustion chamber pressures. The nozzle applied to the monopropellant motor allows to have nearly the same range of operative pressures with respect to the one predicted for the static tests at the same oxidizer mass flow. Moreover, one monopropellant firing has been performed before the first hybrid rocket motor test of each day, in order to exclude the possibility of a malfunctioning of the catalytic reactor.

5.2 SWIRL OXIDIZER INJECTION

The most important part of the test campaign is related to the hybrid rocket motor that has been designed and simulated in chapter 4. For the sake of clarity, this configuration uses swirl injected HTP burning with HDPE. The propellant ignition is spontaneous and an external system is not required, since the oxidizer is decomposed with a catalytic reactor into hot oxygen and water vapor at a temperature of around 1000 K. For the experimental activity, HTP at a concentration of 91.5 % has been used as oxidizer. A mass flow rate of about 100 g/s has been kept constant over the whole experimental activity. Each firing test lasts for 10 s. Moreover, the mixture ratio has been fixed at 6.5 considering only the fuel blowing from the grain surface. This allows to obtain a slightly fuel rich mixture that limits the erosion of the nozzle and the thermal protections, still being able to reach a characteristic velocity close to the maximum value.

In order to decide the test matrix, three different goals have been fixed before starting the experimental activity: comparing different injectors with the same post-combustion chamber; comparing the same injector with different post-combustion chambers; comparing the same motor with different grain port diameters. In order to obtain these results, three main parameters can be varied, namely the injector geometric swirl number, the post-combustion chamber length, and the diameter of the fuel circular port.

Recalling the design process results, three swirl injectors have been available for testing: one with $SN_g = 2$, obtained with ten 5 mm diameter holes, placed on two ranks; one with $SN_g = 2.53$, obtained with ten 4.5 mm diameter holes, placed on two ranks; one with $SN_g = 3.33$, obtained with six 5 mm diameter holes, placed on one rank. The length of the post-combustion chamber, which has a simple cylindrical shape, can be chosen equal to 50 mm, 35 mm or 20 mm.

The grain is considered to maintain its circular shape during the firing test and to burn homogeneously along the length. The instantaneous value of the fuel port diameter can be evaluated integrating numerically the empirical relation (2.34) derived in chapter 2:

$$\dot{r} = aG_{ox}^{n} \tag{5.1}$$

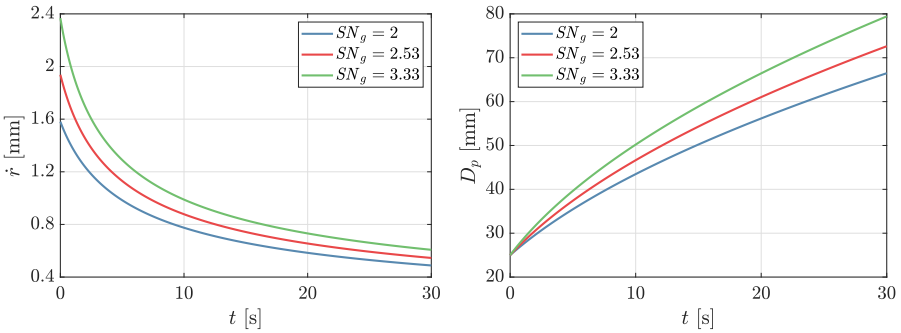

Figure 5.4: Regression rate (left) and port diameter (right) as a function of burning time

where the oxidizer mass flux is equal to:

$$G_{ox} = \frac{\dot{m}_{ox}}{A_p} = \frac{4\dot{m}_{ox}}{\pi D_p^2} \tag{5.2}$$

The dynamic equation of the space averaged port diameter can be written as:

$$\frac{dD_p}{dt} = 2\dot{r} = 2aG_{ox}^n = \frac{2^{2n+1}}{\pi^n} a \frac{\dot{m}_{ox}^n}{D_p^{2n}} \tag{5.3}$$

However, if the oxidizer mass flow rate is kept constant during the burning time, this expression can be integrated to obtain the port diameter as a function of time:

$$D_p(t) = \left[D_{p_0}^{2n+1} + \frac{(2n+1)2^{2n+1}}{\pi^n} a\dot{m}_{ox}^n t \right]^{\frac{1}{2n+1}} \tag{5.4}$$

For HTP burning with a paraffin-based fuel or with HDPE, $n = 0.5$ is a good assumption, as was already demonstrated by several international researchers [79, 112, 113] and confirmed by the Hybrid Propulsion Group of the University of Padova during other test campaigns performed under similar conditions. For what concerns the regression rate constant a, previous experimental results led to preliminary values of this parameter depending on the geometrical swirl number: $a = 0.0886$ for $SN_g = 2$, $a = 0.1086$ for $SN_g = 2.53$, and $a = 0.1327$ for $SN_g = 3.33$ (these values are used to compute the regression rate in mm/s with an oxidizer mass flux measured in kg/m^{2}s). For the present test campaign, the reference initial grain diameter has been fixed equal to 25 mm, which is also the diameter of the outlet section of the swirl injectors. The regression rate and the port diameter as a function of time are represented in figure 5.4 for the three swirl injectors.

Moreover, in order to evaluate the actual regression rate parameters a and n, at least two experimental data at different oxidizer mass fluxes are needed. For this reason, each motor configuration has been

Table 5.1: Test matrix of the experimental campaign

Test	SN_g [-]	L_p [mm]	D_p [mm]	L_{post} [mm]
1	2	170	25	20
2	2	170	25	50
3	2	170	43.5	50
4	2	170	56	50
5	2.53	140	25	20
6	2.53	140	25	35
7	2.53	140	25	50
8	2.53	140	46.5	50
9	2.53	140	61	50
10	3.33	125	25	20
11	3.33	125	25	35
12	3.33	125	25	50
13	3.33	125	50	50
14	3.33	125	66.5	50

tested with three different initial port diameters: the reference initial diameter, the diameter that the grain would have after 10 s of burn, and the diameter that the grain would have after 20 s. It is important to note that the actual value of the circular port diameter after 10 s and 20 s depends on the selected injector.

Finally, the fuel length can be evaluated from the preliminary values of the regression rate for each swirl injector. For a single circular port hybrid rocket motor, the fuel mass flow is equal to:

$$\dot{m}_f = \pi D_p L_p \varrho_f \dot{r} \tag{5.5}$$

Remembering that the mixture ratio is defined as the ratio between the oxidizer mass flow and the fuel mass flow:

$$\varphi = \frac{\dot{m}_{ox}}{\dot{m}_f} \tag{5.6}$$

with some substitutions the length of the fuel grain can be computed with the following relation:

$$L_p = \frac{\pi^{n-1} D_p^{2n-1} \dot{m}_{ox}^{1-n}}{4^n a \varphi \varrho_f} \tag{5.7}$$

The actual lengths of the solid grains are not exactly the same as the ones computed in chapter 4 due to manufacturing reasons.

The complete test matrix of this experimental investigation is summarized in table 5.1, where the fundamental geometrical dimensions are reported as well.

A typical firing test is shown in figure 5.5, where the shock diamonds over the flame length can be appreciated. The typical experimental data, measured during both the monopropellant tests and the

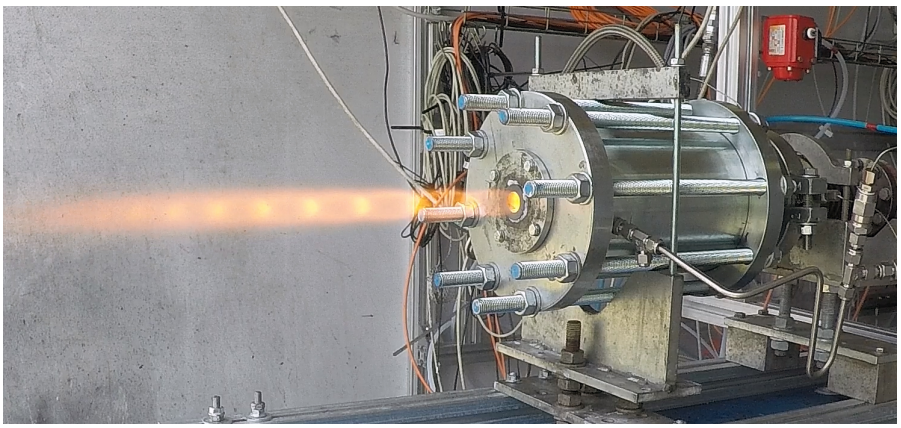

Figure 5.5: Typical firing test of a hybrid rocket motor with swirl injection

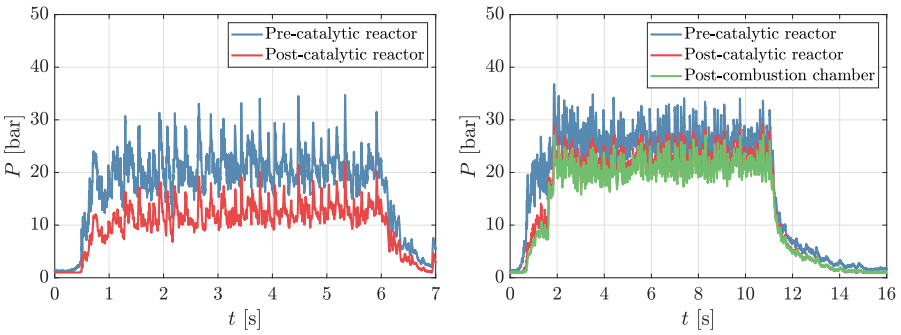

Figure 5.6: Pressure of a monopropellant (left) and a bipropellant (right) test

bipropellant tests, are shown in figure 5.6 and 5.7. Thanks to three pressure sensors, placed immediately before and after the catalytic reactor and in the post-combustion chamber, it is possible to evaluate the pressure drop along the catalytic reactor and the one across the swirl injector. The pressure drop along the injection plate is always around 1 bar, where the higher the geometric swirl number the slightly higher the pressure drop. It is important to underline that the pressure oscillations inside the hybrid rocket motor, which can be as high as $\pm 25\,\%$, do not depend on an unstable combustion process nor on a bad design of the combustion chamber. Instead, the pressure noise is entirely caused by the catalytic reactor used during this test campaign, as it is possible to understand looking at the pressure profile of a monopropellant test. For future firing tests, the catalytic reactor will be entirely redesigned, based on a new catalytic material and on a larger decomposition volume. As it will be seen later in this chapter, this redesign will be able to lower the pressure oscillations to an acceptable value of $\pm 5\,\%$. However, despite the pressure oscillations, the combustion chamber pressure is constant over the burning time. The same can be said for the oxidizer mass flow rate, confirming the preliminary assumption that $n = 0.5$ for a hybrid rocket motor burning HTP with a HDPE fuel grain.

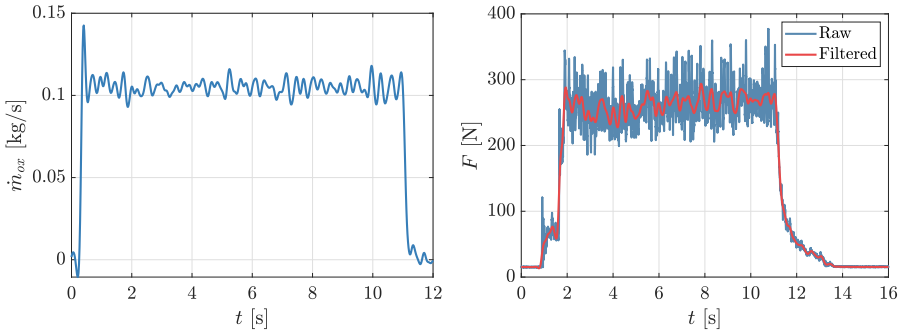

Figure 5.7: Oxidizer mass flow rate (left) and thrust (right) of a firing test

Figure 5.8: Helical pattern inside the paraffin grain port

The characteristic helical pattern given by the swirl injection, which forces the oxidizer mass flow to enter the combustion chamber with a strong tangential velocity component, leaves an imprint on the internal surface of the grain. The marks are clearly visible in figure 5.8.

Before analyzing the performance of all the configurations tested, it is important to make some considerations about the propellants mass flow rates. All these information are summarized in table 5.2. The oxidizer mass flow rate is almost equal to the target one of 100 g/s and the mixture ratio calculated considering only the fuel grain is really close to the design one, where the average value of all the firing tests is around $\varphi_{gr} = 6.6$. However, during the design phase of the hybrid rocket motor, only the fuel mass flow rate blowing from the grain surface has been considered. To compare the influence of the other components of the combustion chamber, the contribution to the total fuel mass flow rate of a single component must be introduced. For example, for the solid grain this parameter is defined as:

$$\varepsilon_{gr} = \frac{\dot{m}_{f_{gr}}}{\dot{m}_{f_{tot}}} \tag{5.8}$$

Table 5.2: Fuel mass flow contribution of each motor component

Test	$\dot{m}_{ox}$ [g/s]	φ [-]	φ_{gr} [-]	ε_{gr} [%]	ε_{post} [%]	ε_{cpf} [%]
1	0.1022	4.82	5.75	83.77	6.81	9.42
2	0.1065	4.00	6.09	65.61	21.74	12.65
3	0.1027	4.50	6.09	73.91	18.84	7.25
4	0.1043	4.44	5.93	74.77	16.51	8.72
5	0.1038	5.54	7.10	78.03	9.25	12.72
6	0.1052	5.76	8.20	70.24	16.07	13.69
7	0.1031	4.48	7.03	63.76	27.98	8.26
8	0.1039	4.90	7.14	68.56	22.16	9.28
9	0.1017	4.46	6.32	70.56	19.16	10.28
10	0.1045	5.34	6.62	80.66	8.29	11.05
11	0.1049	4.88	6.64	73.50	17.00	9.50
12	0.1029	4.10	6.26	65.52	25.00	9.48
13	0.1031	4.19	6.42	65.24	22.74	12.02
14	0.1053	4.24	6.41	66.24	21.37	12.39

where the fuel mass flow of each component is evaluated from its weighted mass loss divided by the burning time. The contribution of the post-combustion chamber ε_{post} can be higher than 25 % and this is the reason for the very low values of the overall mixture ratio. On the other hand, the contribution of the two cotton-phenolic flanges is around 10 %, value that is acceptable considering the trade-off between the material properties and cost.

As introduced in chapter 4, two different characteristic velocities can be computed:

$$c^{\star}_{ex_P} = \frac{P_{cc} A_t}{\dot{m}_{tot}} \tag{5.9}$$

$$c^{\star}_{ex_F} = \frac{F}{\dot{m}_{tot} C_F} \tag{5.10}$$

and consequently two different motor efficiencies:

$$\eta_P = \frac{c^{\star}_{ex_P}}{c^{\star}_{th}} \tag{5.11}$$

$$\eta_F = \frac{c^{\star}_{ex_F}}{c^{\star}_{th}} \tag{5.12}$$

In order to compute the theoretical characteristic velocity, the mass flow coming from the consumption of the two cotton-phenolic flanges has been considered as gasified HDPE. The reason is that it is complicated to model the decomposing cotton-phenolic composite material, because it creates char while burning, and it is out of the scope of this test campaign. This assumption is on the safe side because the characteristic velocity of the cotton-phenolic is lower compared to the

Table 5.3: Experimental results of the test campaign

Test	$\dot{m}_{ox}$ [g/s]	φ [-]	P_{cc} [bar]	F [N]	η_P [%]	η_F [%]
1	0.1022	4.82	20.1	261.8	95.7	97.4
2	0.1065	4.00	21.4	274.5	98.7	97.2
3	0.1027	4.50	20.6	253.7	97.6	93.6
4	0.1043	4.44	20.2	257.1	93.8	93.7
5	0.1038	5.54	20.8	259.7	98.4	95.1
6	0.1052	5.76	20.3	261.2	94.9	94.7
7	0.1031	4.48	20.7	266.9	97.7	98.1
8	0.1039	4.90	18.8	232.9	88.3	86.0
9	0.1017	4.46	20.4	254.5	97.8	95.0
10	0.1045	5.34	21.1	261.9	97.9	95.0
11	0.1049	4.88	21.1	262.9	98.1	94.8
12	0.1029	4.10	20.9	261.2	98.5	96.1
13	0.1031	4.19	21.0	259.5	98.9	95.2
14	0.1053	4.24	20.6	259.2	95.0	93.3

one of the HDPE. Moreover, the contribution of the two cotton-phenolic flanges to the total fuel mass flow is relatively small.

From the experimental results presented in table 5.3, it is possible to see that all the analyzed configurations have a very high efficiency, except for configuration 8. This is imputable to an anomalous gas leakage in the motor, because the fuel regression rate is in line with the other firing tests and no major problems with the injection plate or the graphite nozzle have been found. Unfortunately, in order to keep the cost of the experimental activity low and due to the short amount of time available, no repeatability tests have been performed. Moreover, configurations 1 and 7 exhibit a thrust efficiency higher than the pressure efficiency, probably imputable to some measurement errors and a throat erosion effect.

As opposed to the numerical results, the values of the two expressions of motor efficiency are very close one to the other. This means that the reduction of the effective throat area caused by the swirling flow is not as significant as expected from the numerical simulations. The reason probably lies in the fact that the post-combustion chamber has been simulated as an adiabatic wall, thus neglecting the fuel coming from the ablating surface. However, the results of the firing tests suggest that this contribution is significant. The mass flow that is injected in this area of the motor reasonably reduces the swirl number, both due to the mass addition and to the increased chemical reactions. Consequently, a lower swirl number results in a smaller effective throat area reduction.

Looking at the motor performance of all the configurations, summarized in table 5.3, it is possible to recognize the same trends that have been found during the numerical investigation of chapter 4. First and

most important, even the configuration with the smaller geometric swirl number and the shorter post-combustion chamber has a high efficiency. For this reason, it is hard to see a significant trend of the efficiency that should increase with the geometric swirl number and with the post-combustion chamber length. However, this important result leads to the conclusion that in this type of hybrid rocket motor a post-combustion chamber is not really needed, and for this reason this component will be removed for the next experimental activity. On the other hand, the effect of the grain port diameter is clearly visible: the efficiency decreases with a larger initial port diameter because, as it has been found with the numerical analysis, the mixing in the post-combustion chamber is less effective when the difference in diameters between this section and the grain port is smaller.

Thanks to the large amount of experimental tests, where the same motor configuration has been fired with three different initial grain diameters, it is possible to calculate the regression rate coefficients a and n. First, the space-time averaged form of the regression rate is evaluated from the measurement of the burned fuel mass. It is not possible to measure the regression rate directly from the variation of the port diameter, because the consumption is uneven along the grain axis, mainly at the head-end side due to injection phenomena. Defining the measurement before and after the firing test with the subscripts 1 and 2, the regression rate can be computed as:

$$\Delta M_f = M_{f_1} - M_{f_2} \tag{5.13}$$

$$M_f = \varrho_f \pi \frac{D_p^2}{4} L_p \tag{5.14}$$

$$D_{p_2} = \sqrt{D_{p_1}^2 - \frac{4\Delta M_f}{\varrho_f \pi L_P}} \tag{5.15}$$

$$\dot{r} = \frac{D_{p_2} - D_{p_1}}{2t_b} \tag{5.16}$$

Unfortunately, the grain port surface is not the only one that blows fuel during the burning time. Also the grain lateral face on the post-combustion chamber side is consumed, due to the strong flow recirculation in this region. In order to remove the face contribution to the grain fuel mass flow, some more geometrical measurements of this area have been taken. This process allows to evaluate the regression rate of the grain port alone. Afterwards, the average grain port area and consequently the average oxidizer mass flux can be computed:

$$A_{p_{avg}} = \frac{\pi}{2} \frac{D_{p_1}^2 + D_{p_2}^2}{4} \tag{5.17}$$

$$G_{ox_{avg}} = \frac{\dot{m}_{ox}}{A_{p_{avg}}} \tag{5.18}$$

Finally, it is possible to calculate the values of the regression rate coefficients for each swirl injector, which are summarized in table 5.4.

Table 5.4: Regression rate coefficients for the three swirl injectors

SN_g	a	n
2	0.0665	0.511
2.53	0.0855	0.491
3.33	0.0976	0.506

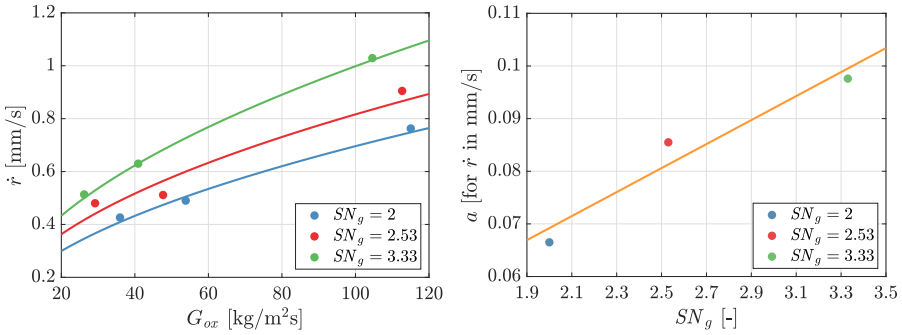

Figure 5.9: Regression rate numerical fit (left) and correlation between the geometric swirl number and the coefficient a (right)

These values are retrieved with a numerical fit of the experimental results of the three tests with different initial port diameters, as it can be seen in figure 5.9. The experimental results definitively confirm that the regression rate exponent n is practically equal to 0.5, where the small deviations are due to measurement errors and to the high sensitivity of the regression rate coefficients to the firing time and the burned mass estimation. Moreover, it is now possible to find a correlation between the geometric swirl number and the regression rate coefficient a. The numerical fit, which is shown in figure 5.9, can be expressed as:

$$a = 0.0228 SN_g + 0.0236 \tag{5.19}$$

Since the regression rate coefficient a has a dependency on the geometric swirl number, it is possible to tailor the regression rate just changing the swirl injector and thus the swirling flow intensity, based on the specific mission requirements. Moreover, the correlation that has been found is a simple linear law, at least across the small range that has been analyzed.

It is crucial to emphasize the importance of fuel regression rate tailoring for space applications. As it is possible to understand following the mathematical treatment of chapter 3, where some simple analytical relations for the system design of a hybrid rocket motor have been derived, the packaging of the hybrid propulsion system is not very flexible and is strongly related to the sizing of the combustion chamber, which in turn depends on parameters like the fuel regression

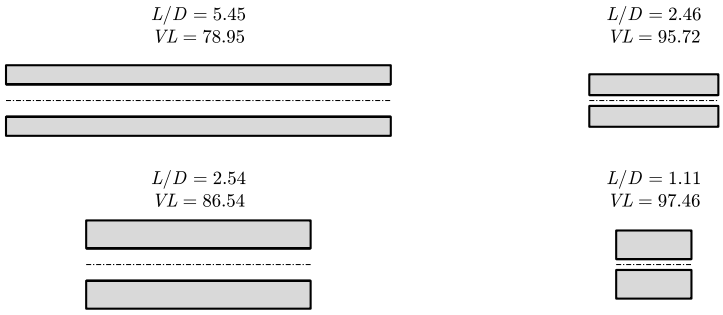

Figure 5.10: Grain shapes for first case (left) and second case (right), with $a = 0.07$ (top) and $a = 0.12$ (bottom)

rate, the burning time and the total mass of propellant required for a specific mission.

In order to show the impact of fuel regression rate on the sizing of the propulsion system, two design examples of a hybrid motor with a single circular port are presented, based on typical applications like the ones reported in chapter 1. The first case is in line with motors designed for ascend vehicles [9, 31], whereas the second case refers to a hypothetical low thrust motor for space applications [39]. The mission profile fixes the burning time and the propellant mass of the propulsion system. The first case is characterized by $M_p = 80\,\text{kg}$ and $t_b = 40\,\text{s}$, whereas for the second case $M_p = 18\,\text{kg}$ and $t_b = 80\,\text{s}$ are considered. The propellant combination selected for both cases is HTP as oxidizer and HDPE as fuel, at a mixture ratio of 7.

For sake of simplicity, the oxidizer mass flow rate is taken as constant and the value of the regression rate exponent n is fixed equal to 0.5, in order to avoid any mixture ratio shift with time. The initial oxidizer mass flux is chosen equal to $500\,\text{kg/m}^2\text{s}$. Each of the two examples is investigated with two different values of the regression rate constant, namely $a = 0.07$ and $a = 0.12$ (these values are used to compute the regression rate in mm/s with an oxidizer mass flux measured in $\text{kg/m}^2\text{s}$). The different values of the regression rate constant are chosen in order to simulate two different swirl intensities of the injection plate.

The results of the grain shapes for the two design examples are shown in figures 5.10. It is finally possible to understand the importance of regression rate tailoring: for a mission with a high propellant mass and a short burning time (like in the first case) it is better to have a configuration with a fast regression rate in order to improve the volume loading and shorten the motor; on the other hand, for a mission that requires a long burning time and a small amount of propellant (like in the second case), the choice of an injection pattern that gives a high regression rate may not be the best solution, because the improvement of the grain volume loading becomes negligible while the grain becomes too short compared to its diameter.

5.3 REAL-TIME THROTTLING

Throttleability is a prized feature in rockets motors because it allows to perform peculiar mission profiles, such as soft landing. Hybrid rocket propulsion is a throttling capable technology, but this quality is often ignored in current research works. The only way to achieve deep throttling in hybrid rocket motors is to control the oxidizer mass flow that is injected into the combustion chamber. In order to do so, a flow control valve is required and the one used in this experimental study is based on a variable area cavitating venturi. Variable area cavitating venturis are a particular class of control valves in which the operating fluid reaches the saturation pressure at the throat of the venturi and hence it cavitates. The vapor that forms at the throat limits the flow through the venturi, which in the case of chocked flow is equal to:

$$\dot{m} = C_D A_t \sqrt{2\varrho\left(P_{0_{up}} - P_{sat}\right)} \tag{5.20}$$

It is important to note that when the flow is chocked the oxidizer mass flow is independent of the downstream pressure. For cavitating venturis in general this is true if the back pressure does not reach a certain limit. In the event that this limit is reached, the cavitation at the throat is drastically reduced or stopped and the flow becomes related to the back pressure. Many researches reported a maximum allowed back pressure ratio of 0.8 to 0.9 [91, 111]. The independency of the oxidizer mass flow from the downstream pressure is an important feature of this class of flow control valves, mainly for two reasons. First, it is possible to mitigate the feed system instabilities since the oxidizer tank and the combustion chamber environment are uncoupled. Second, without a dependency of the flow on the downstream pressure and considering a constant upstream pressure, the flow has a direct linear dependency on the throat area.

The variable area cavitating venturi, which is used as flow control valve in the experimental test bench, has been specifically developed by the Hybrid Propulsion Group of the University of Padova. It has been characterized thoroughly and four types of characterization have been performed: static, dynamic, maximum allowed back pressure and cavitation instabilities [96–99]. The valve has been designed to operate with a flow range between 30 g/s and 340 g/s and a maximum operating pressure of 80 bar.

The flow control valve is composed of two parts, the valve main body and the actuation, as it can be seen from the sagittal section of the device represented in figure 5.11. Moreover, figure 5.12 shows the flow control valve model and its integration in the feed line.

The valve consists of a conical shaped pintle that enters into the venturi throat. This motion is achieved using a leadscrew that guarantees a precise alignment and position of the pintle. A venting hole is machined in the main body (between the sealing and the leadscrew)

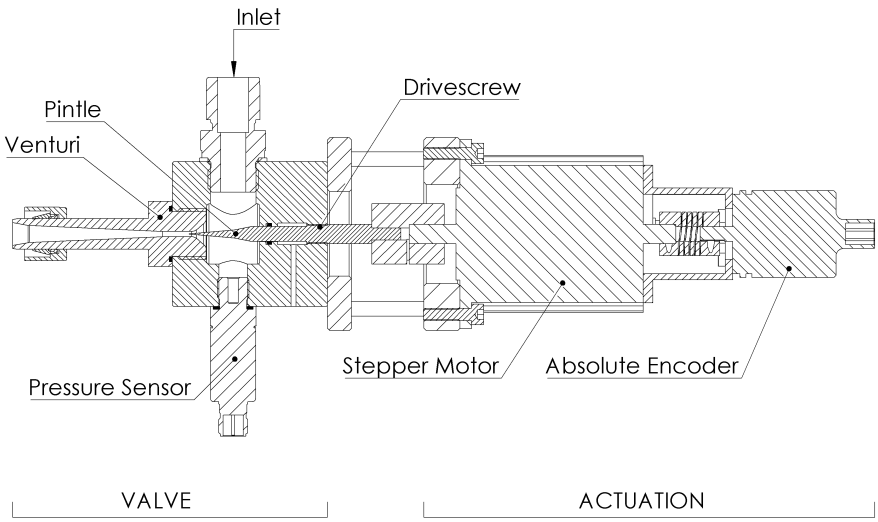

Figure 5.11: Sagittal section of the flow control valve

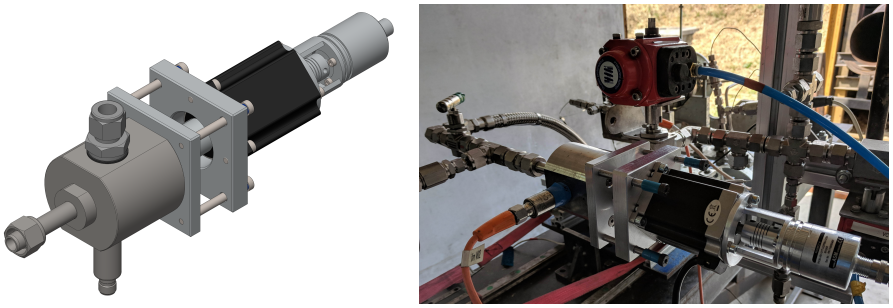

Figure 5.12: CAD model of the flow control valve (left) and integration in the feed line during its characterization (right)

to relief the pressure caused by a movement of the pintle. An O-ring sealing is used to separate the wet region of the flow control valve from the leadscrew. This sealing configuration allows to use any type of lubricant in the leadscrew even those that are not strictly Class A compatible with HTP. The venturi is connected to the main body with a precise threaded connection. Here the sealing is granted by an O-ring in a groove at the base of the male thread. At the downstream end of the venturi a double ferule connection is used to join the flow control valve to the rest of the feed line. As it can be seen in figure 5.11 and 5.12, the flow enters with a 90° angle with respect to the downstream exit, which is collinear to the pintle axis. On the opposite side of the valve inlet there is a pressure transducer that is used to measure the instantaneous upstream pressure.

The actuation consists of a stepper motor connected with an absolute encoder. The stepper motor is dual shaft and two phase. The back shaft is used to connect the motor with the encoder, using a flexible joint. The angular encoder is based on Hall effect and allows to have an absolute measure of the shaft angle. Motor and encoder are connected

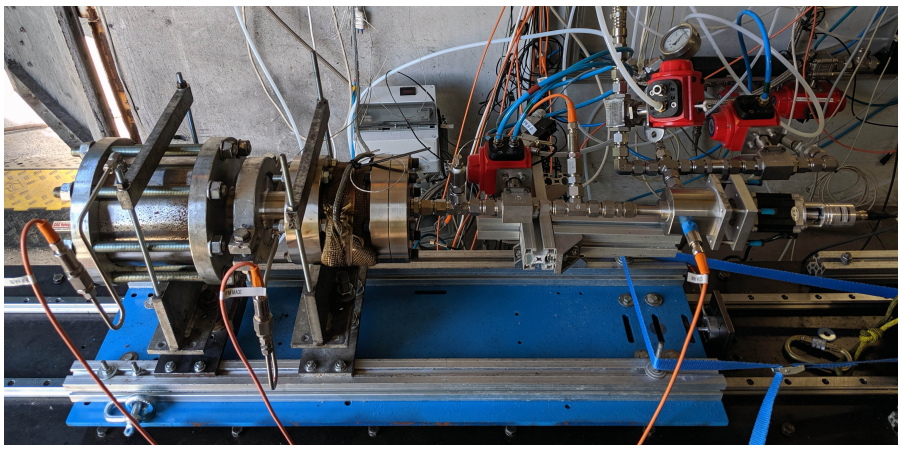

Figure 5.13: Experimental setup of the hybrid rocket motor throttling test

with an aluminum flange. For what concerns the connection between the actuation and the valve, the front shaft of the stepper motor is coupled with the pintle using a rigid joint. Stepper motor and valve main body are connected using four rectified bolts that allow the motion of the actuation system along the pintle axis while blocking any kind of torque and bending.

The experimental setup used to exploit the throttling capabilities of the swirl injection hybrid rocket motor has not been changed, except for the flow control valve and the catalytic reactor, as shown in figure 5.13. The fixed area cavitating venturi has been replaced with the variable area cavitating venturi, while the catalytic reactor has been substituted with a system that uses a new catalytic material and has a bigger chamber volume. The modifications of the catalytic reactor have been introduced in order to reduce the pressure oscillations during the firing tests, which have been found with the previous experimental campaign and that are caused by the catalytic decomposition behavior.

Four tests have been performed to complete the experimental analysis of the swirl injection hybrid rocket motor: three sinusoidal wave tests with a frequency of 0.1, 0.2 and 0.3 Hz respectively, and a step test. In figure 5.14, 5.15, 5.16 and 5.17, the measured pressure plots and the measured thrust profiles for the three sinusoidal wave throttling tests and the step throttling test are reported.

During the sinusoidal wave tests the feed oxidizer mass flow ranged from 30 g/s to 340 g/s and the hybrid motors have been ignited with an oxidizer mass flow of 180 g/s. The tests lasted for thirteen seconds, where three seconds have been allowed for ignition, while the throttling sequence lasted for the remaining ten seconds. Since the length of the throttling sequence has been kept constant for every test, the number of waves changes from test to test. From the plots in figure 5.14, 5.15 and 5.16, it is possible to note that the pressure drop on the catalytic reactor is about 4 bar at full oxidizer mass flow, while the previous catalytic reactor had a much higher pressure drop. This

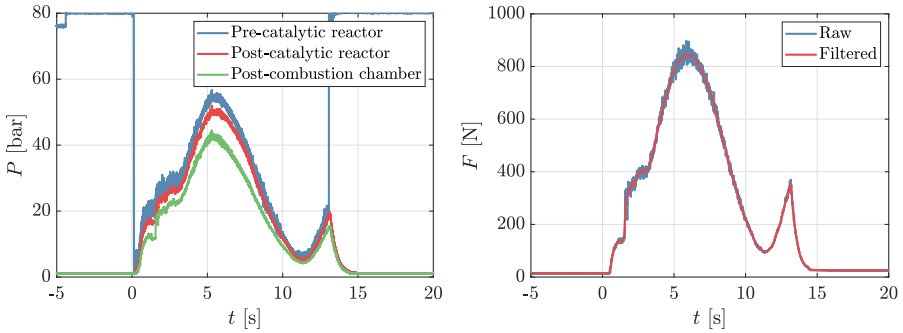

Figure 5.14: Pressure (left) and thrust (right) of the 0.1 Hz test

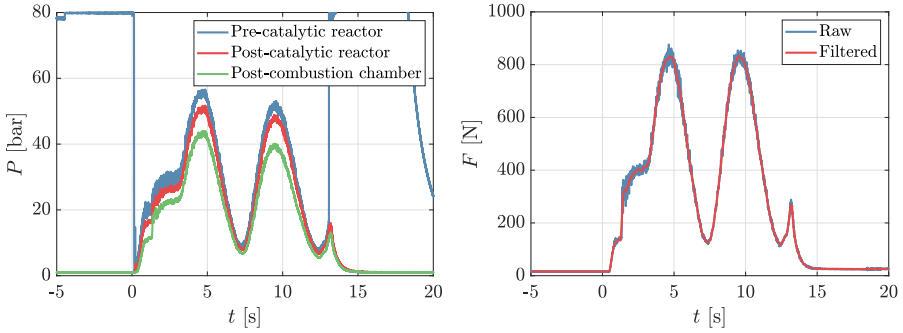

Figure 5.15: Pressure (left) and thrust (right) of the 0.2 Hz test

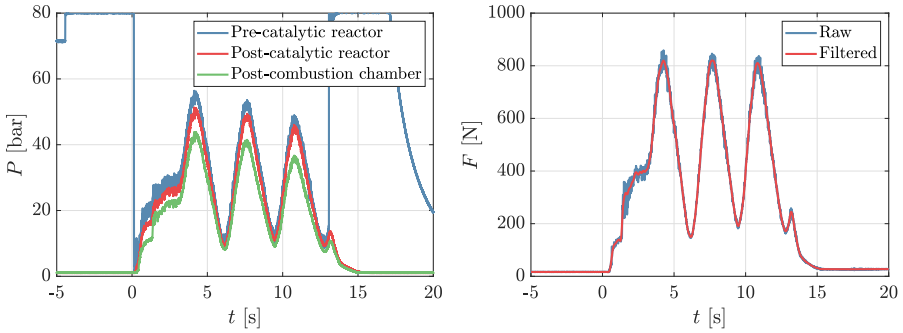

Figure 5.16: Pressure (left) and thrust (right) of the 0.3 Hz test

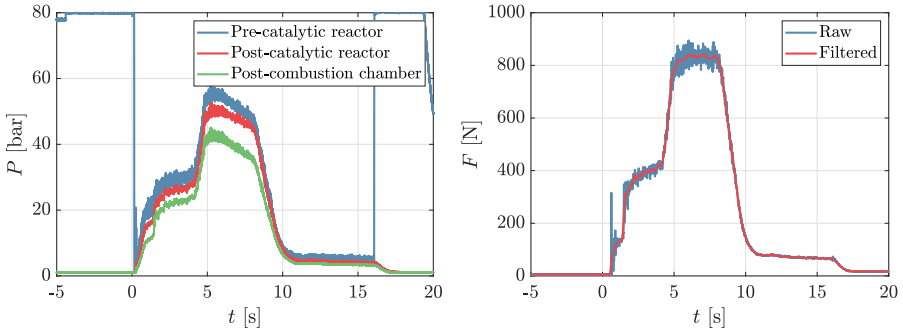

Figure 5.17: Pressure (left) and thrust (right) of the step test

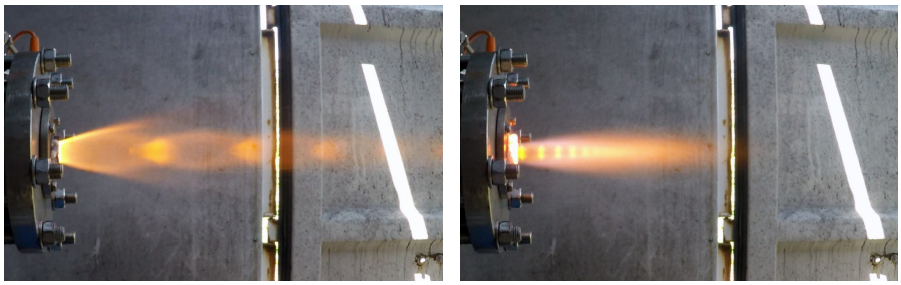

Figure 5.18: Oxidizer rich underexpanded flame at high thrust (left) and fuel rich overexpanded flame at low thrust (right)

effect has been obtained increasing the cross-section of the reactor and changing the catalyst material. Another thing that can be noted is the behavior of the motor at the very low oxidizer mass flow. Considering the 0.1 Hz test, the HTP decomposition and the combustion process are smooth, even for a combustion chamber pressures as low as 4.2 bar and a correspondent catalyst reactor pressure of 5.2 bar. During ignition such a low pressure can be problematic, but after ignition and during throttling the catalyst reactor and the overall motor behavior are very stable. If the thrust and the pressure profiles are compared, the effect of the throat erosion can be observed: from wave to wave the combustion chamber pressure decreases while the thrust profile is nearly constant during the burning time.

The step test has been ignited at 180 g/s, then after four seconds the oxidizer mass flow has been increased to 340 g/s for four seconds and eventually lowered to 30 g/s for six seconds. During the test a maximum thrust of 841.3 N and a minimum thrust of 66.8 N have been achieved, leading to a throttling ratio of 12.6. From the plots in figure 5.17 it is again possible to observe the stable motor behavior for low and high thrusts and the reduced pressure drop achieved with the new catalytic reactor. The effects of throat erosion are evident on the higher step, where there is a pressure drop from 42 bar to 37 bar when the oxidizer mass flow is kept constant and equal to the maximum value. However, the thrust is nearly constant. Due to the excessive throat erosion, a combustion chamber pressure of 3.4 bar is reached with a catalytic reactor pressure of 4.5 bar. Figure 5.18 shows the plume comparison between the maximum and the minimum thrust.

A real-time throttling test has been performed to complete the work carried out until now and to demonstrate the robustness of the control loop applied to the hybrid rocket motor. During this test the oxidizer mass flow injected into the combustion chamber has not been controlled by a predetermined program sequence but by means of a manual throttle. The throttle consists of a simple linear potentiometer with a knob attached. The variation of the potentiometer position results in a variation of a voltage signal that is read by the pintle control system. The signal coming from the throttle is used to directly

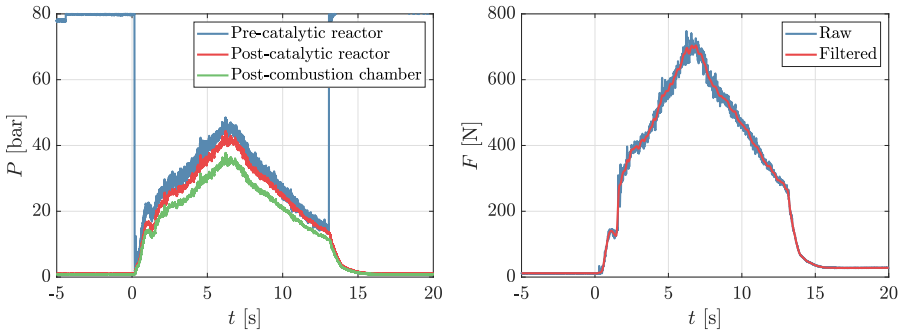

Figure 5.19: Pressure (left) and thrust (right) of the manual test

control the pintle position that in turns results in a control of the inlet oxidizer flow. The minimum oxidizer mass flow that can be set by the user is 30 g/s while the maximum one is 340 g/s. This range corresponds to the one previously used in the predetermined throttling fire tests. In case of a signal loss between the throttle and the pintle control system, the maximum pintle stroke is limited mechanically by means of four rigid plastic tubes that are co-axially connected to the four rectified bolts of the flow control valve actuation. One single manual throttling test has been performed and the measured results are reported in figure 5.19. The thrust profile achieved during manual throttling resembles a pyramid, with an average thrust higher than the one of the predetermined throttling tests performed before. From the plot it can be observed that both the combustion chamber pressure and the thrust are very stable.

5.4 LONG BURNING TIME

The second motor configuration that has been analyzed uses an axial injector with HTP and a paraffin-based fuel as propellant combination. The Hybrid Propulsion Group of the University of Padova has been working for a long time with this configuration of hybrid rocket motors, gaining great experience on the design process.

The objective of the firing test is twofold [87, 102]: first, to demonstrate the feasibility of the HTP and paraffin hybrid rocket motor for long burning times; and second, to demonstrate paraffin liquid layer behavior. To achieve these goals, a specific motor setup has been implemented. This setup has been designed in order to properly survive the severe thermal loads of such prolonged combustion and to allow the measurement of the temperature in the paraffin grain at different locations during the burning time. The test directly demonstrates the feasibility of a small HTP and paraffin motor with a substantial long burn. Considering that thermal and erosion issues are more significant at small scales, the test indirectly demonstrates the feasibility of the technology also for larger scales motors.

In this configuration, the hot oxidant flow enters the combustion chamber from the inlet flange and impinges on the grain surface, igniting the paraffin grain. The thermal protections also take part in the combustion process, providing the necessary ablative cooling capability, which prevents the metal casing from overheating. There are mainly two heat paths to the metal casing: the first is through the inlet catalytic flange, where the metal sees a temperature of about 1000 K; the second is through the nozzle, and it is more dangerous, not only because the flow temperature is beyond 2000 K but also because the maximum heat transfer from the flow to the walls occurs at the nozzle throat, as it is known from basic gas dynamics. For this reason, the possibility of introducing an insulating material between the graphite nozzle and the metal casing has been taken into consideration during the design phase. However, a good insulation tends to increase the graphite nozzle operating temperature, thus leading to an increase of the nozzle throat erosion phenomena typically occurring in long burning time tests. This in turn translates into a decreasing pressure profile, instead of a constant one. Therefore, it has been decided to give prior importance to stable pressure conditions, and thus no insulating material has been used around the graphite nozzle.

The outside casing temperature has been measured at the beginning and at the end of the combustion chamber. Moreover, the temperature in the nozzle region on the outlet flange has been carefully monitored, because no insulation of the graphite nozzle has been employed. Two additional thermocouples have been inserted inside the paraffin grain, at a depth of 10 mm from the grain external diameter. Their duty was to monitor eventual temperature variations inside the grain during the whole burning time.

During the firing test, the mass flow has been reduced to about 53 g/s in order to have the possibility of testing the long burn capabilities of HTP and paraffin motors at a small scale. In fact, a higher mass flow would increase the consumption of the fuel too much, leading to a full grain depletion well before the end of the test. Moreover, a reduced oxidizer mass flow is able to decrease the erosion rate of the nozzle, which will help to maintain a constant value of the combustion chamber pressure during the whole firing test.

The long burning time test has been completed successfully: no particular issues nor combustion instabilities are reported. First of all, the oxidizer mass flow measured by the potentiometer is presented in figure 5.20. The use of the cavitating venturi ensures an approximately constant oxidizer mass flow, and the small oscillations are only related to the process of filtering the noise of the potentiometer measurement. The most important performance parameter for the test is the chamber pressure, which is shown in figure 5.20. The constant trend of the plot of both pre- and post-combustion chamber pressures demonstrates that the HTP and paraffin hybrid motor is suitable to be used for long burning times, eliminating any doubt related to the

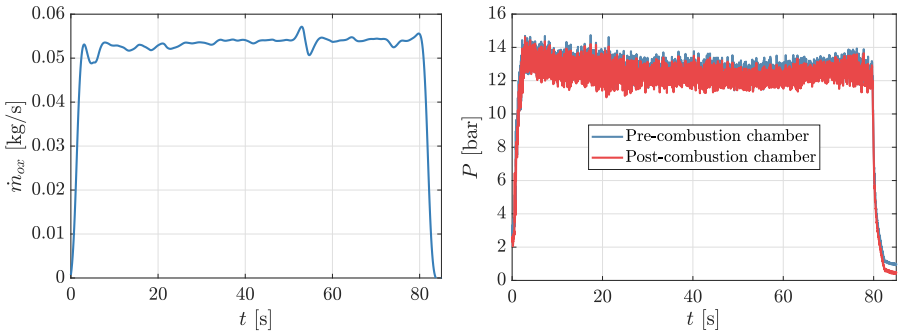

Figure 5.20: Oxidizer mass flow (left) and pressure (right) of the long burning time test

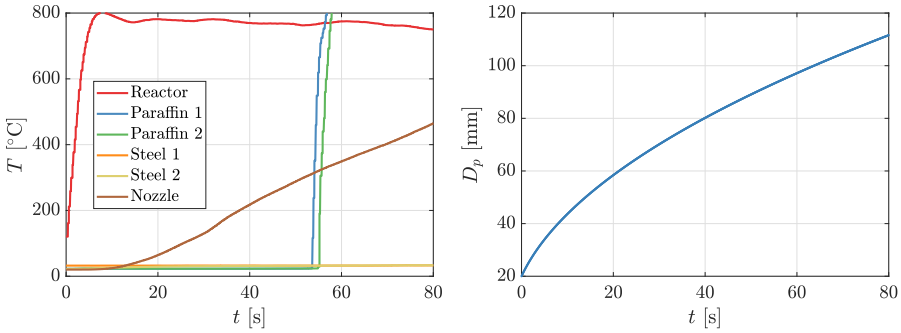

Figure 5.21: Temperature (left) and theoretical port diameter (right) of the long burning time test

use of a paraffin grain for typical applications. Moreover, the pressure oscillations, which can be reduced with an optimization of the combustion chamber design, are currently less than 10 %, providing a stable and efficient combustion. Two other conclusions can be derived from the experimental data. First, the fuel rich mixture ratio prevents the erosion of the nozzle throat, and the throat diameter measured at the end of the burn confirms the pressure data. Second, assuming a constant value of the characteristic velocity during the burn and because the oxidizer mass flow is held constant, the experiment confirms once again that the regression rate exponent n is equal to 0.5 for the paraffin-based fuel. This also leads to the conclusion that the mixture ratio remains unchanged along the entire burning time.

At the end of the burn, only a little paraffin residual has been found and the final weight measurements have been taken in order to determine the paraffin regression rate. Subsequent post-processing leads to the derivation of the regression rate constant value, which is found to be $a = 0.145$ (this value is used to compute the regression rate in mm/s with an oxidizer mass flux measured in kg/m^{2}s).

Figure 5.21 shows the temperature variation during the burning time for different points of interest. The two thermocouples inside the paraffin, which have been placed 10 mm into the grain, measure

an almost constant temperature (the same as the initial one) until a steep increase is detected after about 55 s. Here the sensors are exposed directly to the flame, and failure of the thermocouples (which is expected) occurs. On the other hand, both the thermocouples on the outer side of the metal casing experience a negligible temperature variation, confirming that the external case has been well insulated from the flame zone. Moreover, on the outer side of the nozzle, the absence of any type of insulation around the graphite leads to a continuous increment of the temperature at this point, which is constantly monitored and reaches 500 °C during the burn. At this temperature, the yield stress of the carbon steel becomes approximately half that at ambient temperature, but thanks to the battleship design of the chamber, which employed a very high safety factor, there is no risk of damaging the structure. Finally, the temperature of the decomposed HTP has been monitored with a thermocouple inserted immediately after the catalytic reactor.

It is interesting to notice that figure 5.21 also represents an important validation of the regression rate relationship. In fact, plotting the curve of the theoretical port diameter with the burning time, it is possible to evaluate a circular port diameter of about 95 mm at 55 s, which is approximately equivalent to the thermocouple depth of 10 mm: a value that has been experimentally confirmed by the thermocouple exposure to the direct flame. Moreover, figure 5.21 shows another important point for a paraffin hybrid motor, namely that the paraffin liquid layer blocks the heat penetration inside the grain during the burn, preventing the entire grain from being melted by an increase in temperature. In conclusion, this test demonstrates that paraffin could be safely and effectively employed even for long burn applications.

Despite not being one of the goals of the long burning time test, the average motor efficiency (evaluated by comparing the theoretical characteristic velocity calculated with a thermochemical code [45] and the measured value at the same mixture ratio) has been found to be around 95 %, which is a very good value for a preliminary configuration. However, this is expected because the motor is too long for the low oxidizer mass flow employed in the test and consequently the combustion reagents have enough space to completely mix and to achieve an efficient combustion.

6 FLIGHTWEIGHT MOTOR DESIGN

In chapters 4 and 5 a hybrid rocket motor has been developed and extensively tested. The design process follows two different approaches. The first one is based on swirl injection of HTP burning with a HDPE solid grain, while the second approach uses an axial injector and a propellant combination of HTP and a paraffin-based fuel. Swirl injection on its own guarantees high regression rates even with polymeric fuels like HDPE (other alternatives are for example PMMA, PS or nylon) and high combustion efficiency, while in the axial case a paraffin-based fuel is employed to obtain the required regression rate and a long post-combustion chamber is needed to ensure a complete combustion. A mixing device like a diaphragm can be also used to increase the combustion efficiency, having also the secondary effect of slightly enhancing the regression rate [19, 20, 47].

In both cases the HTP is first forced to pass through a catalytic reactor, where it decomposes into gaseous oxygen and water vapor at a temperature of around 1000 K, and then is injected inside the motor where its temperature is high enough to thermally decompose and ignite the fuels that are commonly used.

6.1 CONFIGURATION SELECTION

Both the configurations have their own advantages and disadvantages. For example, just to mention a few, swirl injection of HTP allows to employ polymeric fuels that are characterized by higher thermomechanical properties compared to paraffin-based fuels. However, this technology is sensitive to the catalytic reactor performance over time, which can worsen due to the degradation of the catalytic material properties. In fact, a partially liquid injection can drastically decrease the swirl intensity with major effects on the grain regression rate, the mixture ratio shift and the overall combustion efficiency. On the other hand, the opposite applies to axial injection of HTP, which is more robust in relation to the catalytic reactor degradation. This behavior has been seen in numerous experimental tests that have been conducted by the Hybrid Propulsion Group of the University of Padova, confirming that after the ignition of the motor a biphasic mixture injection does not affect the system performance. However, the axial injection is generally coupled with paraffin-based fuels that have a low melting temperature and softening point.

Nevertheless, depending on the intended application for the hybrid rocket motor, a paraffin-based fuel can be used with swirl injection

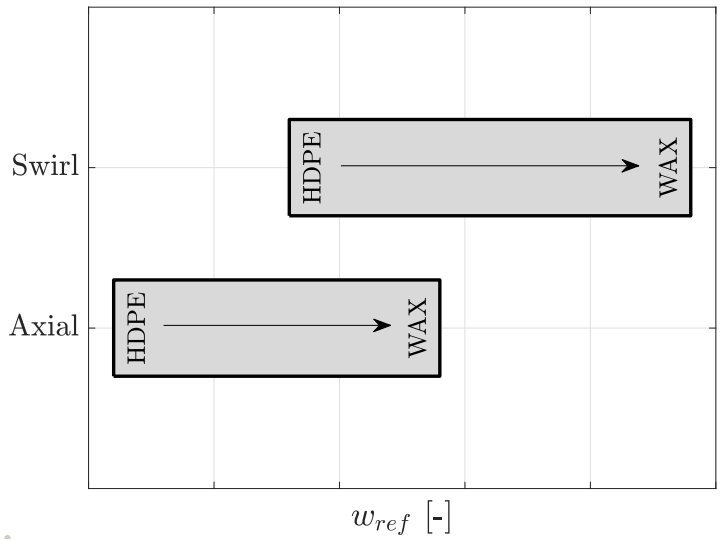

Figure 6.1: Ranges of adimensional reference web thickness

if very high regression rates are required, or a polymeric fuel can be used with axial injection if the opposite is needed. During the preliminary system analysis, it is possible to choose between the different solutions. In order to decide which configuration is best suited, it is first necessary to recall the definition of the adimensional reference web thickness (3.29) that has been suggested in chapter 3:

$$w_{ref} = \frac{aG_0^n t_b}{D_0} \tag{6.1}$$

It is adimensional because it is divided by the initial port diameter, and it is called reference because it is not the actual motor web thickness but it is the web thickness calculated as if the regression rate was kept constant and equal to the initial one. The real web thickness is always lower than the reference one because of the regression rate decay with time.

The adimensional reference web thickness varies for each configuration within a certain range that depends on the propellant combination and to some extent on the overall system design. From a systems engineering point of view, it is possible to tailor this parameter based on the mission requirements changing the injection pattern, the fuel type (also with the inclusion of energetic particles or other additives), the initial oxidizer mass flux, the initial port diameter or the total burning time. In figure 6.1 the ranges of adimensional reference web thickness for the two proposed configurations are plotted. It is possible to see that there are two opposite zones, respectively at the beginning and at the end of the graph, where a single configuration is best suited to the intended application. Moreover, the central area of the graph represents an overlap region where it is necessary to make a trade-off in order to choose the best approach, based on the advantages and disadvantages of each configuration.

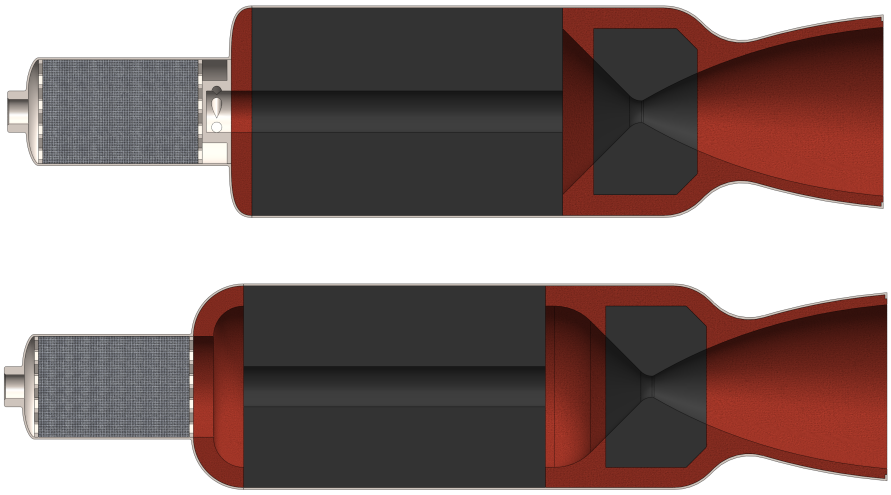

Figure 6.2: CAD model section view of the swirl injection (top) and the axial injection (bottom) expendable flightweight hybrid rocket motor

6.2 THERMAL ANALYSIS

The overall design that has been proposed up to know follows a battleship approach and resulted in a heavyweight equipment for a ground testing environment. However, several concerns arise when the design rationale moves towards a flightweight version of the same hybrid rocket motor. These issues are mainly related to the thermal behavior of the system and to the erosion of the thermal protections. For example, if the thermal protections are not sized correctly, the heat flux that is conducted towards the motor case during the burning time can increase the temperature of the material up to its operating limit point or beyond. Moreover, considering the time frame that follows the motor shutdown, the heat that has been accumulated in the system during the burning time starts to increase the temperature of the solid fuel grain and the motor case, which can reach or even overcome its non-operating limit.

Two different cases have been analyzed for both flightweight configurations, namely an expendable hybrid rocket motor and a reusable one, where the latter can be used either in single-fire or in multi-fire mode. The term expendable is related to the fact that the motor is structurally compromised already with the first firing, due to the excessive temperature increase of the motor case material that is heated during the burning time and afterwards. A CFRP case has been employed for the expendable approach, while the reusable one uses an inconel superalloy shell. In figure 6.2 the CAD models of the two different expendable flightweight configurations are presented. The advantage of using an inconel superalloy shell compared to a CFRP case is that it is able to withstand much higher temperatures, having a twofold result. The first one is trivial, that is the motor case itself can

be sized to operate at relatively higher temperatures. The second one is related to the non-linear behavior of the radiation with respect to the temperature. Remembering the Stefan–Boltzmann law that describes the power irradiated from a body in terms of its temperature:

$$\dot{q}_{rad} = \varepsilon \sigma T^4 \tag{6.2}$$

it is possible to understand that an inconel superalloy shell is also able to dissipate a larger amount of heat through radiation, since the material can reach higher temperatures compared to a CFRP case.

A monodimensional thermal analysis has been performed, for both non-ablative and ablative thermal protections and using an inconel superalloy motor case for all the configurations. The analysis is based on a numerical code developed to describe the transient behavior of hybrid rocket motors [5–7]. It considers the heat conducted through the thermal protections, which is described by the Fourier equation:

$$\frac{\partial T}{\partial t} = \alpha \nabla^2 T \tag{6.3}$$

The heat is conducted up to the inconel superalloy shell, which irradiates the thermal energy to the outer space.

Some approximations have been introduced. The first one is the monodimensionality of the analysis. For this reason, the heat is conducted only perpendicularly to the thermal protection surface:

$$\dot{q}_{cond} = -\lambda \frac{dT}{dy} \tag{6.4}$$

The second one is that the motor case is modeled as having zero thickness and so it is described by just one node, meaning that the whole inconel superalloy shell has the same temperature, which is also equal to the temperature of the last node of the thermal protections.

Moreover, the cylindrical thermal protections are simplified as flat plates. In order to verify this hypothesis and to demonstrate that the planar configuration is on the safe side, a comparison between the two cases has been done. Non-ablative thermal protections have been chosen for simplicity. A carbon fiber reinforced carbon and silicon carbide dual matrix composite with a thermal diffusivity of around $1.12 \times 10^{-5}\,\mathrm{m}^2/\mathrm{s}$ has been selected as material. The inconel superalloy shell is characterized by an emissivity of about 0.3, a limit temperature during operation (characterized by high pressure) of 650 °C, and a limit temperature during non-operation of 850 °C. In figure 6.3 the temperature variation with time of each node inside the thermal protections is presented. In figure 6.4 on the right, the temperature variation with time is shown for the planar configuration, where only the most internal and external nodes are plotted to facilitate the visualization. In figure 6.4 on the left, the temperature variation along the thermal protections thickness is presented, where only the maximum temperatures reached during operation and non-operation

are shown. In figure 6.5 it is possible to see the same results for the cylindrical configuration.

The planar configuration is characterized by higher temperatures and for this reason thicker thermal protections are required for the same burn duration. This result can be seen from the maximum axial coordinate in the aforementioned plots, which represents the thermal protections thickness. For the same burning time of 100 s, the thermal protections in the planar configuration have a thickness of 94 mm, while in the cylindrical configuration only 47 mm are needed. This phenomenon can be qualitatively understood remembering that the internal surface of the thermal protections is heated from the reacting gases of the combustion chamber, while the external surface conducts the thermal energy to the motor case. In the cylindrical configuration the thermal equilibrium gives lower temperatures with respect to the planar configuration, because the inner surface is smaller compared to the outer surface due to the geometrical shape.

Finally, the last assumptions are that all the materials are modeled as homogeneous media with isotropic properties and that the ablative thermal protections do not form char while burning.

In the next subsections, the thermal analysis for both non-ablative and ablative thermal protections will be presented and discussed. Four different flightweight configurations have been analyzed, namely the expendable case, the single-fire reusable case, the non-spaced multi-fire reusable case, and the spaced multi-fire reusable case. As previously pointed out, the term expendable is related to the fact that the motor is structurally compromised already with the first firing, due to the excessive temperature increase of the motor case material that is heated during the burning time and afterwards. Furthermore, in the non-spaced multi-fire mode the motor is fired multiple times, where the total burning time is equal to the single-fire mode, and the different firings are separated by a waiting time comparable to the burning time itself. On the other hand, in the spaced multi-fire mode each firing is separated by a longer coasting phase. For example, in this thermal analysis, a coasting phase of 90 min comparable to the orbital period of a LEO orbit has been used.

6.2.1 *Non-Ablative Thermal Protections*

The first part of the analysis is the study of the configuration with non-ablative thermal protections. A carbon fiber reinforced carbon and silicon carbide dual matrix composite with a thermal diffusivity of around $1.12 \times 10^{-5}\,m^2/s$ has been selected as material. The inconel superalloy shell is characterized by an emissivity of about 0.3, a limit temperature during operation (that is characterized by high pressure) of 650 °C and a limit temperature during non-operation of 850 °C. The same burn duration of 80 s has been used for all four cases.

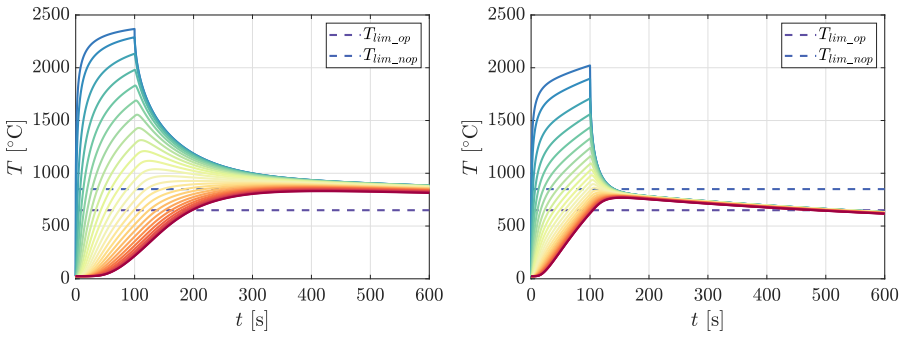

Figure 6.3: Temperature variation with time of all the nodes in the planar configuration (left) and the cylindrical one (right)

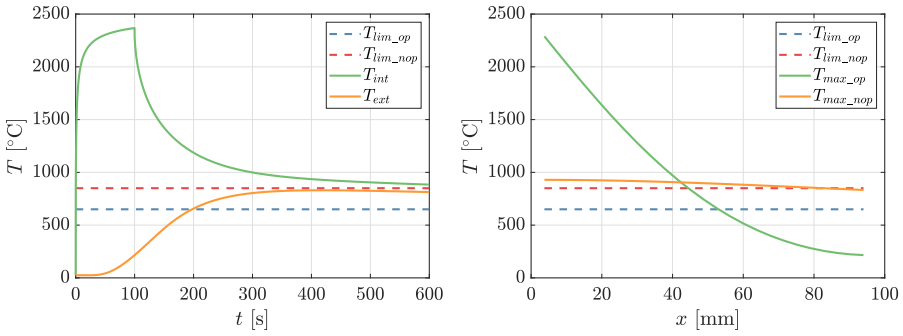

Figure 6.4: Temperature variation with time (left) and thickness (right) of the planar configuration boundary nodes

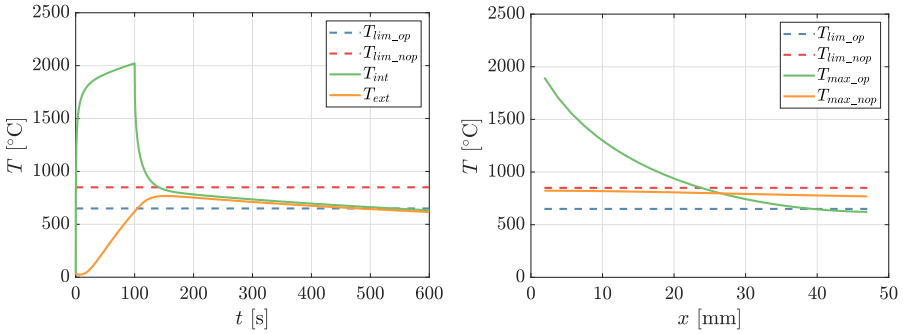

Figure 6.5: Temperature variation with time (left) and thickness (right) of the cylindrical configuration boundary nodes

The expendable case needs a thermal protections thickness equal to $a = 61\,\text{mm}$ in order to guarantee that the maximum operating temperature does not exceed the operating limit. However, this thickness is not enough to avoid any damage to the motor case during the non-operating time, as it can be seen in figure 6.6.

$$t_{tp} = a \tag{6.5}$$

This damage is prevented in the single-fire reusable case, where the thermal thickness protections is increased to $b = 84\,\text{mm}$ in order to restrict the maximum non-operating temperature below the non-operating limit, as shown in figure 6.7.

$$t_{tp} = b > a \tag{6.6}$$

It is important to underline that this relation of inequality can become an equality if the difference between the operating temperature limit and the non-operating temperature limit of the motor case material is wide enough.

Another approach is to split the total burn duration in multiple firings. However, looking at the results shown in figure 6.8 it is possible to see that if the multiple firings are equal in duration and are spaced by a time comparable to the burning time, than the thermal protections thickness is bigger even compared to the single-fire reusable case. This approach requires a thickness of $c = 98\,\text{mm}$.

$$t_{tp} = c > b \tag{6.7}$$

In order to maintain the same thickness, the motor would have to operate in a similar fashion than the "Achilles and the tortoise" paradox, with continuously decreasing burns duration.

Much better results are obtained if the multiple firings are spaced by a long costing phase, as it can be seen in figure 6.9. In this case the thermal protections thickness is equal to $d = 55\,\text{mm}$, which is smaller even compared to the expendable case, just with three or more firings.

$$t_{tp} = d < a \tag{6.8}$$

Multiple firings of equal duration have been chosen. It is also possible to have a slightly shorter first burning time in order to reduce the number of firings required, since the motor starts from a different initial condition and is not pre-heated from previous combustion.

6.2.2 *Ablative Thermal Protections*

The second part of the analysis is the study of the configuration with ablative thermal protections. In order to include the consumption

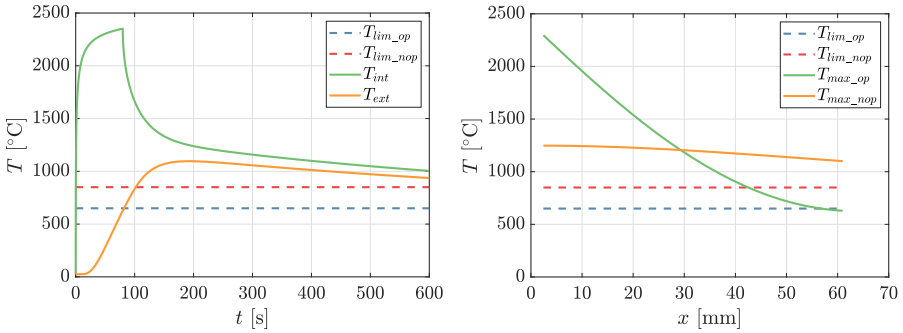

Figure 6.6: Temperatures in the expendable case

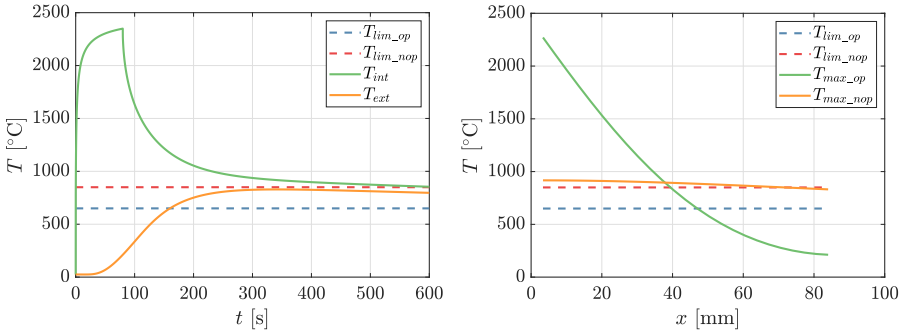

Figure 6.7: Temperatures in the single-fire reusable case

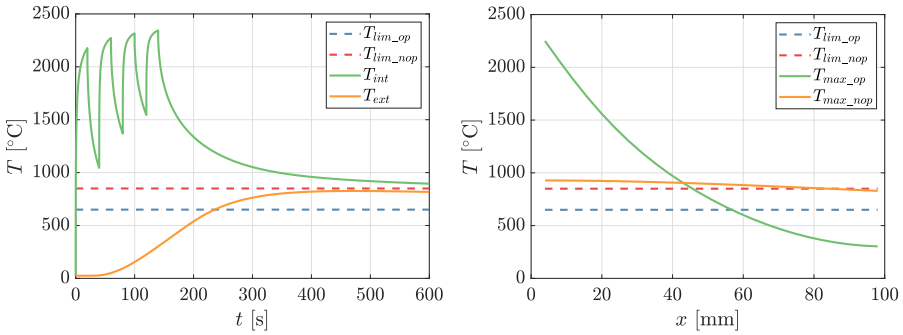

Figure 6.8: Temperatures in the non-spaced multi-fire reusable case

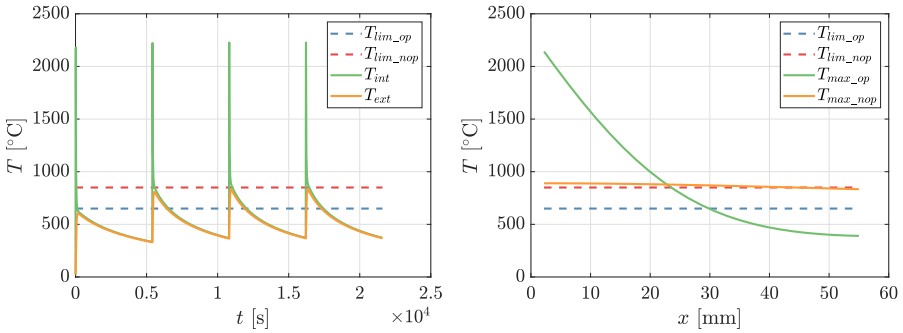

Figure 6.9: Temperatures in the spaced multi-fire reusable case

of the thermal protections during the firing, the regression rate is calculated with the Arrhenius equation:

$$\dot{r} = A \exp\left(-\frac{E_a}{RT_w}\right) \tag{6.9}$$

A silica-phenolic composite with a thermal diffusivity of around $2.83 \times 10^{-5}\,\mathrm{m}^2/\mathrm{s}$ has been selected as material. The inconel superalloy shell is characterized by an emissivity of about 0.3, a limit temperature during operation (characterized by high pressure) of 650 °C and a limit temperature during non-operation of 850 °C. The same burn duration of 80 s has been used for all four cases. The results are similar to the ones of the previous configuration with non-ablative thermal protections.

The expendable case needs a thermal protections thickness equal to $a = 11.6\,\mathrm{mm}$ in order to guarantee that the maximum operating temperature does not exceed the operating limit. Unlike the non-ablative expendable case, the thickness is also enough to avoid any damage to the motor case during the non-operating time, as it can be seen in figure 6.10. As it has been previously pointed out, the difference between the operating temperature limit and the non-operating temperature limit is wide enough to have the same results for the expendable case and the single-fire reusable case, as shown in figure 6.12.

$$t_{tp} = a = b \tag{6.10}$$

In figure 6.11 and 6.13, the instantaneous regression rate is plotted on the left, while the transient regression of the thermal protections surface is shown on the right (denoted as r_{tr}), together with the steady value of the total regression (denoted as r_{st} and calculated as $r_{st} = \dot{r} t_b$) and the thermal protections thickness (denoted as t_{tp}).

Another approach is to split the total burn duration in multiple firings. However, looking at the results shown in figure 6.14 it is possible to see that if the multiple firings are equal in duration and are spaced by a time comparable to the burning time, than the thermal protections thickness is bigger even compared to the single-fire reusable case. This approach requires a thickness of $c = 12.3\,\mathrm{mm}$.

$$t_{tp} = c > b \tag{6.11}$$

In order to maintain the same thickness, the motor would have to operate in a similar fashion than the "Achilles and the tortoise" paradox, with continuously decreasing burn duration. Again, regression rate and regression information are shown in figure 6.15.

Much better results are obtained if the multiple firings are spaced by a long costing phase (that has been reduced for computational reasons), as it can be seen in figure 6.16. In this case the thermal protections thickness is equal to $d = 10.1\,\mathrm{mm}$, which is smaller even

compared to the expendable configuration, just with three or more firings.

$$t_{tp} = d < a \tag{6.12}$$

Multiple firings of equal duration have been chosen. It is also possible to have slightly decreasing burning times in order to reduce the number of firings required, since the thermal protections are consumed during the subsequent combustions. Again, regression rate and regression information are shown in figure 6.17.

6.2.3 *Thermal Analysis Considerations*

The thermal analysis that has been performed allows to understand how to size the thermal protections and the outer shell in a hybrid rocket motor. Different approaches are needed in order to satisfy the requirements of the intended space application, depending on whether an expendable motor or a reusable one is considered.

The obtained results depend on the properties of the materials. In particular, the values of the temperature limits of the outer motor case, both during operation (characterized by high pressure) or non-operation, have a strong influence on the behavior of the system. Moreover, a higher emissivity of the outer shell corresponds to the dissipation of a larger amount of heat through radiation. However, this effect is negligible during the burning time while is substantial after the motor shutdown, when the motor is not heated up by the reaction occurring inside the combustion chamber anymore.

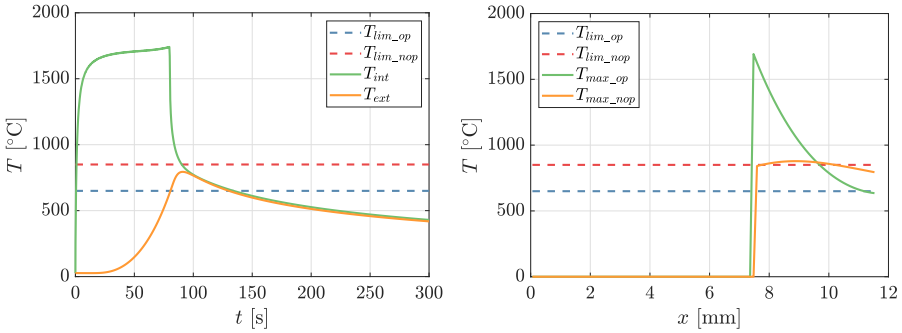

Figure 6.10: Temperatures in the expendable case

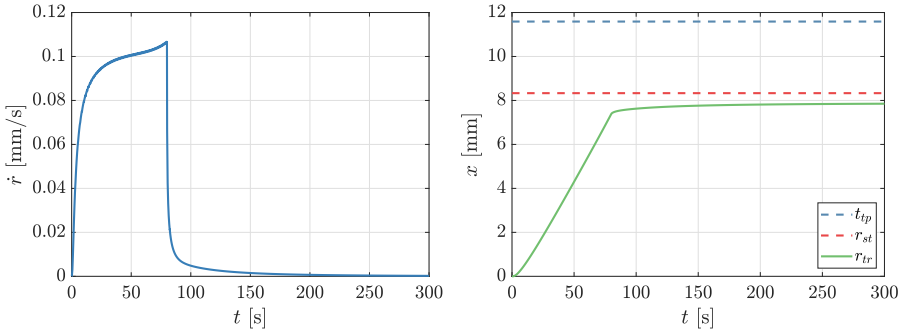

Figure 6.11: Thicknesses in the expendable case

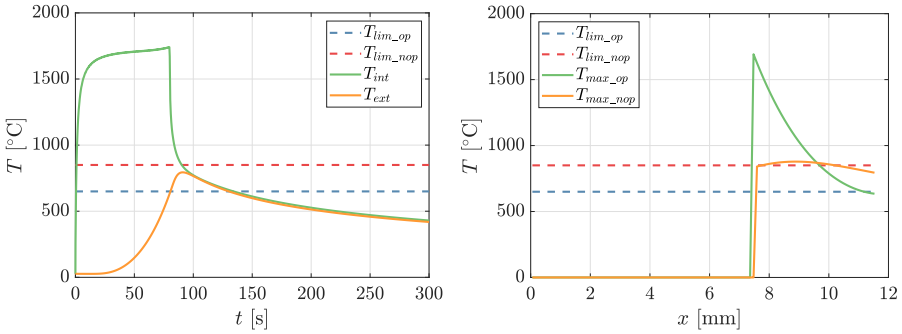

Figure 6.12: Temperatures in the single-fire reusable case

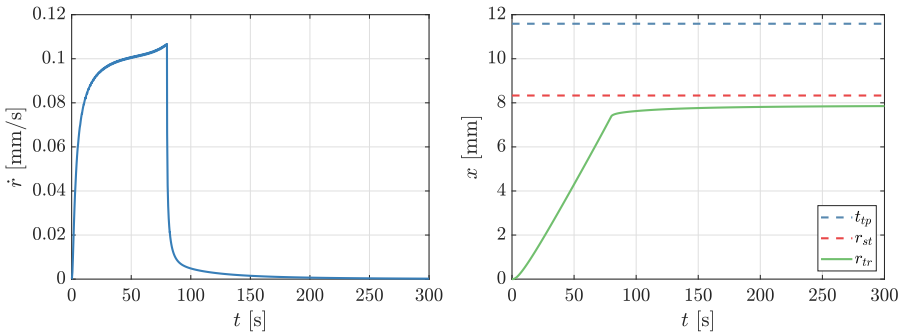

Figure 6.13: Thicknesses in the single-fire reusable case

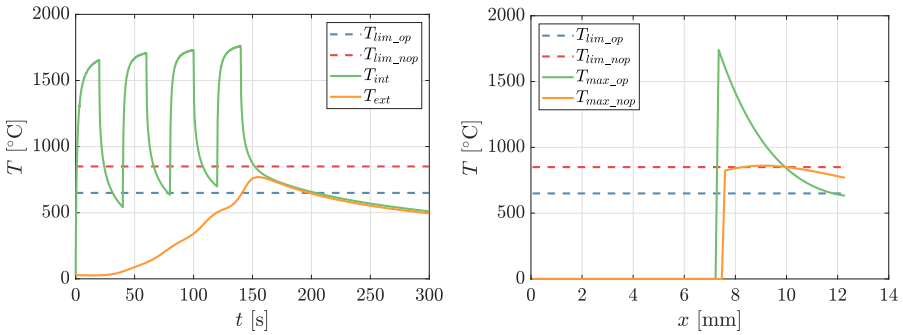

Figure 6.14: Temperatures in the non-spaced multi-fire reusable case

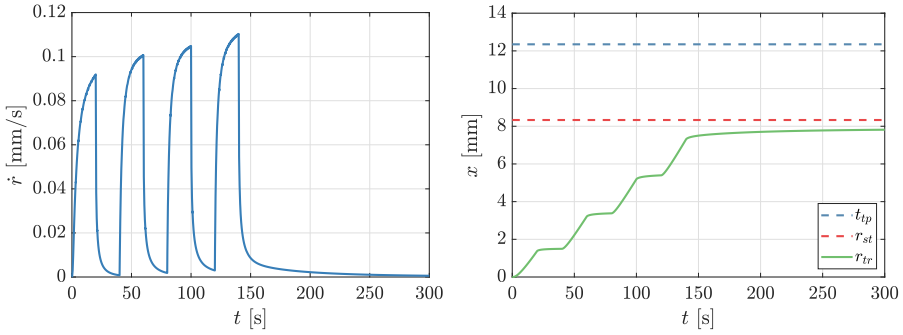

Figure 6.15: Thicknesses in the non-spaced multi-fire reusable case

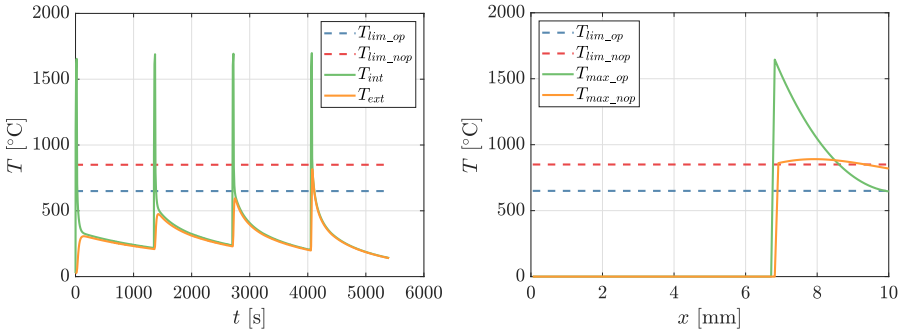

Figure 6.16: Temperatures in the spaced multi-fire reusable case

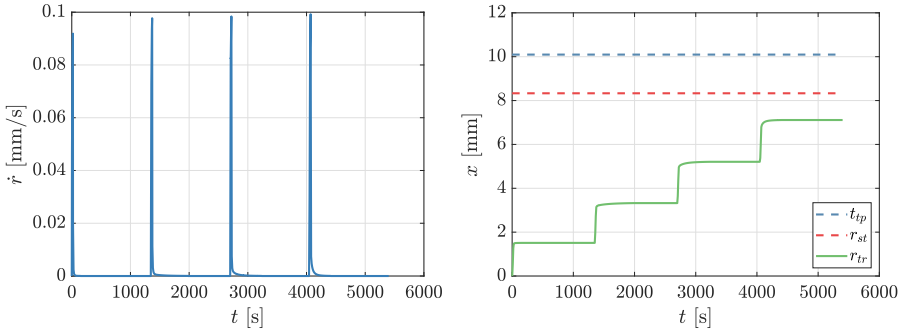

Figure 6.17: Thicknesses in the spaced multi-fire reusable case

7 CONCLUSIONS

In recent years there has been a significant renewed interest in hybrid propulsion for its unique features. Unfortunately, this technology presents also several disadvantages, which caused the lack of its widespread use for both military and commercial purposes. However, most of these drawbacks can be solved through a correct design process and choosing convenient approaches. This is not always a trivial work and this is the reason why, despite many efforts, most of the international contribution to this field is limited to conceptual designs and laboratory-scale firing tests. Therefore, the following research is focused on the development and testing of a small hybrid rocket motor, considering in particular its possible space applications. The final ambition of this work is to design a viable alternative to replace conventional propulsive systems, demonstrating its high performance and adaptability to different mission scenarios.

At the Center of Studies and Activities for Space "G. Colombo" of the University of Padova, the Hybrid Propulsion Group is very active in the development of hybrid rocket motors, primarily focusing on the reduction of the inherent disadvantages of this promising propulsive system. The presented research has been carried out within this group, which has specific CFD codes, validated for different configurations of hybrid motors, also benefiting of a test facility that is completely equipped for burning tests up to about 10 kN sea-level thrust.

Hybrid rocket motors are generally not very flexible concerning the motor configuration, and the packaging of the hybrid propulsion system is strongly related to the sizing of the combustion chamber. Therefore, it is fundamental to understand how the length, the external diameter, the volume loading and the length to diameter ratio vary with the design parameters such as scale, burning time, average mixture ratio, initial oxidizer mass flux and propellant combination. The use of explicit analytical tools has a strong beneficial effect, because it clearly shows the fundamental parameters affecting the results and their sometimes not intuitive dependencies. The key step has been the definition of the relation between initial and average mixture ratio and the asymptotic treatment with respect to the ratio between the external and internal diameter. Moreover, an approximate explicit semi-analytical expression of the instantaneous and average characteristic velocities has been provided. The explicit analytical equations have been validated with the exact implicit solutions showing good agreement and exact asymptotic behavior.

After having characterized the hybrid rocket motor behavior, defined its mission envelop, and understood the combustion chamber

sizing, two different motor configurations have been designed. The two solutions have been implemented in order to develop hybrid rocket motors with high regression rate and high combustion efficiency. The first approach is based on swirl injection of HTP burning with a HDPE solid grain, while the second one uses an axial injector and a propellant combination of HTP and a paraffin-based fuel. In both cases the HTP is first forced to pass through a catalytic reactor, where it decomposes into gaseous oxygen and water vapor at a temperature of around 1000 K. The design has been numerically verified: first only the injection system, and afterwards the whole combustion chamber. The numerical investigation confirms that the pressure drop along the injectors is about 5 % of the upstream pressure, and that all the motor configurations exhibit a very high efficiency above 97 %.

In order to demonstrate that after a correct design process it is possible to exploit the distinctive advantages of hybrid rocket motors and that this propulsive technology has reached a high maturity level, a thorough experimental campaign has been conducted. First, the configuration with swirl injection has been tested, obtaining a high efficiency, above 93 %, and a stable combustion. Thanks to the large amount of experimental tests, where the same motor configuration has been fired with different initial grain diameters, it has been possible to calculate the regression rate coefficients a and n for each swirl injector. Moreover, a correlation between the geometric swirl number and the coefficient a has been found, making it possible to tailor the regression rate simply changing the swirl injector. This means that the operational point of this particular hybrid rocket motor can be adjusted to the specific mission requirements. The throttling capability of this configuration has also been successfully verified with a real-time deep throttling firing test that reached a throttling ratio of 12.6 and showed the fast dynamic response of the system. This is a significant achievement because throttleability is a prized feature in rockets motors since it allows to perform peculiar mission profiles, such as soft landing. Afterwards, since paraffin-based fuels have been often regarded with skepticism due to their low melting temperature and softening point, the second configuration has been verified through a long burn test that resulted in a successful operation of the motor with an efficiency of around 95 %. Moreover, the liquid layer theory has been validated by monitoring the temperature of the fuel grain during the firing test. This outcome has shown that, for a paraffin hybrid motor, the liquid layer blocks the heat penetration inside the grain during the burn, preventing the entire grain from being melted by an increase in temperature. In conclusion, this test has demonstrated that paraffin could be safely and effectively employed even for long burn applications.

The two configurations that have been developed and tested have their own advantages and disadvantages. During the preliminary system analysis, it is possible to choose between the different solutions,

depending on the intended space application. In order to design a propulsive system based on hybrid rocket motors that can actually replace conventional propulsive systems, the problems that arise when designing the flightweight version of the same heavyweight motor have been analyzed. These issues are mainly related to the thermal behavior of the system and to the erosion of the thermal protections. A monodimensional thermal analysis has been performed, considering both non-ablative and ablative thermal protections. Two different cases have been considered, namely an expendable hybrid rocket motor and a reusable one, where the latter can be used either in single-fire or in multi-fire mode. The obtained numerical model allows to size the thermal protections in order to efficiently withstand the thermal loads. Different approaches are needed in order to satisfy the requirements of the intended mission, depending on whether an expendable motor or a reusable one is considered.

Much work has been done to carry out the presented research and great outcomes have been achieved. Hybrid rocket behavior and motor sizing have been analyzed and two different heavyweight configurations have been developed and successfully tested. Both solutions are perfectly suitable to several space applications, such as orbit insertion motors for small satellites, orbit raising and station keeping motors for orbit transfer vehicles, reentry systems, and throttleable motors for planetary soft landing. Generally, such space missions have a thrust that ranges between 100 N and 1000 N. The motor thrust depends on both the required Δv for the mission and the size of the satellite, and for this reason it can be scaled according to the payload weight. Moreover, it has been demonstrated that it is feasible to develop a hybrid rocket motor that can fulfill the requirements of an actual space application with high performance, thus representing an alternative solution compared to liquid or solid motors. Some issues coming from the flightweight design of the same heavyweight motor have been assessed. However, more work is needed before being able to realize an actual hybrid rocket motor for space applications in a flightweight version. For example, a more detailed thermal analysis of the hybrid rocket motor is required, before moving to the actual manufacturing and testing of the flightweight equipment. These firing tests, possibly performed in a vacuum environment to evaluate the actual in-space performance, are required in order to validate the numerical results and to refine the final design. Ad maiora semper!

ACRONYMS

CAD	Computer-aided design
CFD	Computational fluid dynamics
CFRP	Carbon fiber reinforced polymer
ESA	European Space Agency
GOX	Gaseous oxygen
HDPE	High-density polyethylene
HTP	High-test peroxide
HTPB	Hydroxyl-terminated polybutadiene
LEO	Low earth orbit
LOX	Liquid oxygen
NASA	National Aeronautics and Space Administration
ONERA	Office National d'Etudes et de Recherches Aérospatiales
P&ID	Piping and instrumentation diagram
PLC	Programmable logic controller
PMMA	Polymethylmethacrylate
PS	Polystyrene
RANS	Reynolds-averaged Navier-Stokes
RFNA	Red fuming nitric acid
SARA	Satélite de reentrada atmosférica
SHERPA	Shuttle expendable rocket for payload augmentation
SPARTAN	Space research for throttleable advanced engine
TNT	Trinitrotoluene

NOMENCLATURE

LATIN LETTERS

A	Area, Arrhenius pre-exponential factor
a	Acceleration, regression rate constant
B	Blowing parameter
c	Specific heat capacity
$c^\star$	Characteristic velocity
C_D	Discharge coefficient
C_F	Thrust coefficient
C_f	Skin friction coefficient
c_p	Specific heat capacity at constant pressure
D	Diameter, diffusion
Da	Damköhler number
E_a	Activation energy
F	Thrust
G	Mass flux
g_0	Standard gravitational acceleration
h	Entalpy
h_v	Heat of vaporization
I_{sp}	Specific impulse
k	Absorption coefficient, turbulent kinetic energy
L	Length
L_v	Laten heat of vaporization
Le	Lewis number
M	Mass
m	Regression rate length exponent
$\dot{m}$	Mass flow
Ma	Mach number
N	Number
n	Regression rate mass flux exponent
P	Pressure
Pr	Prandtl number
$\dot{q}$	Heat flux
R	Diameter ratio, radius, universal gas constant
r	Regression
$\dot{r}$	Regression rate
S	Sink, source
Sc	Schmidt number
SF	Safety factor
SN	Swirl number
St	Stanton number
T	Temperature
t	Thickness, time

v	Velocity
VL	Volume loading
w	Web thickness
X	Mass fraction
x	Combustion chamber axial coordinate
y	Coordinate perpendicular to the surface

GREEK LETTERS

α	Absorptivity, divergent angle, thermal diffusivity
γ	Heat capacity ratio
ε	Emissivity, error, expansion ratio, mass flow contribution
η	Efficiency, flame position
ϑ	Temperature ratio
λ	Thermal conductivity
μ	Dinamic viscosity
ν	Kinematic viscosity
ϱ	Density
σ	Stefan–Boltzmann constant, tensile strength
τ	Shear stress, time scale
Φ	Fluid unknown, velocity ratio
φ	Mixture ratio
ω	Specific dissipation rate

SUBSCRIPTS

0	Initial, reference, total
a	Ambient
avg	Average
b	Burning
c	Chemical
cc	Combustion chamber
cond	Conductive
conv	Convective
cpf	Cotton-phenolic flange
cyl	Cylinder
D	Diameter
e	Edge, exit
ex	Experimental
ext	External
F	Thrust
f	Final, fuel
fl	Flame, flange
fun	Function
g	Gas, geometric
gr	Grain
h	Hole
in	Initial
int	Internal, intersection

lim	Limit
m	Molar
max	Maximum
min	Minimum
nop	Non-operating
num	Numerical
op	Operating
opt	Optimum
ox	Oxidizer
P	Pressure
p	Port, propellant
post	Post-combustion chamber
pre	Pre-combustion chamber
R	Relative
rad	Radiative
ref	Reference
s	Soot
sat	Saturation
st	Steady
t	Throat, turbulent
th	Theoretical
tot	Total
tp	Thermal protection
tr	Transient
up	Upstream
vac	Vacuum
w	Wall
x	Axial, local
ϑ	Tangential
Φ	Fluid unknown

BIBLIOGRAPHY

[1] A. Abdelhafez and A. K. Gupta. "Swirling Airflow Through a Nozzle: Choking Criteria". In: *Journal of Propulsion and Power* 26.4 (July 2010), pp. 754–764. DOI: 10.2514/1.47956.

[2] D. Altman and A. Holzman. "Overview and History of Hybrid Rocket Propulsion". In: *Fundamentals of Hybrid Rocket Combustion and Propulsion*. Ed. by K. K. Kuo and M. J. Chiaverini. Reston, VA, United States: American Institute of Aeronautics and Astronautics, Jan. 2007. DOI: 10.2514/4.866876.

[3] D. Altman and R. W. Humble. "Hybrid Rocket Propulsion Systems". In: *Space Propulsion Analysis and Design*. Ed. by R. W. Humble. Space Technology Series. OCLC: 833153187. New York, NY, United States: McGraw-Hill, 1995.

[4] F. Barato. "Numerical and Experimental Investigation of Hybrid Rocket Motors Transient Behavior". PhD Thesis. Padova, Italy: Università degli Studi di Padova, 2013.

[5] F. Barato, N. Bellomo, M. Faenza, M. Lazzarin, A. Bettella, and D. Pavarin. "A Numerical Model to Analyze the Transient Behavior and Instabilities on Hybrid Rocket Motors". In: *47th AIAA/SAE/ASEE Joint Propulsion Conference & Exhibit*. San Diego, CA, United States: American Institute of Aeronautics and Astronautics, July 31–Aug. 3, 2011. DOI: 10.2514/6.2011-5538.

[6] F. Barato, N. Bellomo, M. Faenza, M. Lazzarin, A. Bettella, and D. Pavarin. "Numerical Model to Analyze Transient Behavior and Instabilities on Hybrid Rocket Motors". In: *Journal of Propulsion and Power* 31.2 (Mar. 2015), pp. 643–653. DOI: 10.2514/1.B35282.

[7] F. Barato, N. Bellomo, M. Lazzarin, F. Moretto, A. Bettella, and D. Pavarin. "Numerical Modeling of Paraffin-Based Fuels Behavior". In: *48th AIAA/SAE/ASEE Joint Propulsion Conference & Exhibit*. Atlanta, GA, United States: American Institute of Aeronautics and Astronautics, July 30–Aug. 1, 2012. DOI: 10.2514/6.2012-3750.

[8] F. Barato, N. Bellomo, and D. Pavarin. "Integrated Approach for Hybrid Rocket Technology Development". In: *Acta Astronautica* 128 (Nov. 2016), pp. 257–261. DOI: 10.1016/j.actaastro.2016.07.023.

[9] F. Barato, M. Faenza, N. Bellomo, M. Lazzarin, A. Bettella, and D. Pavarin. "Numerical Simulations of an H2O2 Vortex Hybrid Rocket Motor". In: *Space Propulsion 2012*. Bordeaux, France: Association Aéronautique et Astronautique de France, May 7–10, 2012.

[10] F. Barato, M. Grosse, and A. Bettella. "Hybrid Rocket Fuel Residuals - An Overlooked Topic". In: *50th AIAA/ASME/SAE/ASEE Joint Propulsion Conference*. Cleveland, OH, United States: American Institute of Aeronautics and Astronautics, July 28–30, 2014. DOI: 10.2514/6.2014-3753.

[11] F. Barato, E. Paccagnella, and D. Pavarin. "Explicit Analytical Equations for Single Port Hybrid Rocket Combustion Chamber Sizing". In: *53rd AIAA/SAE/ASEE Joint Propulsion Conference*. Atlanta, GA, United States: American Institute of Aeronautics and Astronautics, July 10–12, 2017. DOI: 10.2514/6.2017-4641.

[12] F. Barato, E. Paccagnella, G. Venturelli, D. Pavarin, F. Picano, and J.-Y. Lestrade. "Numerical Simulations of an Isochoric Hybrid Rocket Combustion Chamber and Comparison with Tests". In: *8th European Conference for Aeronautics and Space Sciences*. Madrid, Spain: EUCASS, July 1–4, 2019.

[13] F. Barato, E. Paccagnella, G. Venturelli, M. Scarpa, F. Picano, D. Pavarin, and J.-Y. Lestrade. "Numerical Simulation of an Isochoric Combustion Chamber for Hybrid Rocket Propulsion". In: *Space Propulsion 2016*. Rome, Italy: Association Aéronautique et Astronautique de France, May 2–6, 2016.

[14] J. M. Beér and N. A. Chigier. *Combustion Aerodynamics*. Fuel and Energy Science Series. London, United Kingdom: Applied Science Publishers Ltd, 1972.

[15] N. Bellomo, F. Barato, M. Faenza, M. Lazzarin, A. Bettella, and D. Pavarin. "Numerical and Experimental Investigation of Unidirectional Vortex Injection in Hybrid Rocket Engines". In: *Journal of Propulsion and Power* 29.5 (Sept. 2013), pp. 1097–1113. DOI: 10.2514/1.B34506.

[16] N. Bellomo, F. Barato, M. Faenza, M. Lazzarin, A. Bettella, and D. Pavarin. "Numerical and Experimental Investigation on Vortex Injection in Hybrid Rocket Motors". In: *47th AIAA/ASME/SAE/ASEE Joint Propulsion Conference & Exhibit*. San Diego, CA, United States: American Institute of Aeronautics and Astronautics, July 31–Aug. 3, 2011. DOI: 10.2514/6.2011-5675.

[17] N. Bellomo, M. Faenza, F. Barato, A. Bettella, and D. Pavarin. "The "Vortex Reloaded" Project: Numerical Investigation on Fully Tangential Vortex Injection in N2O - Paraffin Hybrid Motors". In: *48th AIAA/ASME/SAE/ASEE Joint Propulsion Conference & Exhibit*. Atlanta, GA, United States: American Institute

of Aeronautics and Astronautics, July 30–Aug. 1, 2012. DOI: 10.2514/6.2012-3903.

[18] N. Bellomo, M. Faenza, F. Barato, A. Bettella, D. Pavarin, and A. Selmo. "The "Vortex Reloaded" Project: Experimental Investigation on Fully Tangential Vortex Injection in N2O - Paraffin Hybrid Motors". In: *48th AIAA/ASME/SAE/ASEE Joint Propulsion Conference & Exhibit*. Atlanta, GA, United States: American Institute of Aeronautics and Astronautics, July 30–Aug. 1, 2012. DOI: 10.2514/6.2012-4304.

[19] N. Bellomo, M. Lazzarin, F. Barato, and M. Grosse. "Numerical Investigation of the Effect of a Diaphragm on the Performance of a Hybrid Rocket Motor". In: *46th AIAA/ASME/SAE/ASEE Joint Propulsion Conference & Exhibit*. Nashville, TN, United States: American Institute of Aeronautics and Astronautics, July 25–Aug. 28, 2010. DOI: 10.2514/6.2010-7033.

[20] A. Bettella, M. Lazzarin, N. Bellomo, F. Barato, D. Pavarin, and M. Grosse. "Testing and CFD Simulation of Diaphragm Hybrid Rocket Motors". In: *47th AIAA/ASME/SAE/ASEE Joint Propulsion Conference & Exhibit*. San Diego, CA, United States: American Institute of Aeronautics and Astronautics, July 31–Aug. 3, 2011. DOI: 10.2514/6.2011-6023.

[21] A. Bettella, F. Moretto, E. Geremia, N. Bellomo, D. Pavarin, and D. Petronio. "Development and Flight Testing of a Hybrid Rocket Booster for UAV Assisted Take Off". In: *49th AIAA/ASME/SAE/ASEE Joint Propulsion Conference*. San Jose, CA, United States: American Institute of Aeronautics and Astronautics, July 14–17, 2013. DOI: 10.2514/6.2013-4140.

[22] T. A. Boardman. "Hybrid Propellants Rocket Propulsion". In: *Rocket Propulsion Elements*. Ed. by G. P. Sutton and O. Biblarz. Hoboken, NJ, United States: John Wiley & Sons Inc, 2017.

[23] T. A. Boardman, R. Carpenter, and S. Claflin. "A Comparative Study of the Effects of Liquid- Versus Gaseous-Oxygen Injection on Combustion Stability in 11-Inch-Diameter Hybrid Motors". In: *33rd Joint Propulsion Conference and Exhibit*. Seattle, WA, United States: American Institute of Aeronautics and Astronautics, July 6–9, 1997. DOI: 10.2514/6.1997-2936.

[24] N. Boman and M. Ford. "Design of a Hybrid Propulsion System for Orbit Raising Applications". In: *2nd International Conference on Green Propellants for Space Propulsion*. Cagliari, Italy, June 7–8, 2004.

[25] M. Calabro, L. T. De Luca, L. Galfetti, H. Raina, and C. Perut. "Advanced Hybrid Solid Fuels". In: *58th International Astronautical Congress*. Hyderabad, India: International Astronautical Federation, Sept. 24–28, 2007, p. 7.

[26] R. E. Carlson, A. Nowinski, J. Jones, J. Rothman, and S. Buckley. "Improving Space-Asset Responsiveness Using the Shuttle Expendable Rocket for Payload Augmentation (SHERPA)". In: *1st Responsive Space Conference*. Redondo Beach, CA, United States, Apr. 1–3, 2003.

[27] C. Carmicino and A. Russo Sorge. "Influence of a Conical Axial Injector on Hybrid Rocket Performance". In: *Journal of Propulsion and Power* 22.5 (Sept. 2006), pp. 984–995. DOI: 10.2514/1.19528.

[28] C. Carmicino and A. Russo Sorge. "Role of Injection in Hybrid Rockets Regression Rate Behaviour". In: *Journal of Propulsion and Power* 21.4 (July 2005), pp. 606–612. DOI: 10.2514/1.9945.

[29] C. Carmicino and A. Russo Sorge. "The Effects of Oxidizer Injector Design on Hybrid Rockets Combustion Stability". In: *42nd AIAA/ASME/SAE/ASEE Joint Propulsion Conference & Exhibit*. Sacramento, CA, United States: American Institute of Aeronautics and Astronautics, July 9–12, 2006. DOI: 10.2514/6.2006-4677.

[30] E. Casillas, C. Shaeffer, and J. Trowbridge. "Cost and Performance Payoffs Inherent in Increased Fuel Regression Rates". In: *33rd Joint Propulsion Conference and Exhibit*. Seattle, WA, United States: American Institute of Aeronautics and Astronautics, July 6–9, 1997. DOI: 10.2514/6.1997-3081.

[31] A. Chandler, B. J. Cantwell, G. Scott Hubbard, and A. Karabeyoglu. "Feasibility of a Single Port Hybrid Propulsion System for a Mars Ascent Vehicle". In: *Acta Astronautica* 69.11-12 (Dec. 2011), pp. 1066–1072. DOI: 10.1016/j.actaastro.2011.07.004.

[32] M. J. Chiaverini. "Review of Solid-Fuel Regression Rate Behavior in Classical and Nonclassical Hybrid Rocket Motors". In: *Fundamentals of Hybrid Rocket Combustion and Propulsion*. Ed. by K. K. Kuo and M. J. Chiaverini. Reston, VA, United States: American Institute of Aeronautics and Astronautics, Jan. 2007. DOI: 10.2514/4.866876.

[33] M. J. Chiaverini, K. K. Kuo, A. Peretz, and G. C. Harting. "Regression-Rate and Heat-Transfer Correlations for Hybrid Rocket Combustion". In: *Journal of Propulsion and Power* 17.1 (Jan. 2001), pp. 99–110. DOI: 10.2514/2.5714.

[34] M. J. Chiaverini, N. Serin, D. K. Johnson, Y.-C. Lu, K. K. Kuo, and G. A. Risha. "Regression Rate Behavior of Hybrid Rocket Solid Fuels". In: *Journal of Propulsion and Power* 16.1 (Jan. 2000), pp. 125–132. DOI: 10.2514/2.5541.

[35] T. Claypole and N. Syred. "The Effect of Swirl Burner Aerodynamics on NOx Formation". In: *Symposium (International) on Combustion* 18.1 (1981), pp. 81–89. DOI: 10.1016/S0082-0784(81)80013-6.

[36] S. Contadin, A. Conte, A. C. Karp, E. T. Jens, D. Vaughan, and D. Pastrone. "Thermal Analysis of a Hybrid Rocket Propulsion System for Interplanetary CubeSats". In: *7th European Conference for Aeronautics and Space Sciences*. Milano, Italy: EUCASS, July 3–6, 2017. DOI: 10.13009/EUCASS2017-613.

[37] A. Conte, S. Contadin, A. C. Karp, E. T. Jens, D. Vaughan, and D. Pastrone. "CFD Simulation of Hybrid Rocket Motors for Interplanetary CubeSats". In: *7th European Conference for Aeronautics and Space Sciences*. Milano, Italy: EUCASS, July 3–6, 2017. DOI: 10.13009/EUCASS2017-614.

[38] A. D. Cutler and R. W. Barnwell. "Vortex Flow in a Convergent-Divergent Nozzle". In: *AIAA Journal* 37.10 (Oct. 1999), pp. 1329–1331. DOI: 10.2514/2.606.

[39] P. L. K. Da Cás, C. Q. Vilanova, M. N. D. Barcelos Jr., and C. A. G. Veras. "An Optimized Hybrid Rocket Motor for the SARA Platform Reentry System". In: *Journal of Aerospace Technology and Management* 4.3 (2012), pp. 317–330. DOI: 10.5028/jatm.2012.04032312.

[40] P. Estey, J. McFarlane, R. Kniffen, and J. Lichatowich. "Large Hybrid Rocket Testing Results". In: *Space Programs and Technologies Conference and Exhibit*. Huntsville, AL, United States: American Institute of Aeronautics and Astronautics, Sept. 21–23, 1993. DOI: 10.2514/6.1993-4279.

[41] E. Farbar, J. Louwers, and T. Kaya. "Investigation of Metallized and Nonmetallized Hydroxyl Terminated Polybutadiene/Hydrogen Peroxide Hybrid Rockets". In: *Journal of Propulsion and Power* 23.2 (Mar. 2007), pp. 476–486. DOI: 10.2514/1.22091.

[42] A. Gany and Y. Manheimer-Timnat. "Parametric Study of a Hybrid Rocket Motor". In: *Israel Journal of Technology* 10.1-2 (1972), pp. 85–96.

[43] A. Gany, M. Mor, and C. Goldman. "Analysis and Characteristics of Choked Swirling Nozzle Flows". In: *AIAA Journal* 43.10 (Oct. 2005), pp. 2177–2181. DOI: 10.2514/1.16887.

[44] S. Gomes, L. Rocco, J. Rocco, and K. Iha. "Gaseous Oxygen Injection Effects in Hybrid Labscale Rocket Motor Operations". In: *46th AIAA/ASME/SAE/ASEE Joint Propulsion Conference & Exhibit*. Nashville, TN, United States: American Institute of Aeronautics and Astronautics, July 25–28, 2010. DOI: 10.2514/6.2010-6545.

[45] S. Gordon and B. J. McBride. *Computer Program for Calculation of Complex Chemical Equilibrium Compositions and Applications. Part 1: Analysis*. NASA Reference Publication 1311. Cleveland, OH, United States: NASA Lewis Research Center, Oct. 1, 1994.

[46] M. Grosse. "Design Challenges for a Cost Competitive Hybrid Rocket Booster". In: *2nd European Conference for Aeronautics and Space Sciences*. Brussels, Belgium: EUCASS, July 1–6, 2007.

[47] M. Grosse. "Effect of a Diaphragm on Performance and Fuel Regression of a Laboratory Scale Hybrid Rocket Motor Using Nitrous Oxide and Paraffin". In: *45th AIAA/ASME/SAE/ASEE Joint Propulsion Conference & Exhibit*. Denver, CO, United States: American Institute of Aeronautics and Astronautics, Aug. 2–5, 2009. DOI: 10.2514/6.2009-5113.

[48] E. T. Jens, A. C. Karp, S. Contadin, A. Conte, B. Nakazono, and D. Vaughan. "Development Testing of Hybrid Rocket Motors Using Classical Fuels for Interplanetary CubeSats". In: *53rd AIAA/SAE/ASEE Joint Propulsion Conference*. Atlanta, GA, United States: American Institute of Aeronautics and Astronautics, July 10–12, 2017. DOI: 10.2514/6.2017-4981.

[49] E. T. Jens, A. C. Karp, B. Nakazono, D. B. Eldred, M. E. DeVost, and D. Vaughan. "Design of a Hybrid CubeSat Orbit Insertion Motor". In: *52nd AIAA/SAE/ASEE Joint Propulsion Conference*. Salt Lake City, UT, United States: American Institute of Aeronautics and Astronautics, July 25–27, 2016. DOI: 10.2514/6.2016-4961.

[50] C. Jones, D. Myre, and J. Cowart. "Performance and Analysis of Vortex Oxidizer Injection in a Hybrid Rocket Motor". In: *45th AIAA/ASME/SAE/ASEE Joint Propulsion Conference & Exhibit*. Denver, CO, United States: American Institute of Aeronautics and Astronautics, Aug. 2–5, 2009. DOI: 10.2514/6.2009-4938.

[51] A. Karabeyoglu. "Advanced Hybrid Rockets for Future Space Launch". In: *5th European Conference for Aeronautics and Space Sciences*. Munich, Germany: EUCASS, July 1–5, 2013.

[52] A. Karabeyoglu. "Challenges in the Development of Large-Scale Hybrid Rockets". In: *International Journal of Energetic Materials and Chemical Propulsion* 16.3 (2017), pp. 243–261. DOI: 10.1615/IntJEnergeticMaterialsChemProp.2018022732.

[53] A. Karabeyoglu. "Performance Additives for Hybrid Rockets". In: *Chemical Rocket Propulsion*. Ed. by L. T. De Luca, T. Shimada, V. P. Sinditskii, and M. Calabro. Cham, Switzerland: Springer International Publishing, 2017, pp. 139–163. DOI: 10.1007/978-3-319-27748-6_5.

[54] A. Karabeyoglu, B. Cantwell, and J. Stevens. "Evaluation of the Homologous Series of Normal Alkanes as Hybrid Rocket Fuels". In: *41st AIAA/ASME/SAE/ASEE Joint Propulsion Conference & Exhibit*. Tucson, AZ, United States: American Institute of Aeronautics and Astronautics, July 10–13, 2005. DOI: 10.2514/6.2005-3908.

[55] A. Karabeyoglu, S. De Zilwa, G. Zilliac, and B. Cantwell. "Transient Modeling of Hybrid Rocket Low Frequency Instabilities". In: *39th AIAA/ASME/SAE/ASEE Joint Propulsion Conference and Exhibit*. Huntsville, AL, United States: American Institute of Aeronautics and Astronautics, July 20–23, 2003. DOI: 10.2514/6.2003-4463.

[56] A. Karabeyoglu, J. Stevens, D. Geyzel, B. Cantwell, and D. Micheletti. "High Performance Hybrid Upper Stage Motor". In: *47th AIAA/ASME/SAE/ASEE Joint Propulsion Conference & Exhibit*. San Diego, CA, United States: American Institute of Aeronautics and Astronautics, July 31–Aug. 3, 2011. DOI: 10.2514/6.2011-6025.

[57] A. Karabeyoglu, G. Zilliac, B. J. Cantwell, S. De Zilwa, and P. Castellucci. "Scale-Up Tests of High Regression Rate Paraffin-Based Hybrid Rocket Fuels". In: *Journal of Propulsion and Power* 20.6 (Nov. 2004), pp. 1037–1045. DOI: 10.2514/1.3340.

[58] M. A. Karabeyoglu, D. Altman, and B. J. Cantwell. "Combustion of Liquefying Hybrid Propellants: Part 1, General Theory". In: *Journal of Propulsion and Power* 18.3 (May 2002), pp. 610–620. DOI: 10.2514/2.5975.

[59] M. A. Karabeyoglu and B. J. Cantwell. "Combustion of Liquefying Hybrid Propellants: Part 2, Stability of Liquid Films". In: *Journal of Propulsion and Power* 18.3 (May 2002), pp. 621–630. DOI: 10.2514/2.5976.

[60] M. A. Karabeyoglu, B. J. Cantwell, and G. Zilliac. "Development of Scalable Space-Time Averaged Regression Rate Expressions for Hybrid Rockets". In: *Journal of Propulsion and Power* 23.4 (July 2007), pp. 737–747. DOI: 10.2514/1.19226.

[61] D. Kearney, K. Joiner, M. Gnau, and M. Casemore. "Improvements to the Marketability of Hybrid Propulsion Technologies". In: *AIAA SPACE 2007 Conference & Exposition*. Long Beach, CA, United States: American Institute of Aeronautics and Astronautics, Sept. 18–20, 2007. DOI: 10.2514/6.2007-6144.

[62] W. Knuth, M. J. Chiaverini, J. A. Sauer, and D. J. Gramer. "Solid-Fuel Regression Rate Behavior of Vortex Hybrid Rocket Engines". In: *Journal of Propulsion and Power* 18.3 (May 2002), pp. 600–609. DOI: 10.2514/2.5974.

[63] W. Knuth, M. Chiaverini, D. Gramer, and J. Sauer. "Experimental Investigation of a Vortex-Driven High-Regression Rate Hybrid Rocket Engine". In: *34th AIAA/ASME/SAE/ASEE Joint Propulsion Conference and Exhibit*. Cleveland, OH, United States: American Institute of Aeronautics and Astronautics, July 13–15, 1998. DOI: 10.2514/6.1998-3348.

[64] W. Knuth, D. Gramer, M. Chiaverini, and J. Sauer. "Development and Testing of a Vortex-Driven, High-Regression Rate Hybrid Rocket Engine". In: *34th AIAA/ASME/SAE/ASEE Joint Propulsion Conference and Exhibit*. Cleveland, OH, United States: American Institute of Aeronautics and Astronautics, July 13–15, 1998. DOI: 10.2514/6.1998-3507.

[65] W. Knuth, D. Gramer, M. Chiaverini, J. Sauer, R. Whitesides, and R. Dill. "Preliminary CFD Analysis of the Vortex Hybrid Rocket Chamber and Nozzle Flow Field". In: *34th AIAA/ASME/SAE/ASEE Joint Propulsion Conference and Exhibit*. Cleveland, OH, United States: American Institute of Aeronautics and Astronautics, July 13–15, 1998. DOI: 10.2514/6.1998-3351.

[66] H. W. Koehler. "Fehlerrechnung für Hybridraketentriebwerke". PhD Thesis. Munich, Germany: Technische Universität München, 1972.

[67] C. P. Kumar and A. Kumar. "Effect of Swirl on the Regression Rate in Hybrid Rocket Motors". In: *Aerospace Science and Technology* 29.1 (Aug. 2013), pp. 92–99. DOI: 10.1016/j.ast.2013.01.011.

[68] K. K. Kuo and M. J. Chiaverini. "Challenges of Hybrid Rocket Propulsion in the 21st Century". In: *Fundamentals of Hybrid Rocket Combustion and Propulsion*. Ed. by K. K. Kuo and M. J. Chiaverini. Reston, VA, United States: American Institute of Aeronautics and Astronautics, Jan. 2007. DOI: 10.2514/4.866876.

[69] M. Lazzarin, M. Faenza, F. Barato, N. Bellomo, and A. Bettella. "Numerical Simulation of Hybrid Rockets Liquid Injection and Comparison with Experiments". In: *Journal of Propulsion and Power* 31.1 (Jan. 2015), pp. 352–364. DOI: 10.2514/1.B35223.

[70] T.-S. Lee and A. Potapkin. "The Performance of a Hybrid Rocket with Swirlin GOx Injection". In: *11th International Conference on the Methods of Aerophysical Research*. 2002, p. 7.

[71] G. Lengelle, R. Foucaud, J. Godon, A. Heslouin, R. Lecourt, Y. Maisonneuve, and N. Pillet. "Hybrid Propulsion for Small Satellites Analysis and Tests". In: *35th Joint Propulsion Conference and Exhibit*. Los Angeles, CA, United States: American Institute of Aeronautics and Astronautics, June 20–24, 1999. DOI: 10.2514/6.1999-2321.

[72] A. Mager. "Approximate Solution of Isentropic Swirling Flow Through a Nozzle". In: *ARS Journal* 31.8 (Aug. 1961), pp. 1140–1148. DOI: 10.2514/8.5732.

[73] J. Majdalani. "Vortex Injection Hybrid Rockets". In: *Fundamentals of Hybrid Rocket Combustion and Propulsion*. Ed. by K. K. Kuo and M. J. Chiaverini. Reston, VA, United States: American Institute of Aeronautics and Astronautics, Jan. 2007. DOI: 10.2514/4.866876.

[74] G. Marxman and M. Gilbert. "Turbulent Boundary Layer Combustion in the Hybrid Rocket". In: *Symposium (International) on Combustion* 9.1 (Jan. 1963), pp. 371–383. DOI: 10.1016/S0082-0784(63)80046-6.

[75] G. Marxman, R. Muzzy, and C. Wooldridge. "Fundamentals of Hybrid Boundary Layer Combustion". In: *Heterogeneous Combustion Conference*. Palm Beach, FL, United States: American Institute of Aeronautics and Astronautics, Dec. 11–13, 1963. DOI: 10.2514/6.1963-505.

[76] G. A. Marxman. "Boundary-Layer Combustion in Propulsion". In: *Symposium (International) on Combustion* 11.1 (Jan. 1967), pp. 269–289. DOI: 10.1016/S0082-0784(67)80153-X.

[77] G. A. Marxman. "Combustion in The Turbulent Boundary Layer on a Vaporizing Surface". In: *Symposium (International) on Combustion* 10.1 (Jan. 1965), pp. 1337–1349. DOI: 10.1016/S0082-0784(65)80268-5.

[78] M. Masugi, T. Ide, T. Sakurai, S. Yuasa, N. Shiraishi, and T. Shimada. "Visualization of Flames in Combustion Chamber of Swirling-Oxidizer-Flow-Type Hybrid Rocket Engines". In: *46th AIAA/ASME/SAE/ASEE Joint Propulsion Conference & Exhibit*. Nashville, TN, United States: American Institute of Aeronautics and Astronautics, July 25–28, 2010. DOI: 10.2514/6.2010-6546.

[79] A. McCormick, E. Hultgren, M. Lichtman, J. Smith, R. Sneed, and S. Azimi. "Design, Optimization, and Launch of a 3" Diameter N2O/Aluminized Paraffin Rocket". In: *41st AIAA/ASME/SAE/ASEE Joint Propulsion Conference & Exhibit*. Tucson, AZ, United States: American Institute of Aeronautics and Astronautics, July 10–13, 2005. DOI: 10.2514/6.2005-4095.

[80] F. R. Menter. "Two-Equation Eddy-Viscosity Turbulence Models for Engineering Applications". In: *AIAA Journal* 32.8 (Aug. 1994), pp. 1598–1605. DOI: 10.2514/3.12149.

[81] D. Myre, P. Caton, J. Cowart, and C. Jones. "Exhaust Gas Analysis of a Vortex Oxidizer Injection Hybrid Rocket Motor". In: *46th AIAA/ASME/SAE/ASEE Joint Propulsion Conference & Exhibit*. Nashville, TN, United States: American Institute of

Aeronautics and Astronautics, July 25–28, 2010. DOI: 10.2514/6.2010-6548.

[82] D. D. Ordahl and W. A. Rains. "Recent Developments and Current Status of Hybrid Rocket Propulsion". In: *Journal of Spacecraft and Rockets* 2.6 (Nov. 1965), pp. 923–926. DOI: 10.2514/3.28315.

[83] E. Paccagnella, F. Barato, D. Pavarin, and A. Karabeyoglu. "Scaling of Hybrid Rocket Motors with Swirling Oxidizer Injection". In: *51st AIAA/SAE/ASEE Joint Propulsion Conference*. Orlando, FL, United States: American Institute of Aeronautics and Astronautics, July 27–29, 2015. DOI: 10.2514/6.2015-3833.

[84] E. Paccagnella, F. Barato, D. Pavarin, and A. Karabeyoglu. "Scaling of Hybrid Rocket Motors with Swirling Oxidizer Injection - Part 2". In: *52nd AIAA/SAE/ASEE Joint Propulsion Conference*. Salt Lake City, UT, United States: American Institute of Aeronautics and Astronautics, July 25–27, 2016. DOI: 10.2514/6.2016-4750.

[85] E. Paccagnella, F. Barato, D. Pavarin, and A. Karabeyoglu. "Scaling Parameters of Swirling Oxidizer Injection in Hybrid Rocket Motors". In: *Journal of Propulsion and Power* 33.6 (Nov. 2017), pp. 1378–1394. DOI: 10.2514/1.B36241.

[86] E. Paccagnella, R. Gelain, F. Barato, D. Pavarin, P. van den Berg, and F. Barreiro. "CFD Simulations of Self-Pressurized Nitrous Oxide Hybrid Rocket Motors". In: *2018 Joint Propulsion Conference*. Cincinnati, OH, United States: American Institute of Aeronautics and Astronautics, July 9–11, 2018. DOI: 10.2514/6.2018-4534.

[87] E. Paccagnella, M. Santi, A. Ruffin, F. Barato, D. Pavarin, G. Misté, G. Venturelli, and N. Bellomo. "Testing of a Long-Burning-Time Paraffin-Based Hybrid Rocket Motor". In: *Journal of Propulsion and Power* 35.2 (Mar. 2019), pp. 432–442. DOI: 10.2514/1.B37144.

[88] G. Parissenti, M. Pessana, E. Gaia, E. Zaccagnino, F. Santilli, D. Pavarin, A. Bettella, J.-E. Ronningen, T. Valle, P. Van Put, R. Tijsterman, R. Popola, A. Pistek, E. Di Sotto, D. Grandou, V. Stasse, L. T. De Luca, L. Galfetti, and F. Maggi. "Throttleable Hybrid Engine for Planetary Soft Landing". In: *4th European Conference for Aeronautics and Space Sciences*. Saint Petersburg, Russia: EUCASS, July 4–8, 2011.

[89] D. Pastrone. "Approaches to Low Fuel Regression Rate in Hybrid Rocket Engines". In: *International Journal of Aerospace Engineering* 2012 (2012), pp. 1–12. DOI: 10.1155/2012/649753.

[90] J. Pucci. "The Effects of Swirl Injector Design on Hybrid Flame-Holding Combustion Instability". In: *38th AIAA/ASME/SAE/ASEE Joint Propulsion Conference & Exhibit*. Indianapolis, Indiana: American Institute of Aeronautics and Astronautics, July 7, 2002. DOI: 10.2514/6.2002-3578.

[91] L. N. Randall. "Rocket Applications of the Cavitating Venturi". In: *Journal of the American Rocket Society* 22.1 (Jan. 1952), pp. 28–38. DOI: 10.2514/8.4412.

[92] G. A. Risha, B. J. Evans, E. Boyer, and K. K. Kuo. "Metals, Energetic Additives, and Special Binders Used in Solid Fuels for Hybrid Rockets". In: *Fundamentals of Hybrid Rocket Combustion and Propulsion*. Ed. by K. K. Kuo and M. J. Chiaverini. Reston, VA, United States: American Institute of Aeronautics and Astronautics, Jan. 2007. DOI: 10.2514/4.866876.

[93] A. Rogers, P. Gloyer, R. E. Carlson, and S. Buckley. "SHERPA: A Flexible, Modular Spacecraftfor Orbit Transfer and On-Orbit Operations". In: *17th AIAA/USU Conference on Small Satellites*. Logan, UT, United States, Aug. 11–14, 2003.

[94] J.-E. Ronningen and J. Husdal. "Development of a Throttleable Hybrid Rocket Engine for the SPARTAN Lander". In: *Space Propulsion 2014*. Cologne, Germany: Association Aéronautique et Astronautique de France, May 19–22, 2014.

[95] J.-E. Ronningen, J. Husdal, M. Berger, R. Vesterås, and G. Raudsandmoen. "Nammo Hybrid Rocket Propulsion TRL Improvement Program". In: *48th AIAA/ASME/SAE/ASEE Joint Propulsion Conference & Exhibit*. Atlanta, GA, United States: American Institute of Aeronautics and Astronautics, July 30–Aug. 1, 2012. DOI: 10.2514/6.2012-4311.

[96] A. Ruffin. "Study and Development of Throttleable Hybrid Rocket Motors". PhD Thesis. Padova, Italy: Università degli Studi di Padova, 2018.

[97] A. Ruffin, F. Barato, M. Santi, E. Paccagnella, N. Bellomo, G. Misté, G. Venturelli, and D. Pavarin. "Development of a Cavitating Pintle for a Throttleable HybridRocket Motor". In: *7th European Conference for Aeronautics and Space Sciences*. Milano, Italy: EUCASS, July 3–6, 2017. DOI: 10.13009/EUCASS2017-425.

[98] A. Ruffin, E. Paccagnella, M. Santi, F. Barato, and D. Pavarin. "Real-Time Deep Throttling Tests of a Hydrogen Peroxide Hybrid Rocket Motor". In: *AIAA Propulsion and Energy 2019 Forum*. Indianapolis, IN, United States: American Institute of Aeronautics and Astronautics, Aug. 19–22, 2019. DOI: 10.2514/6.2019-4266.

[99] A. Ruffin, M. Santi, E. Paccagnella, F. Barato, N. Bellomo, G. Misté, G. Venturelli, and D. Pavarin. "Development of a Flow Control Valve for a Throttleable Hybrid Rocket Motor and Throttling Fire Tests". In: *2018 Joint Propulsion Conference*. Cincinnati, OH, United States: American Institute of Aeronautics and Astronautics, July 9–11, 2018. DOI: 10.2514/6.2018-4664.

[100] Y. Saburo, S. Noriko, and H. Kousuke. "Controlling Parameters for Fuel Regression Rate of Swirling-Oxidizer-Flow-Type Hybrid Rocket Engine". In: *48th AIAA/ASME/SAE/ASEE Joint Propulsion Conference & Exhibit*. Atlanta, GA, United States: American Institute of Aeronautics and Astronautics, July 30–Aug. 1, 2012. DOI: 10.2514/6.2012-4106.

[101] D. Saito, Y. Saburo, K. Hirata, T. Sakurai, and N. Shiraishi. "Combustion Characteristics of Paraffin-Fueled Swirling Oxidizer-Flow-Type Hybrid Rocket Engines". In: *48th AIAA/ASME/SAE/ASEE Joint Propulsion Conference & Exhibit*. Atlanta, GA, United States: American Institute of Aeronautics and Astronautics, July 30–Aug. 1, 2012. DOI: 10.2514/6.2012-3904.

[102] M. Santi, E. Paccagnella, A. Ruffin, F. Barato, D. Pavarin, G. Misté, G. Venturelli, and N. Bellomo. "Development and Testing of a Long Burning Time Lab-Scale Paraffin-Based Hybrid Rocket Motor". In: *53rd AIAA/SAE/ASEE Joint Propulsion Conference*. Atlanta, GA, United States: American Institute of Aeronautics and Astronautics, July 10–12, 2017. DOI: 10.2514/6.2017-4829.

[103] R. H. Schmucker. *Hybridraketenantriebe - Eine Einführung in theoretische und technische Probleme*. Das wissenschaftliche Taschenbuch: Abteilung Technik und Technologie 4. Munich, Germany: Goldmann, 1972.

[104] C. Sezaki, M. Sakamoto, K. Hirata, S. Yuasa, T. Sakurai, and N. Shiraishi. "Measurement of Axial-Direction Fuel Regression Rate of Swirling-Oxidizer-Flow-Type Hybrid Rocket Engines". In: *46th AIAA/ASME/SAE/ASEE Joint Propulsion Conference & Exhibit*. Nashville, TN, United States: American Institute of Aeronautics and Astronautics, July 25–28, 2010. DOI: 10.2514/6.2010-6547.

[105] G. Story. "Large-Scale Hybrid Motor Testing". In: *Fundamentals of Hybrid Rocket Combustion and Propulsion*. Ed. by K. K. Kuo and M. J. Chiaverini. Reston, VA, United States: American Institute of Aeronautics and Astronautics, Jan. 2007. DOI: 10.2514/4.866876.

[106] G. Story, T. Abel, S. Claflin, O. Park, J. Arves, and D. Kearney. "Hybrid Propulsion Demonstration Program 250K Hybrid

Motor". In: *39th AIAA/ASME/SAE/ASEE Joint Propulsion Conference and Exhibit*. Huntsville, AL, United States: American Institute of Aeronautics and Astronautics, July 20–23, 2003. DOI: 10.2514/6.2003-5198.

[107] G. Story and J. Arves. "Flight Testing of Hybrid-Powered Vehicles". In: *Fundamentals of Hybrid Rocket Combustion and Propulsion*. Ed. by K. K. Kuo and M. J. Chiaverini. Reston, VA, United States: American Institute of Aeronautics and Astronautics, Jan. 2007. DOI: 10.2514/4.866876.

[108] L. Strand, M. Jones, R. Ray, and N. Cohen. "Characterization of Hybrid Rocket Internal Heat Flux and HTPB Fuel Pyrolysis". In: *30th Joint Propulsion Conference and Exhibit*. Indianapolis, IN, United States: American Institute of Aeronautics and Astronautics, June 27–29, 1994. DOI: 10.2514/6.1994-2876.

[109] G. P. Sutton and O. Biblarz. *Rocket Propulsion Elements*. Hoboken, NJ, United States: John Wiley & Sons Inc, 2017.

[110] T. Takashi, S. Yuasa, and K. Yamamoto. "Effects of Swirling Oxidizer Flow on Fuel Regression Rate of Hybrid Rockets". In: *35th Joint Propulsion Conference and Exhibit*. Los Angeles, CA, United States: American Institute of Aeronautics and Astronautics, June 20–24, 1999. DOI: 10.2514/6.1999-2323.

[111] H. Tian, P. Zeng, N. Yu, and G. Cai. "Application of Variable Area Cavitating Venturi as a Dynamic Flow Controller". In: *Flow Measurement and Instrumentation* 38 (Aug. 2014), pp. 21–26. DOI: 10.1016/j.flowmeasinst.2014.05.012.

[112] E. Toson and A. M. Karabeyoglu. "Design and Optimization of Hybrid Propulsion Systems for In-Space Application". In: *51st AIAA/SAE/ASEE Joint Propulsion Conference*. Orlando, FL, United States: American Institute of Aeronautics and Astronautics, July 27–29, 2015. DOI: 10.2514/6.2015-3937.

[113] D. Van Pelt, M. Skinner, A. Buchanan, R. Gulman, H. Chan, J. Hopkins, and M. A. Karabeyoglu. "Overview of a 4-inch OD Paraffin-Based Hybrid Sounding Rocket Program". In: *40th AIAA/ASME/SAE/ASEE Joint Propulsion Conference and Exhibit*. Fort Lauderdale, FL, United States: American Institute of Aeronautics and Astronautics, July 11–14, 2004. DOI: 10.2514/6.2004-3822.

[114] K. R. Wagner and R. H. Schmucker. "Hybrid Propulsion for Space Applications - A Critical Assessment". In: *28th Joint Propulsion Conference and Exhibit*. Nashville, TN, United States: American Institute of Aeronautics and Astronautics, July 6–8, 1992. DOI: 10.2514/6.1992-3305.

[115] G. Williams, F. Macklin, M. Sarigul-Klijn, N. Sarigul-Klijn, and J. Benson. "Almost There: Responsive Space". In: *2nd Responsive Space Conference*. Los Angeles, CA, United States, Apr. 19–22, 2004.

[116] S. Yuasa, O. Shimada, T. Imamura, T. Tamura, and K. Yamoto. "A Technique for Improving the Performance of Hybrid Rocket Engines". In: *35th Joint Propulsion Conference and Exhibit*. Los Angeles, CA, United States: American Institute of Aeronautics and Astronautics, June 20–24, 1999. DOI: 10.2514/6.1999-2322.

[117] S. Yuasa, K. Yamamoto, H. Hachiya, K. Kitagawa, and Y. Oowada. "Development of a Small Sounding Hybrid Rocket with a Swirling-Oxidizer-Type Engine". In: *37th Joint Propulsion Conference and Exhibit*. Salt Lake City, UT, United States: American Institute of Aeronautics and Astronautics, July 8–11, 2001. DOI: 10.2514/6.2001-3537.

ACKNOWLEDGMENTS

These three years of PhD Program have been a great experience and to complete this journey has been a satisfying accomplishment, even if writing this Thesis has been more challenging than I thought. To arrive where I am now, both professionally and personally, would not have been possible without the advice, support, and friendship of many invaluable people.

First and foremost, I would like to thank the head of the Advanced Space Propulsion Group, Daniele Pavarin. I can't help but be amazed by his passion and his ability to think out of the box, even if trying to keep pace with his chaotic mind is exhausting. I would like to express my sincere gratitude to the head of the Hybrid Propulsion Group, Francesco Barato, for his endless support and patience during all the time of my research. He set an example with his motivation and immense knowledge. I would also like to thank the coordinator of the PhD Course, Giampiero Naletto, for the precious work that he does for all of us students and for his effort in avoiding that the place shuts down. I have to recognize that without them none of this would have been possible.

I would like to thank the only person I know that is more scrupulous than me, Nicolas Bellomo, for letting me learn so much from his expertise and attitude. My heartfelt thanks go to those who helped shape this group, Giovanni Venturelli and Gianluigi Misté, even if they are not part of it anymore. I won't forget to thank my PhD colleagues, Alessandro Ruffin and Marco Santi, for the stimulating discussions and for the fun we had during these years. I would also like to thank our first technician, Federico Conte, for being so helpful all the time and for being always able to work with a smile. All these people are now a lot more than just colleagues and working together has been a pleasure and an honor.

A special word must be said for Andrea Scapin and Stefano Giacometti, two unmatched artisans and unique people. I am also pleased to say thank you to those who are working in our group but I didn't have the time to know better yet, the whole Plasma Propulsion and Antennas Group, all the employees of T4i, and the students who stopped by just for a few months but left a mark.

Last but not the least, I would like to express my deepest gratitude to my family and friends. I would like to thank my mother, who is always able to get to the point with her unsolicited but priceless advice and who always does everything she can for me. I would like to thank my father, who is an important example and is always there when I need it. Thank you, mom and dad, for showing me how to have a happy and full life and for helping me arrive where I am now.

I would like to thank my brothers, because in their own way, with a little healthy competition, they push me everyday to better myself. Finally, I would also like to thank all my friends and special people, those I know for as long as I can remember, those I met recently and with whom we became inseparable, those who will always be there even if we don't see each other very often, those who suddenly came into my life bringing a breath of fresh air without even expecting it.